1. SPATIALLY RESOLVED ABSOLUTE SPECTRAL REFLECTIVITY OF JUPITER: 3390 - 8400 ANGSTROMS

2. THE JOVIAN THERMAL STRUCTURE FROM PIONEER 10 INFRARED RADIOMETER DATA

3. OBSERVATIONS AND ANALYSIS OF 8 - 14 MICRON THERMAL EMISSION OF JUPITER: A MODEL OF THERMAL STRUCTURE AND CLOUD PROPERTIES

Thesis by

GLENN SCOTT ORTON

In Partial Fulfillment of the Requirements

for the Degree of

Doctor of Philosophy

California Institute of Technology

Pasadena, California

1975

(Submitted 13 January 1975)

DEDICATION

To my parents, without whose efforts none of this would have been possible.

To an interested and sympathetic high school physics instructor.

To the Source of all Mysteries.

ACKNOWLEDGEMENTS

I gratefully acknowledge the continued advice and helpful criticism provided by Dr. Andrew P. Ingersoll in his role as advisor to my thesis work. He deserves special recognition for his critical reading of this work in its formative stages, and also for his considerable tolerance of my occasional backtracking and my somewhat iterative writing style.

I thank Dr. Duane O. Muhleman, both for his comments during the writing of this thesis and for the challenge and interest which he provided in the initial stages of my graduate career.

For suggesting the subject of Part 1 and for his advice and assistance in its undertaking, I thank Dr. Guido Münch. Acknowledgements are due for Dr. Dennis Matson and Dr. Torrance Johnson for their advice and assistance during some of the initial observing periods, and for the use of some of their scheduled observing time on the Mt. Wilson 60-inch telescope. I thank Dr. J. Beverley Oke for useful discussions concerning calibration procedures, and David Pollard for help in reducing some of the data presented in Part 1. My thanks goes to the scheduled observing assistants at Mt. Wilson, James Dittmar, John Kondratowicz, and Michael Marcario, and to colleagues and other friends (with whose help I got by) who have assisted me in making the observations presented in Part 1, generally working at a furious pace to utilize the short time periods when Jupiter was available photometrically: Bruce Bills, Michael Dailey, David Diner, Anthony Dobrovolskis, Daniel Dzurisin, J. Andreas Howell, Judson James, Philip Nicholson, Barbara Noyes, Richard McCreight, Mark Reid, Steve Roe, Maritza Stapanian, Donald Sullivan, and Julius Uradnisheck. I express appreciation to the kind and helpful staffs of the

Mt. Wilson Observatory and the Caltech Astro-Electronics Laboratory.

My extreme thanks goes to the Pioneer 10 infrared radiometer team, headed by Dr. Münch and Dr. Gerry Neugebauer, without which Part 2 would have been impossible, and to team member Dr. Lawrence Trafton for the use of his calculation routine for estimating the He-induced H_2 dipole absorption coefficients. I thank Prof. James Westphal and Richard Terrile for allowing me access to their December 1973 5-micron images of Jupiter in advance of publication and for several useful discussions. David Diner deserves credit for making the appropriate latitude bins of Pioneer 10 infrared data which were used in the analysis and are displayed in many of the figures in Part 2.

I gratefully acknowledge Prof. Westphal for providing both the motivation to begin what developed into Part 3 of this thesis and the observing time on the 200-inch telescope at Palomar Mountain. I thank Dr. Fred Gillett for his interest, and for the committment of his time and equipment which made the observations reported in Part 3 possible. I am also indebted to Dr. Fredric Taylor for his encouragement and for many useful discussions concerning the models presented in Part 3.

Much help in the preparation of this manuscript was extended by Kay Campbell and Brenda Parson.

I acknowledge the support of a California State Fellowship during the period this work was undertaken. Much of this research has been supported by NASA NGL 05-002-003.

PREFACE

This thesis represents three separate topics of research which concern the atmosphere of Jupiter.

Part 1 deals with the absolute reflectivity of several of the features of the planetary disk at visible wavelengths. It reports the results of observations made with some difficulty using the 60-inch telescope at Mt. Wilson. Discussion is given with regard to the absorption which takes place both in the continuum and in molecular bands, and to differences with earlier results obtained by other observers.

Part 2 uses the thermal maps of Jupiter at 20 and 40 microns retrieved by the Pioneer 10 infrared radiometer to derive a thermal structure, constraints on the relative abundances of H_2 and He, and a measure of the thermal energy output of the planet. The conclusions of this part are somewhat dependent on the model which has been assumed for the opacity of the atmosphere at these wavelengths.

Part 3 combines: (1) a report of observations of Jovian limb structure near 8 microns made with Dr. Fred Gillett using the Palomar Mountain 200-inch telescope, with (2) a general model for the Jovian atmosphere which is consistent with ground-based observations of the 8 - 14 micron thermal emission. The atmospheric structure derived in this part depends on models of the opacity contributed by several atmospheric constituents. The number of alternative models has been reduced to include only what appears to be the simplest and least unusual. Nevertheless, the model is somewhat detailed and it probably represents the most open-ended undertaking included in this thesis.

ABSTRACT

Part 1 presents determinations of the absolute reflectivities of several visually distinct regions of Jupiter between 3390 and 8400Å, at 10Å resolution, from observations made on the 60-inch telescope at Mt. Wilson between June 1973 and June 1974. These have been checked independently by observations using 150-200Å wide filters from 3400 to 6400Å. The absolute scale of Oke and Schild (1970) is used, and solar irradiance values are taken from Arvesen et al.(1969).

The results are presented as a set of 9 figures showing the wavelength dependence of reflectivity. There is generally good internal consistency within the estimated errors. The effective reflectivities for several regions on the meridian in the 3390 to 8400Å range are: South Tropical Zone- 0.76±.05, North Tropical Zone- 0.68±.08, South Equatorial Belt- 0.63±.08, North Equatorial Belt- 0.62±.04, and Great Red Spot- 0.64±.09 . Reflectivities nearer the limb are also observed. In support of the Pioneer imaning photopolarimeter experiment, the appropriate blue and red reflectivity values are also tabulated. For the regions on the meridian listed above, the equivalent widths of molecular bands vary as: CH_4 (6190Å): 14-16Å; CH_4(7250Å): 77-86Å; and NH_3(7900Å): 87-95Å. Significant differences from previous results of Pilcher et al. (1973) are noted.

* * *

Part 2 presents latitude sectors of the 20 and 40 micron maps of Jupiter obtained by the Pioneer 10 infrared radiometer. These data are used to derive simple models for the average vertical thermal structure over the South Equatorial Belt and the South Tropical Zone, with additional examples of models for the North Equatorial Belt and the Great Red Spot.

The models assume gaseous absorption by H_2 and NH_3 alone. The models are predominantly composed of H_2 with He dilution constrained to 0-35% by volume.

For the South Equatorial Belt, the temperature is about $170^{\circ}K$ at 1.0 atm pressure, assuming the deep atmosphere to be adiabatic. The temperature may be $113\text{-}121^{\circ}K$ near 0.2 atm, depending on what is assumed for the overlying thermal structure. In a non-scattering model, as given above, the South Tropical Zone is some $8^{\circ}K$ cooler than the SEB near 1.0 atm. However, the data may also be successfully modeled by a thermal structure at minimum variance from that of the SEB, but with an optically thick cloud close to the $150^{\circ}K$ level. Such a model is consistent with the visible and 5 micron appearance of the planet, and the cloud is coincident with the location at which saturation of NH_3 is expected to begin. For this model, the STrZ temperature is $3^{\circ}K$ cooler than the SEB near 0.2 atm. The Great Red Spot may be modeled by a thermal structure like the "cloudy" STrZ model, but $5^{\circ}K$ cooler near 0.2 atm. The local effective temperatures for the SEB ($129^{\circ}K$) and the STrZ ($126^{\circ}K$) are both below the effective temperature of $134^{\circ}K$ from earth-based measurements. The derived thermal structures are inconsistent with the neutral atmosphere inversion of the Pioneer 10 radio occultation (Kliore et al.,1974), but not with others in the literature, including the Gulkis et al. (1973) model for the microwave spectrum.

Part 3 reports: (1) observations of the limb structure near the equator of Jupiter at 8.15 and 8.44 microns using the Palomar 200-inch telescope at a resolution of about 3 arc seconds and a cooled filter-wheel

spectrometer ($\Delta\lambda/\lambda \approx 0.015$), and (2) a model of the thermal structure and cloud properties of the atmosphere which is most consistent with spatially and spectrally resolved observations of the planet in the 8 - 14 micron range, including those reported in (1).

The thermal structure derived in Part 2 below the 0.2 atm level must be cooled by some 6°K in order to match the 12-14 micron spectrum, which is dominated by the opacity of H_2. An NH_3 abundance defined by saturation equilibrium is consistent with the 9.5-12.0 micron spectrum, dominated by the opacity of that gas. The thermal structure above the 0.2 atm level is determined by fitting spectral and limb structure data in the 7.2-8.4 micron range, dominated by the opacity of CH_4. The result is an inverted thermal structure with a base of about 110°K at 0.2 atm, rising through 150°K at about 0.03 atm. The mixing ratio of CH_4 most consistent with the spectral and limb structure data is 2.0×10^{-3}, some three times that assumed in "solar abundance" models.

The 8.2-9.5 micron spectral region is not earily matched by simple gaseous opacity sources. However, a haze of solid NH_3 particles above a thick cloud (which exists only in zones, as implied in Part 2) is consistent with the observed spectrum. Difficulty is encountered, however, with limb structure data at 8.44 microns and with some observations outside the 8-14 micron range.

Further observations of the separate spectral characteristics of belts and zones is recommended, as well as more accurate laboratory data for the opacity of atmospheric constituents in the relevant thermal regime and more sophisticated scattering approximations that used in this model.

TABLE OF CONTENTS

TABLE OF CONTENTS

FIGURES: Part 1

TABLE OF CONTENTS

TABLES: Part 1

§

TABLE OF CONTENTS

Part 2 (cont'd.) Page

FIGURES: Part 2

Number

TABLE OF CONTENTS

Part 2 (cont'd.) Page

FIGURES: Part 2

Number

TABLE OF CONTENTS

FIGURES: Part 2 (CONT'D.)

TABLE OF CONTENTS

TABLES: Part 2

Part §

TABLE OF CONTENTS

Part 3 (cont'd.) Page

FIGURES: Part 3

Number

TABLE OF CONTENTS

FIGURES: Part 3 (CONT'D.)

PART 1

SPATIALLY RESOLVED ABSOLUTE SPECTRAL REFLECTIVITY OF JUPITER: 3390 - 8400 ANGSTROMS

I. INTRODUCTION

This paper presents observations which are used to determine the reflectivity of several distinct visible regions of Jupiter. Simultaneously, this paper also represents the continuing education of this author in the realities and significance of absolute astronomical measurements.

The data which is presented in this report is considered to be of good quality, but it has been acquired with some difficulty. The difficulty of spatially resolved absolute photometry of Jupiter with high wavelength resolution is compounded by the limitations of the available observing site. As a result, the best of the observations have been taken some 30 to 40 degrees above the Los Angeles skyline (and somewhat closer to the L.A. smogline). Furthermore, Jupiter was seldom available for more than 3 hours each night during the period when these observations were made. Combined with the extent of the observational detail in wavelength, this has forced not only very efficient use of observational time (wherever it could be found), but also some rather uncommon calibration techniques. These are explained in detail in the next section of this paper. Considerable detail in the text is also devoted to data credibility and error analysis, in view of the difficulty of the observations.

The motivation for examining separate regions on Jupiter is straightforward. Some early whole disk photometry of Jupiter is reviewed by Harris (1961) and more recent work has been continued by Taylor (1965) and Irvine et al. (1968a, 1968b). However, such observations are easily confused by the obvious time changes which take place in the detailed albedo structure of the planet. Spatially resolved observations of Jovian reflectivities have recently been published by Pilcher, Prinn, and McCord (1973) (hereafter referred to as PPM in this paper). To a certain extent, the measurements of PPM have duplicated the goals of this study.

The results presented here are important in several respects. It is particularly useful to verify observations such as those made by PPM, particularly with a different calibration system. In such a way, the effects of different calibration techniques may be separated from real time variations of the features. As will be shown, significant differences between the present results and PPM are observed. The results presented here also extend to regions not included in PPM. An attempt is also made to determine limb structure in individual regions. Reflectivity variations in a time scale on the order of a year and variations with solar phase angle should also have been possible, as well. However, the level of uncertainty in the observations has precluded the success of such measurements.

It is also quite important to mention that these observations may provide some support for the interpretation of data retrieved by the imaging photopolarimeter on board Pioneer 10 and 11 (Coffeen, 1973). Their proximity to the time the spacecraft data was acquired may reduce some of the effects of the variation of the reflectivities over long time periods.

II. OBSERVATIONS AND DATA REDUCTION

A. Summary of Observations

Spatially resolved single beam photometric observations of several Jovian regions have been made between 17/18 June 1973 and 3/4 June 1974 with the 60-inch telescope at Mt. Wilson. These observations consist of measurements of the flux of each region through a fixed solid angle defined by the aperture of the instrument. The regions are measured on the central meridian of Jupiter; measurements closer to the limb are also presented for some regions. The nights of observations from which data is presented in this report are summarized in Table 1.

Most observations were made with an Ebert-Fastie type all-reflection scanning spectrometer at the Cassegrain focus. This instrument was used in both a scanning mode and in a discrete wavelength mode with an aperture of 4.20 seconds of arc, centered on each region observed. A larger aperture was used for observations of standard stars. The observations were made in the second order of the spectrometer with an S-17 phototube and in the first order with a GaAs phototube. Blocking filters were used to remove radiation from adjacent overlapping orders. The system of detectors, blocking filters, and wavelengths observed is summarized in Table 2.

In addition, on the night of 24/25 July 1973, the 60-inch telescope was used with a different photometer. This photometer (McCord, 1968a) uses a wheel containing several interference filters with fixed transmission characteristics. Although the photometer is capable of double-beam observations, the available supporting electronics required the use

TABLE 1

NIGHT OF OBSERVATION	DETECTOR
17/18 June 1973	S-17
18/19 June 1973	GaAs
10/11 August 1973	S-17
14/15 August 1973	GaAs
21/22 August 1973	GaAs
2/3 October 1973	GaAs
3/4 October 1973	S-17
10/11 October 1973	GaAs
31 May/1 June 1974	GaAs
3/4 June 1974	GaAs*

(*extended to wavelengths: 3571-4785Å)

TABLE 2

Wavelengths (Å)		Blocking Filter	Phototube
Scan Observations	Discrete Observations		
3390-3571	3390	UG11	S-17
	3448		
	3509		
	3571		
3571-4785	3571	BG38	
	3636		
	3704		
	4032		
	4167		
	4255		
	4464		
	4566		
	4785		
4785-6370	4785	G65	
	5000		
	5263		
	5556		GaAs
	5840		
	6055		
	6370		
6370-8400	6370	R61	
	6800		
	7100		
	7530		
	7850		
	8080		
	8400		

TABLE 3

CENTRAL WAVELENGTHS FILTERS USED WITH McCORD PHOTOMETER

Filter	Wavelength
1	3400Å
2	4200Å
3	4400Å
4	4800Å
5	5200Å
6	5800Å
7	6200Å
8	6400Å

of the single beam mode. Observations of Jupiter were made with an aperture of 2.41 seconds of arc using this photometer with a set of eight filters, whose central wavelengths are summarized in Table 3. The filters have resolutions between 150 and 200 Å. Again, a larger aperture was used for observations of narrow and point sources taken as standards. The results of these observations are used to verify the results of observations made with the Cassegrain scanner.

The calibration system for observations with each instrument is devised to remove the effects of the instrument response, solar absorption lines reflected by Jupiter, and telluric absorption. For the scanner, observations of the Mare Serenitatis 2 section of the Moon (McCord, 1968b) are used for reference with the Jovian data, to remove solar and telluric absorption features at the resolution of the observations. J4 (Callisto) is used for this purpose with observations made using the McCord photometer. The observed spectra are placed on an absolute scale by reference to observations of the standard star ϵ Aqr made on the same night.

B. Definition of the Observational Problem

The absolute intensity scale as a function of wavelength is presented as I/F, where I is the specific intensity observed from Jupiter and πF is the incident solar flux. This ratio is observationally determined by:

$$I/F = \frac{F_{\text{Jupiter}}}{F_{\text{Sun}}} \left(\frac{R}{a}\,\theta\right)^2 \quad . \tag{1}$$

In this equation, F_{Jupiter} and F_{Sun} are the respective spectral irradiances of Jupiter and the sun, observed outside the earth's atmosphere. R is the distance between the sun and Jupiter at the time of the observations and a is the distance between the earth and the sun at the time of the solar spectral irradiance measurements. The angle θ is the size (in radians) of the arc subtended by the aperture radius, i.e. $\pi/648000$ times 2.10 seconds of arc for the scanner observations and 1.20 seconds of arc for the McCord photometer observations.

The observational problem, then, is the determination of the ratio $F_{Jupiter}/F_{Sun}$ equal to that outside the earth's atmosphere for the wavelength range of interest. The solar spectral irradiance has been measured by Arvesen et al. (1969) and their results have been used for F_{Sun} in this analysis. A complication arises, however, due to the effects of narrowband spectral features in the solar spectrum and the finite spectral resolution of the instruments used in this study. Thus, observations of the Moon and the Galilean satellite J4 were made to determine the effects of degrading the solar spectrum at the resolution of these instruments.

The star ε Aqr has been used to place the Jupiter observations on an absolute scale. Oke (1964) has calibrated this young star, which presents a nearly continuous spectrum (with the great exception of the Balmer discontinuity) with respect to the prime photometric standard star, α Lyr. Oke and Schild (1970) have calibrated α Lyr on an absolute basis. The absolute flux spectrum of ε Aqr is thus obtained by multiplying the ratio of ε Aqr to α Lyr fluxes by the absolute flux of α Lyr. The observations of these stars are made at wavelength positions which avoid non-continuous telluric absorption. A smooth curve through the absolute spectrum of ε Aqr at each of these wavelength positions is then taken to be a reasonable approximation of the ε Aqr spectrum outside the earth's atmosphere.

C. The Calibration System: Cassegrain Scanner Data

For the scanner data, a reduction system which uses a Galillean satellite (as in PPM) to remove the effects of solar and telluric absorption features from Jovian observations is not considered adequate for several reasons. First, on the 60-inch telescope the low photon count from the satellite at 10Å resolution makes it difficult to gather statistically adequate data without drastic reduction of the time available for observations of Jupiter. Second, the background sky near the satellite contains the strongly wavelength-dependent features of the Jovian spectrum. Thus, rigorous subtraction of the sky background requires complete wavelength scanning observations. Third, it is in the interest of time efficiency to forego complete wavelength scans of the standard star in favor of observations at the set of discrete standard wavelengths used by Oke (1964) and Schild (1970). (Hereafter, for brevity, these are referred to as the standard wavelengths. They are listed in Table 2.)

The calibration system for the Cassegrain scanner data is summarized by the following equation:

where $\odot$ - includes solar lines
$\oplus$ - includes telluric lines
instr. - includes instrument response function

$$\frac{F_{\text{Jupiter}}}{F_{\text{Sun}}} = \underbrace{\frac{f_{\text{Jupiter}}(\odot,\oplus,\text{instr.})}{f_{\epsilon\text{Aqr}}(\text{instr.})} \times \frac{f_{\text{std. star}}(\text{instr.})}{f_{\text{Moon}}(\odot,\oplus,\text{instr.})}}_{A} \times \underbrace{\frac{F_{\epsilon\text{Aqr}}}{F_{\text{std. star}}}}_{B} \times \underbrace{\frac{F_{\text{Moon}}(\odot)}{F_{\text{sun}}}}_{C} \qquad (2)$$

(A) From observational program: $f_{\text{Jupiter}}(\odot,\oplus,\text{ instr.})$ and $f_{\text{Moon}}(\odot,\oplus,\text{instr.})$ from wavelength scans; $f_{\epsilon\text{Aqr}}(\text{instr.})$ and $f_{\text{std. star}}(\text{instr.})$ from polynomial interpolation of observations at standard wavelengths Standard stars used for the lunar calibration were ζ Oph ($\lambda \leq 4785$Å) and 29 Psc ($\lambda \geq 4785$Å)

(B) From Oke (1964).

(C) $F_{\mathrm{Sun}}(\odot)$ from Arvesen, et al. (1969).

$F_{\mathrm{Moon}}(\odot)$ from $$F_{\mathrm{Moon}}(\odot,\oplus) = \underbrace{\frac{f_{\mathrm{Moon}}(\odot,\oplus,\mathrm{instr.})}{f_{\mathrm{std.\ star}}(\mathrm{instr.})}}_{\substack{\text{observational}\\ \text{program}}} \times \underbrace{F_{\mathrm{std.\ star}}}_{\substack{\text{Oke (1964) and}\\ \text{Oke and Schild (1969)}}}$$

and smooth interpolation in the neighborhood of telluric absorption lines.

The ratio $F_{\mathrm{Moon}}/F_{\mathrm{Sun}}$ is a smoothly varying function of wavelength, determined as described above. Telluric absorption effects are minimized in the ϵ Aqr and other std. star observations by polynomial interpolation among observations at the standard wavelengths. This interpolation does not accurately describe the stellar spectrum in the neighborhood of the Balmer discontinuity, but the effect of this approximation is minimized by its use in both numerator and denominator of equation (2).

Observations of the Mare Serenitatis 2 section of the Moon have two advantages over the more common practice of using a G-type star as an approximation to the solar spectrum. One is the obvious advantage of brightness, which makes the statistical sampling requirements for scan data easy to fulfill. The second is the certain coincidence of observed features in the radiation reflected from the lunar surface with those of the sun itself.

One of the disadvantages of using the Moon is that it was not available near Jupiter on all nights when observations could be taken. The Jovian observations were, therefore, referenced to lunar observations taken on other nights. This requires the assumption that the telluric absorption on one night is compatible with other nights. This is certainly not strictly true, especially for strong telluric absorption features. For this reason, regions of strong telluric absorption have been omitted from the results shown in the next section. For the remainder of the spectrum, no differences are observed between the results of many nights of observation, as presented in the next section, and the results of observations taken on the same night as the lunar observations.

Continuous telluric absorption is assumed to be a linear function of air mass. The extinction of the atmosphere is determined empirically by several observations of a Galilean satellite over a range of air masses at the standard wavelengths. These were verified by observations of standard stars, including ϵ Aqr, covering a wide range of air masses, using relative fluxes as given by Oke (1964).

D. The Calibration System: McCord Photometer

For the fixed filter photometer, the calibration system is quite simple:

$$\frac{F_{\text{Jupiter}}}{F_{\text{Sun}}} = \frac{f_{\text{Jupiter}}(\odot,\oplus,\text{instr.})}{f_{J4}(\odot,\oplus,\text{instr.})} \times \underbrace{\frac{f_{J4}(\odot,\oplus,\text{instr.})}{f_{\epsilon\ \text{Aqr}}(\oplus,\text{instr.})}}_{A} \times \underbrace{\frac{F_{\epsilon\ \text{Aqr}}}{F_{\text{Sun}}(\odot)}}_{B} \qquad (3)$$

(A) From observational program.

(B) $F_{\epsilon\ \text{Aqr}}$ and F_{Sun} for each filter determined by folding respective spectra into filter functions. As a continuous function of wavelength, $F_{\epsilon\ \text{Aqr}}$ is polynomial interpolation of flux at standard wavelengths from Oke (1964) and Oke and Schild (1970), and F_{Sun} is from Arvesen et al. (1969).

In this equation, symbols are used as in equation (2). The observations of J4 are not necessary in theory to remove the effects of telluric absorption. The proximity of Jupiter and J4 in space, however, allowed a very reliable comparison of the fluxes over more similar atmospheric conditions than direct comparison of Jupiter and ϵ Aqr observations.

As in the Cassegrain scanner observations, the extinction of the atmosphere is assumed to be linear and is determined empirically by observations of J4 and of ϵ Aqr. In both calibration systems, it is assumed that the measured flux ratios of Jupiter, J4, and ϵ Aqr may closely approximate the ratios outside the earth's atmosphere, if the observations are taken as nearly as possible under the same conditions, i.e., close together in time and referred to the same air mass via the extinction coefficients.

E. Determination of the Data Quality

Two criteria were used simultaneously to determine the expected quality of the data for each night. The most accurate one was the scatter in the computed values of the reflectivity at a given wavelength for the same Jovian region observed more than once during the night. The other criterion was the deviation of the observed flux values for a Galilean satellite or the standard stars from a linear extinction curve. Data were eliminated from consideration where the scatter in the observed flux or computed reflectivity exceeded a standard deviation equivalent to 6% of the value.

Additional criteria were used for eliminating data from consideration. No observations at air mass values greater than 2.00 were considered. Furthermore, no results are presented in the next section which were not observed on more than a single night, by whatever means (e.g., at all wavelengths with scans or only at the discrete standard wavelengths). This qualification was made as the criteria for data quality listed above are not considered by any means to be failsafe.

The effect of these criteria was to eliminate from consideration some 48% of the nights on which observations were taken, not including 24/25 July 1973, when the McCord photometer was used. The remaining nights are those shown in Table 1.

F. Method of Positional Control

For observations of features near the limb, it was desirable to maintain some quantitative control over the position of the aperture on the visible disk. Unfortunately, attempts to adapt photographic equipment to the scanner met with little success, and so a cruder control was used. The aperture position was centered 1.5 aperture diameters from the limb. This technique suffers from the arbitrary judgement of the observer with respect to relative sizes and limb position, both of which are affected by varying conditions of seeing.

Some verification of this technique was made by observing the Great Red Spot (GRS) near the limb, using this technique for positional control. An independent determination of its position was made by recording the time interval between the limb position and central meridian passage and comparing it with the known rotational period of the GRS. By both techniques, the cosine of the local emission angle, μ, for the South Tropical Zone and the Great Red Spot is 0.72 ± 0.05. The uncertainty in the value of μ is assumed to be the same for regions closer to the equator as well.

III. RESULTS

A. Summary

Figure 1 demonstrates the aperture positions on the visible disk, centered over various regions, for the Cassegrain scanner observations (left) and the McCord photometer observations (right). The regions observed include: the North Temperate Zone (NTeZ), the North Tropical Zone (NTrZ), the North Equatorial Belt (NEB), the Equatorial Zone (EZ), the South Equatorial Belt (SEB), the South Tropical Zone (STrZ), the Great Red Spot (GRS, not shown), the South Temperate Zone (STeZ), and the South South Temperate Zone (SSTeZ). The Cassegrain scanner observations with the aperture centered 1.5 aperture diameters from the polar limbs are identified as "North Polar Region" ("NPR") and "South Polar Region" ("SPR") for convenience. The scanner observations identified as "NTrZ" actually combine the radiation emitted by the North Tropical Zone with that emitted by the North Temperate Belt (NTeB) and the North Temperate Zone. The McCord photometer observations near the poles center the aperture over the visibly dark regions which are identified here as the North Polar Hood (NPH) and the South Polar Hood (SPH).

Figures 2 - 10 show the measured reflectivity of these regions, averaged over all the observations. The figures include the results of: (1) scan and standard wavelength measurements using the Cassegrain scanner, and (2) the wider band measurements using the McCord photometer. Scan measurements are indicated by the solid line, with error bars located at the end points of the wavelength region where each blocking filter was used: 3390, 4785, 6370, and 8400 Å. Measurements at the set

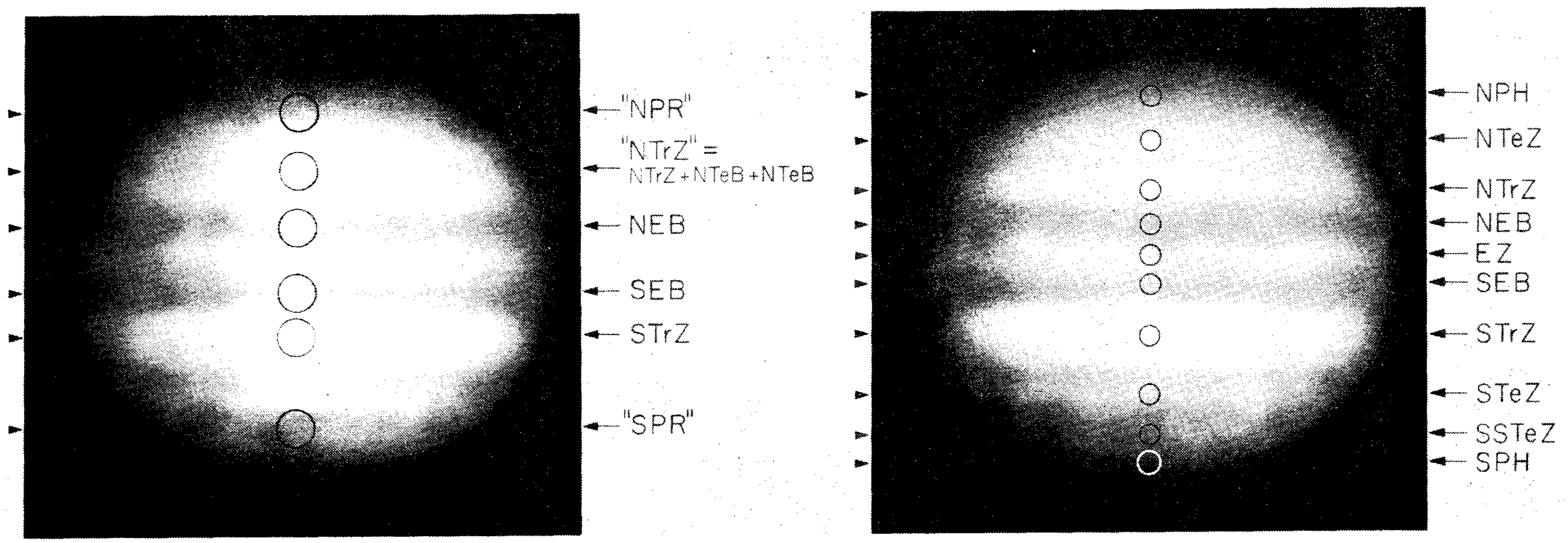

Fig. 1. -Aperture positions on visible disk of Jupiter during observations. Cassegrain scanner positions on left and McCord photometer positions on right. Circles represent typical aperture size relative to disk. Nomenclature is explained in text.

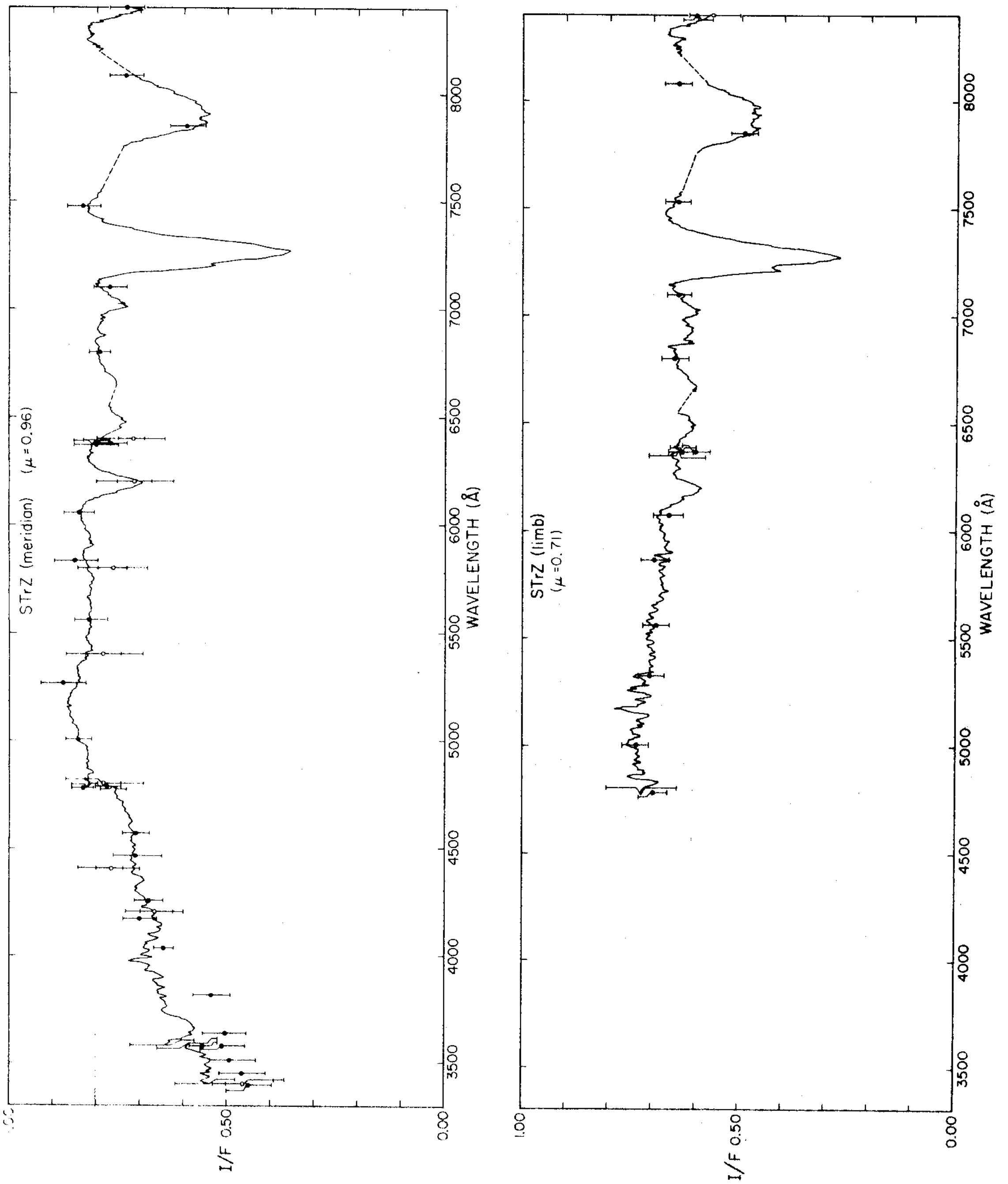

Figs. 2A.(top) 2B.(bottom) -Measured absolute spectral reflectivity of South Tropical Zone. Solid line represents scan observations and filled circles standard wavelength observations (both with Cassegrain scanner); open circles represent McCord photometer observations. Vertical bars represent error estimates. μ is cosine of local emission angle.

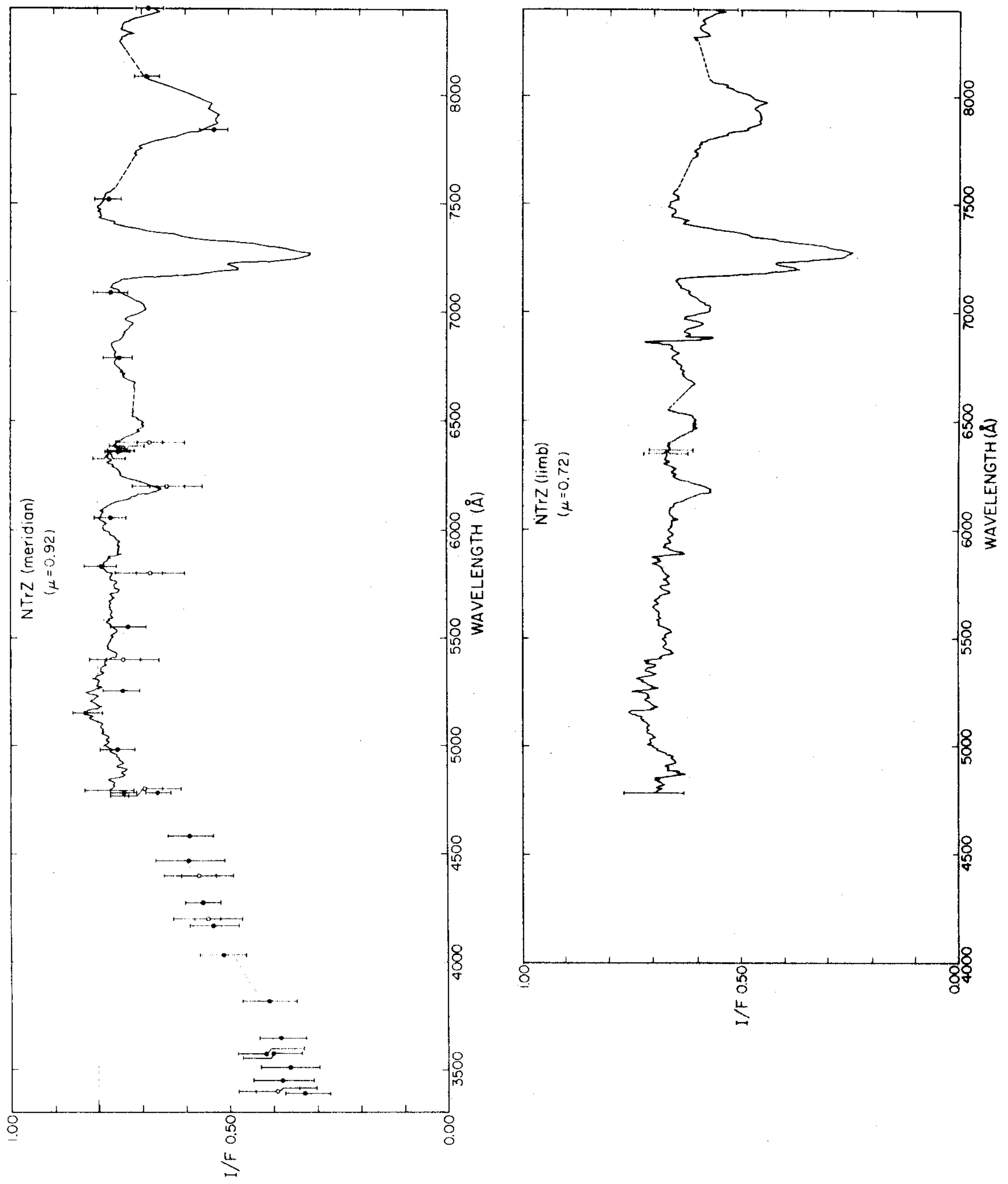

Figs. 3A.(top) 3B.(bottom) -Measured absolute spectral reflectivity of North Tropical Zone. Symbols as in figs. 2A and 2B. Cassegrain scanner measurements are of "NTrZ" region in fig. 1.

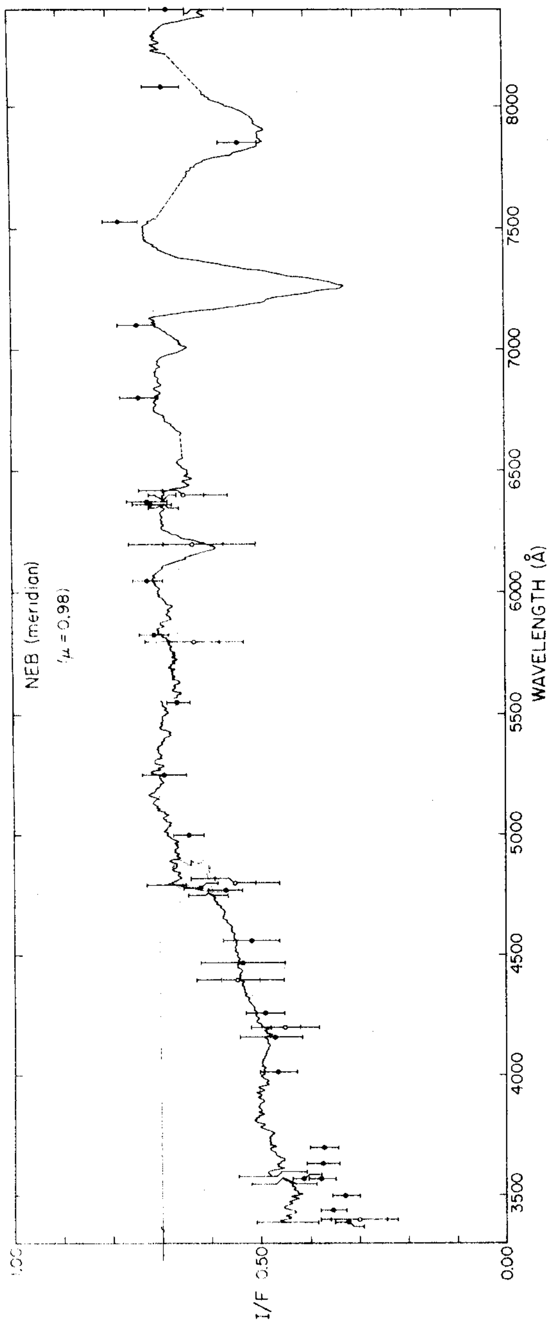

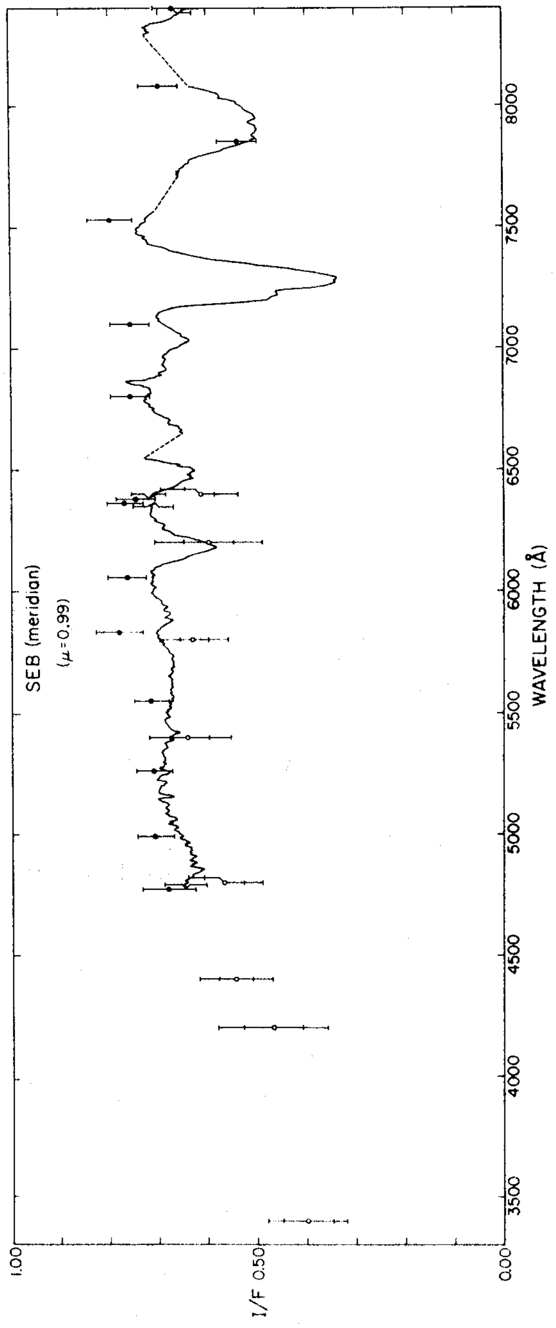

Fig. 4. (top) -Measured absolute spectral reflectivity of North Equatorial Belt.
Fig. 5. (bottom) -Measured absolute spectral reflectivity of South Equatorial Belt. In both figures, symbols as in figs. 2A and 2B.

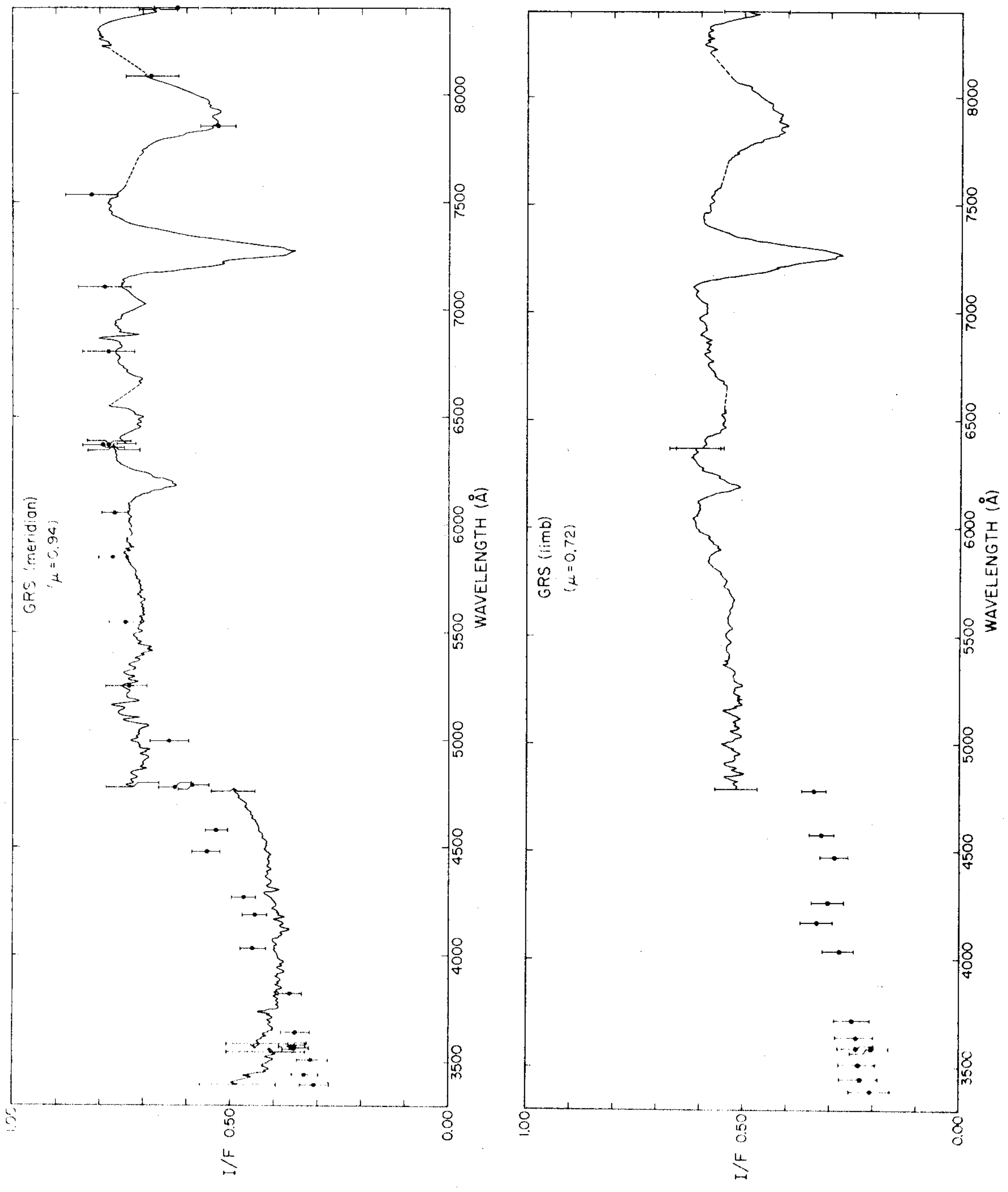

Figs. 6A.(top) 6B.(bottom) -Measured absolute spectral reflectivity of Great Red Spot. Symbols as in figs. 2A and 2B.

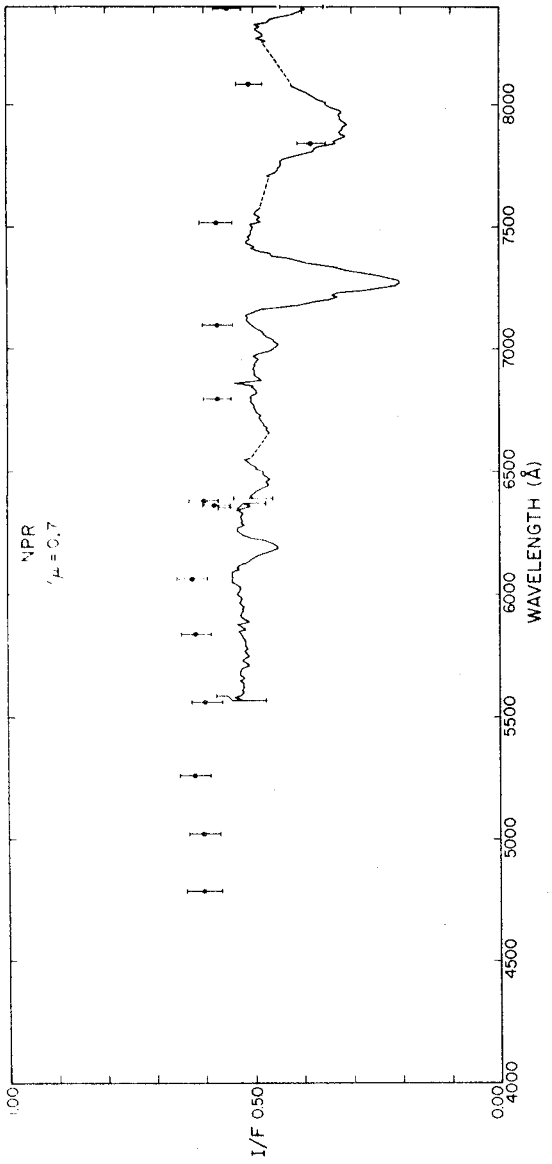

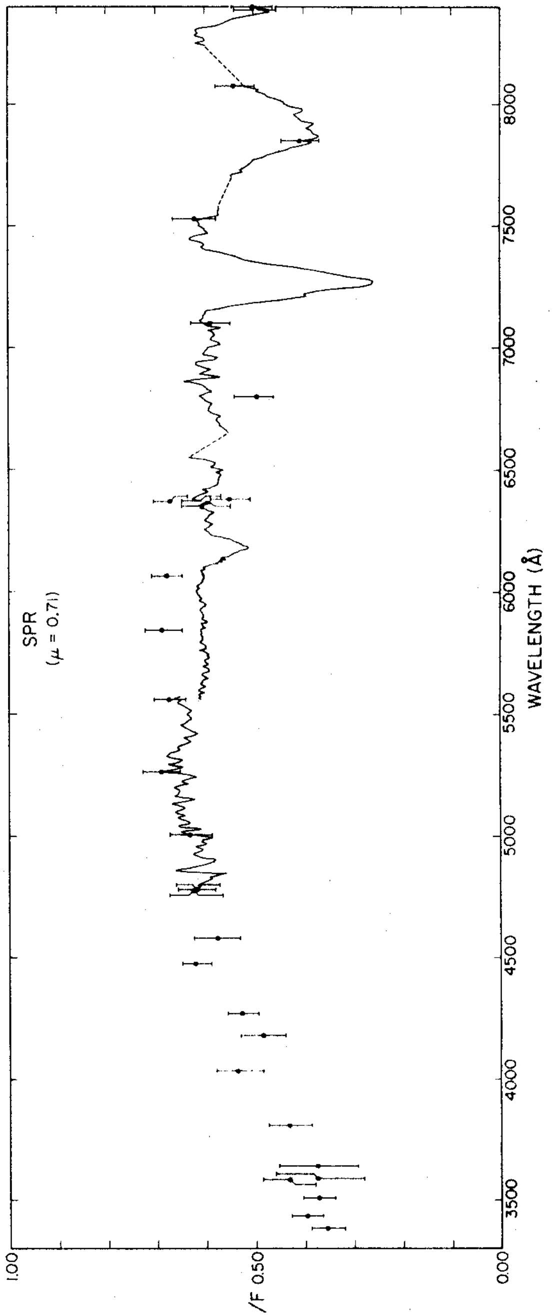

Fig. 7.(top) -Measured absolute spectral reflectivity of "North Polar Region".

Fig. 8.(bottom) -Measured absolute spectral reflectivity of "South Polar Region". In both figures, symbols as in figs. 2A and 2B.

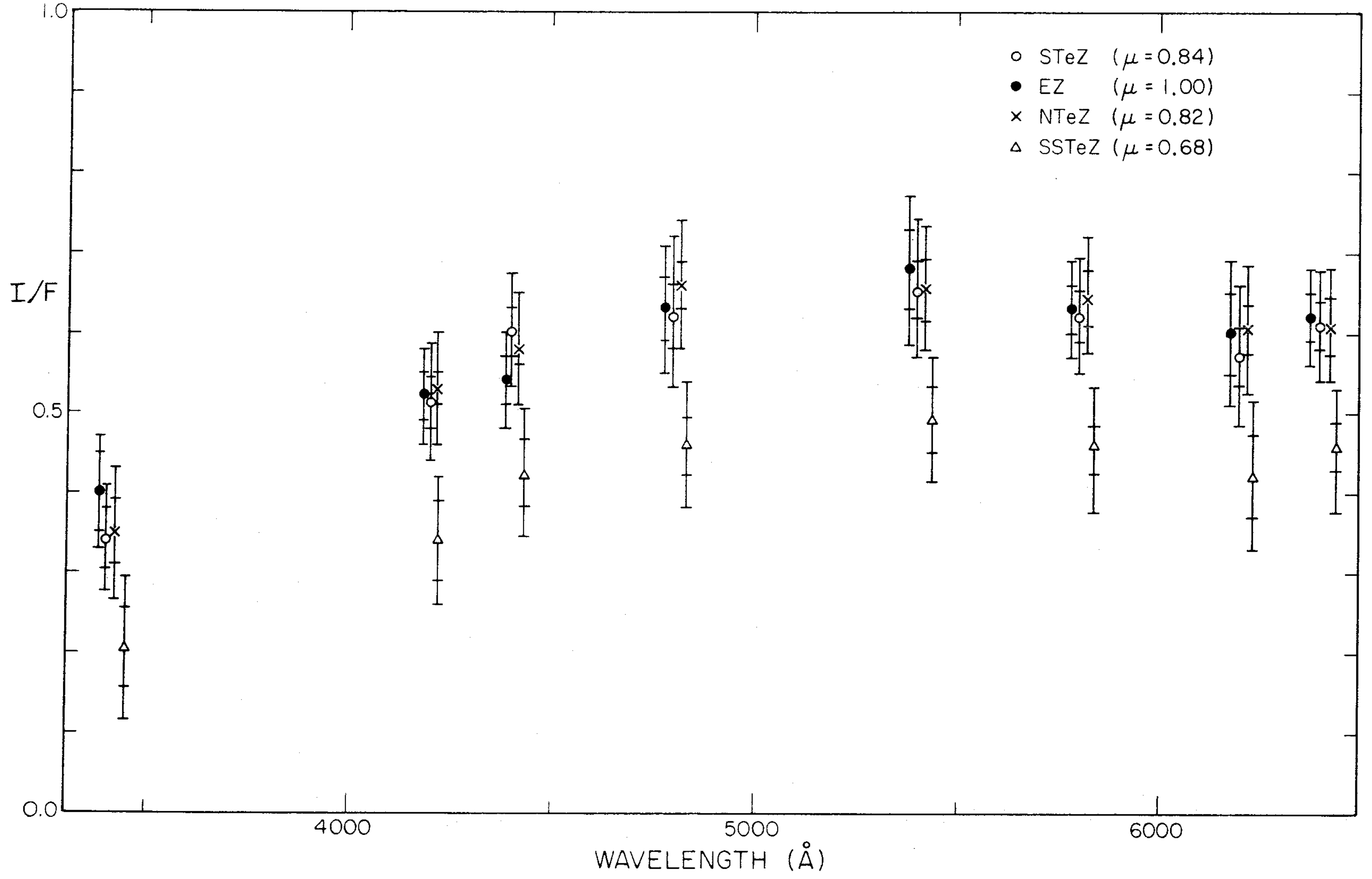

Fig. 9. -Measured absolute spectral reflectivity of South Temperate Zone, Equatorial Zone, North Temperate Zone and South South Temperate Zone. Observations with McCord photometer. Error bars as in figs. 2A and 2B.

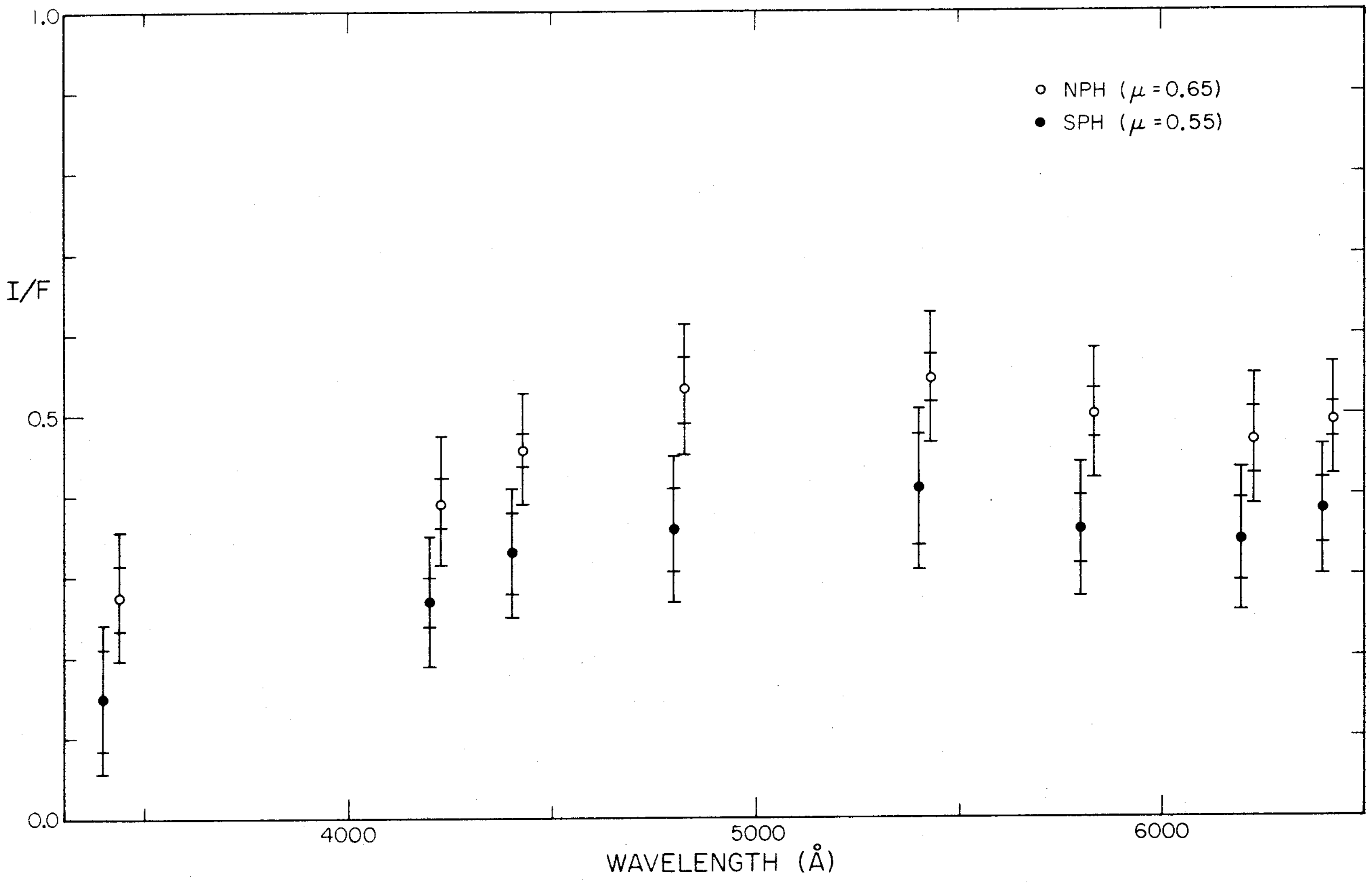

Fig. 10. -Measured absolute spectral reflectivity of North Polar Hood and South Polar Hood. Observations made with McCord photometer. Error bars as in figs. 2A and 2B.

at the set of standard wavelengths are indicated by the filled circles with appropriate error bars. McCord photometer measurements are indicated by the open circles with the double error bars.

Each figure shows the value of μ appropriate to the observations of the region. Data is missing from some wavelength regions as no opportunity was available to observe it in that wavelength region on more than a single night.

B. Error Analysis for the Observations

Errors in both the shape of the spectra and the absolute values assigned to the reflectivities are due, in part, to errors in the measurements made in the observations. These are summarized as errors in the observations of: (1) Jupiter, (2) the auxilliary standards (the Moon and J4), (3) the standard stars which are used to determine the spectral reflectivity of the auxilliary standards and the absolute reflectivity of Jupiter, (4) errors in the aperture position guidance, and (5) uncertainties in the determination of the aperture size and vignetting occurring in the optical path of the observing system.

Errors in the observations themselves, i.e. the actual photon count from each object, arise from two sources: (1) statistical errors and (2) variations in the transmission of the atmosphere with time. The value of the statistical error, relative to the observation, is $N^{-\frac{1}{2}}$, for an observation consisting of a total photon count of N. Therefore, a statistical error of 1% or less is achieved for $N \geq 10^4$. This criterion was met in almost all of the observations.

Estimates of the error resulting from time variations of the atmospheric transmission at each wavelength were made by observing the deviation of the observed flux of a Galilean satellite or of standard stars from a linear extinction curve in airmass. This is used as one of the criteria for the data quality of each night, as stated earlier. A conservative estimate of the error is made at each wavelength by taking the case of the worst deviation from linear extinction and considering this value as the error characterizing all data taken that night at the given wavelength. Not included in the consideration of "worst cases" were: (1) observations made in the early evening when the atmosphere is typically somewhat unsettled, (2) observations made at a time when the consistency of atmospheric transmission is deteriorating (e.g. due to changes in weather), and (3) observations made when the size of departures from linear extinction apparently increase with airmass (e.g. when haze or smog layers become significant contributors to extinction). (Observations made close to the above conditions were not used unless they met the 6% maximum deviation criterion given in the last section.)

The statistical errors are much less than the estimates of the error due to atmospheric transmission changes. Estimates of the latter extended from the 6% maximum allowed down to 2% (on one night), for the full range of wavelengths and nights of observation considered.

An individual reflectivity determination (for a particular region and wavelength) is defined as an observation of Jupiter referenced to a preceeding or subsequent observation of ε Aqr. It also includes the appropriate calibration defined by equations (1), (2), and (3). No more than three such determinations were made per night.

The mean reflectivity values shown in figures 2 - 10 are computed by weighting individual reflectivity determinations by the error estimates as computed immediately above. The errors displayed, however, do not represent the formal error of the mean, which was considered to be unrealistically low. Consistent with the policy of making conservative estimates of the error, the error bars displayed in these figures are large enough to enclose about 68% of all the individual reflectivity determinations. This conservative estimate is supported, in part, by the systematic nature of errors associated with the variation of atmospheric transmission from ideal conditions.

For mean reflectivity values determined from few individual data, the variation between individual values for the reflectivity is occasionally much smaller than the error estimate associated with the individual reflectivity determinations. As these never appear to be systematic in wavelength or in time, they are considered to be coincidental results of dealing with small numbers of data. In such cases, the estimated error for the mean reflectivity is computed as the average value of the error associated with the individual reflectivity determinations.

A measure of the variation of individual reflectivity determinations may be seen in: (1) the deviation of the scan measurements and standard wavelength measurements from each other; (2) the deviation of observations made with the Cassegrain scanner from each other at 3571, 4785, and 6370 Å, where individual observations overlap; and (3) the deviation of the McCord photometer measurements from the Cassegrain scanner measurements. These variation are largely consistent with the displayed error bars. Inconsistencies must be attributed to underestimates of the error associated with the atmospheric transmission quality of an individual night, or to difficulties in the resolution of individual regions.

The aperture position is usually well-centered on the individual region measured. When atmospheric seeing has made this difficult, no data were taken. For the Great Red Spot, however, the commensurability of the 4.20 arc second aperture and the size of the spot itself has made the problem of guidance quite difficult. This may account for the large variation of the reflectivity measured at 4785Å, for example.

One additional uncertainty resulting from the measurements must be discussed. Many of the scan measurements have been sampled less than twice for each resolution element (the Nyquist frequency). This has tended to create artificial variations in the reflectivities when strongly wavelength-dependent variations in the flux are measured and subsequently ratioed with similar variations in the solar spectrum, e.g. the vicinity of strong solar absorption lines for wavelengths near and somewhat less than 5500Å. This tendency appears in the spectra for which too few scan data are available to be included in the mean, e.g. spectra measured near the planetary limb.

The size of the aperture used in the Cassegrain scanner measurements of Jupiter has been very carefully measured. On the other hand, the aperture size used in the McCord photometer measurements is determined only with respect to the area of a larger aperture which has been accurately measured. This comparison has been made by comparing the flux observed from the same mare region of the moon, which is visibly homogeneous. The 7% uncertainty in this comparison accounts for the wider error bars associated with the open circles, representing the McCord photometer observations among figs. 2 - 10.

Two careful checks were made against vignetting, the interruption of the light received from the object somewhere in the optical train of the observing system, for both instruments. First, both instruments are designed so that a precise collimation of the beam is easily made and physically verified. Second, bright stars were scanned by the larger apertures, and the measured flux was always ascertained to be independent of position in the field of view before any observations were recorded.

The correlation of the reflectivities determined by both instruments is useful in demonstrating the total level of error expected, due to: (1) insufficiently accurate guidance of the aperture position on the region measured or insufficient spatial resolution of the Cassegrain scanner measurements, (2) errors in the estimates of the relative sizes of the apertures, or (3) vignetting in either system or systematic errors generated by observing narrow sources with apertures wider than those used in the observations of Jupiter.

C. Other Errors

Among the errors not included in those displayed in figs. 2 - 10 are: (1) errors in the flux of ϵ Aqr relative to α Lyr as measured by Oke (1964), (2) errors in the absolute flux scale of α Lyr, as determined by Oke and Schild (1970), and (3) errors in the spectral irradiance of the sun as measured by Arvesen et al. (1969).

Among these, the uncertainty of the measurements of the relative fluxes of standard stars by Oke (1964) is smallest and is expected to be no greater than 2%. The error quoted by Oke and Schild (1970) in the absolute flux calibration of α Lyr is 2%. Comparison with the calibration by Hayes (Hayes et al., 1970) shows agreement to within 2% for most wavelengths in this study. However, for wavelengths below about 4000Å and above about 8000Å, the results of Oke and Schild are some 5% brighter than those of Hayes.

Arvesen et al. (1969) quote a 3% accuracy in the absolute solar spectral irradiance measurements which they report over most of the 3390-8400Å range. Furthermore, Duncan (1969) has suggested a 2.5% decrease in the value of the solar flux derived from the measurements of Arvesen et al., due to a correction in the comparison lamp calibration. Code (1973) has compared estimates of the apparent visual magnitude of the sun by several observers with the results of integrating the Arvesen et al. data over the visual filter bandpass and calibration to the absolute scale of Oke and Schild. The average of these two results implies a total 3% uncertainty in the energy scale. Given all these uncertainties, it may be wisest to consider the solar irradiance values reliable to no better than 5%.

D. Phase Variations and Limb Darkening

Neither systematic long-term variations in the reflectivities of individual regions during the period of these observations, nor variations in the reflectivities with solar phase angle were detectable above the level of noise in the data. However, using a phase law for a linear change of 0.005 magnitudes/degree (Harris,1961; Irvine et al.,1968b) for the whole disk may be assumed. Subtracting out the approximate change in brightness with angle expected from the purely geometric effects of illumination, the data which are averaged together in figures 2 -10 may be individually corrected to 0° illumination. The net effect is to raise the reflectivity values for all the data shown by approximately 3%, independent of wavelength and position on the disk.

The limb data, near $\mu=0.70$, for various regions (figs. 2B, 3B, and 6B) show no significant asymmetry between different limbs of the planet above the level of observational error. The data may be used to make simple determinations of linear limb darkening coefficients as a function of wavelength. However, it is found that the uncertainties in the measured flux at the meridian, the flux near the limb, and the value of μ where flux was measured near the limb, combine to make the error in the derived value for a linear limb darkening coefficient a significant fraction of the value itself. These values are, therefore, not considered to be sufficiently well determined to be presented here.

Nevertheless, a wavelength-independent average of the coefficients may be used to estimate the increase in reflectivity from that measured at $\mu<1.00$ on the central meridian to $\mu=1.00$. For the equatorial belts, the increase is less than 1%, and for the tropical zones, it is about 3%. Thus, for the North and South Tropical Zones, the reflectivity at zero degrees phase and normal emission is about 6% higher than that illustrated in figs 2A and 3A, respectively. For the North and South Equatorial Belts, the reflectivities at zero degrees phase and normal emission is some 3% higher than the reflectivity illustrated in figs 4 and 5, respectively. Both changes are below the error bars of the measurements.

IV. DISCUSSION

A. Comparison of Various Regions

Of all the regions, the South Tropical Zone (STrZ) (fig. 2A) is the brightest over most visible wavelengths. In fig. 11 the reflectivities of the North Tropical Zone (NTrZ) (fig. 3A), the North Equatorial Belt (NEB) (fig. 4), the Great Red Spot (GRS) (fig. 6A), and the South Temperate Zone (STeZ) (fig. 9) are ratioed with the reflectivity of the STrZ at the standard wavelengths of the scanner measurements and the wavelengths of the fixed filter photometer. With the exception of the STeZ, the reflectivity of each of the regions in this figure appear to be quite similar to that of the STrZ for wavelengths greater than about 6500Å. Toward the ultraviolet, however, the reflectivity of each region is less than that of the STrZ. The region identified in fig. 1 as "NTrZ" is actually a composite of the reflectivity of the NTrZ, the NTeZ, and the North Temperate Belt (NTeB). The contribution of the latter region may account for the lower reflectivity of this region relative to the STrZ. However, the McCord photometer measurements (open circles) have presumably resolved the NTrZ with nearly identical results. The reflectivity of the NEB in the blue and ultraviolet is systematically, although only slightly, lower than that of the NTrZ.

If the measurements of the GRS at the standard wavelengths (which agree at 4785Å) are credible, then the reflectivity of the GRS appears to be similar to that of the NEB. Both ground-based and spacecraft measurements have shown a higher contrast, however, between the GRS and the surrounding STrZ in the blue and ultraviolet. Thus, it appears desirable to study the GRS using some technique which enables a greater degree of spatial resolution. Such a study would further remove the possible confusion of the GRS measurements shown here with the surrounding STrZ resulting from inadequate spatial resolution.

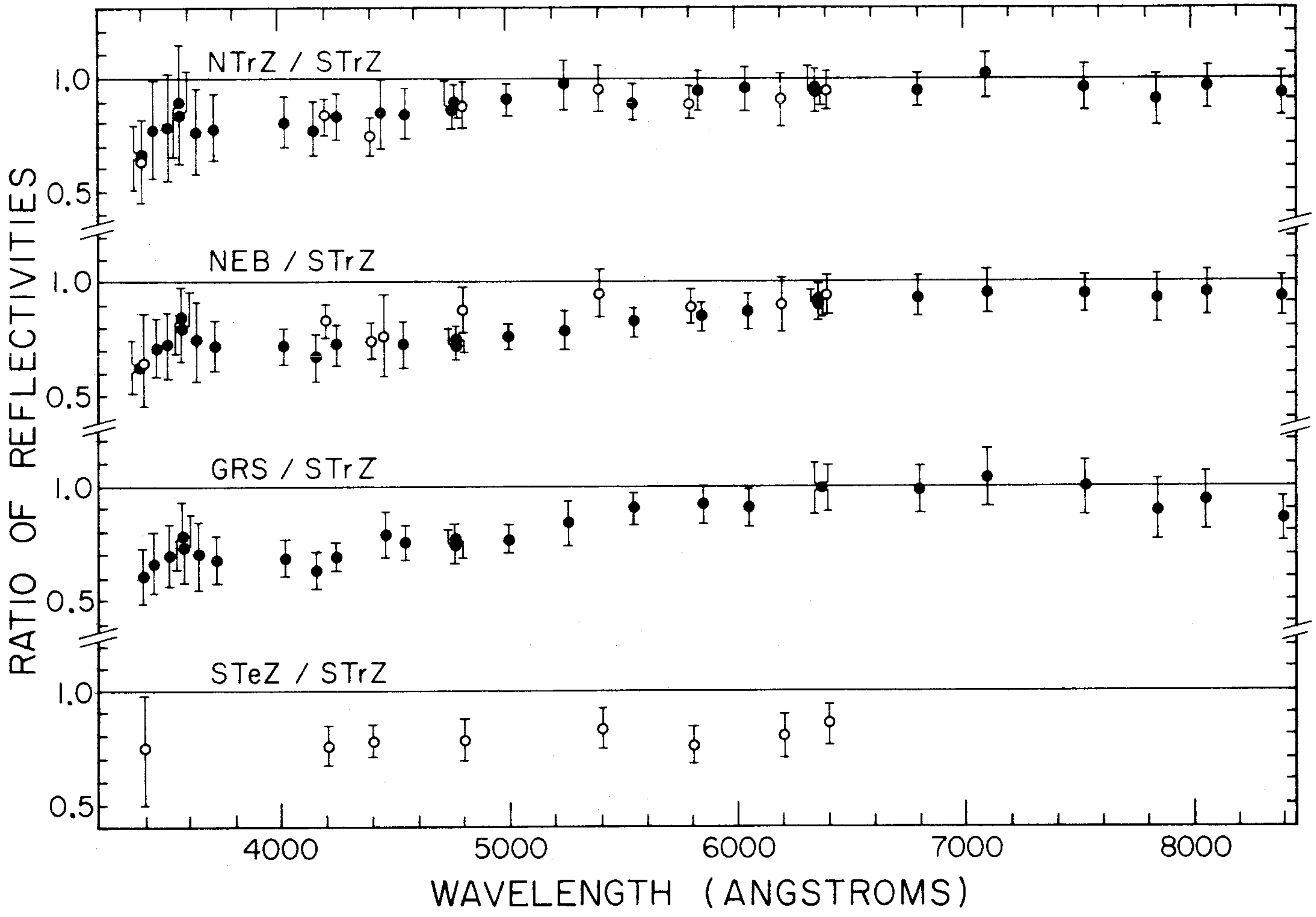

Fig. 11. -Reflectivities of four regions, relative to South Tropical Zone. Measurements with the Cassegrain scanner at standard wavelengths and McCord photometer are used in the comparison. Symbols as in figs. 2A and 2B.

TABLE 4

AVERAGE REFLECTIVITIES

OF EQUATORIAL REGIONS

Region (on meridian)	Average I/F (3390 - 8400 Å)
STrZ	0.76 ± 0.05
NTrZ	0.68 ± 0.08
SEB	0.63 ± 0.08
NEB	0.62 ± 0.04
GRS	0.64 ± 0.09

The reflectivity of the NEB (fig. 4) and the South Equatorial Belt (SEB) (fig. 5), are quite similar at all wavelengths. Fig. 9 demonstrates the similarity of the measured reflectivities of the STeZ, the Equatorial Zone (EZ), and the North Temperate Zone (NTeZ) at all wavelengths where measurements were taken with the fixed filter photometer. The South South Temperate Zone (SSTeZ), also shown in fig. 9, appears to be some 25-40% dimmer. This may be due either to closer proximity to the limb or to incomplete resolution of the region, rather than to any real difference in the reflectivities of the SSTeZ and the other regions displayed in fig. 9.

B. Average Reflectivity and Equivalent Broad-Band Reflectivity

The reflectivity measurements shown in figs. 2-6 have been averaged over 3390 - 8400Å, weighted by the solar irradiance at each wavelength. This wavelength range includes about 65% of the total solar intensity. These values are listed for the regions close to the equator in Table 4. Where necessary, a smooth curve has been fit through the fixed wavelength data for $\lambda \leqslant 4785Å$, where no scan data exists. The remainder is derived from an average of scan and fixed wavelength measurements, with appropriate consideration of absorption lines in the spectra. Error estimates are derived from the measurement uncertainties.

As expected, the STrZ is the brightest region. The NEB, SEB, and the GRS display similar averages. The NTrZ reflectivity is intermediate between the reflectivity of the STrZ and the reflectivities of the NEB, SEB, and GRS.

In support of the imaging photopolarimeter measurements of Pioneers 10 and 11, the reflectivity measurements shown in fig. 2-8 have been folded into the blue and red filter transmission functions of the spacecraft experiment (Pellicori et al., 1973; Coffeen, 1973). These values are listed in Table 5.

TABLE 5

EQUIVALENT REFLECTIVITIES FOR BLUE AND RED CHANNELS OF PIONEER IMAGING PHOTOPOLARIMETER

Region (on meridian)	$(I/F)_{blue}$	$(I/F)_{red}$
STrZ	0.70±0.05	0.78±0.04
NTrZ	0.58±0.06	0.72±0.05
SEB	0.52±0.10	0.68±0.04
NEB	0.53±0.05	0.68±0.04
GRS	0.48±0.10	0.72±0.06
SPR	0.56±0.08	0.60±0.07
NPR	——	0.54±0.07

Reflectivity values at each wavelength and errors are derived similarly to the computation of Table 4.

Comparison with Pioneer 10 imaging photopolarimeter data is not made here. The limited contrast data published at the date of this writing (Coffeen, 1974) is taken from a phase angle significantly different from zero. Significant effects take place, therefore, due solely to variation of distance from the terminator. Differences due to the polarization of the instrument may also be present.

C. Comparison with Previous Results

Fig. 12 displays a comparison of the reflectivity measurements of this study (for discrete wavelengths) with the equivalent results of PPM over corresponding bandpasses. PPM do not include measurements between 5000 and 6000Å. The error bars displayed in fig. 12 represent the uncertainty of the measurements reported here and the variation of successive measurements by PPM. (For the NTrZ at $\lambda \leq 6000$Å, PPM display only one scan. Therefore, the error bars shown represent only the uncertainties in the measurements reported here.)

For $\lambda \leq 5000$Å, the measurements reported in this paper are similar to those of PPM within the error bars. The reflectivity of each region is at least marginally higher than measured by PPM just above 6000Å.

The two greatest differences from the PPM measurements are the EZ and the STrZ results. Both regions are less reflective than measured by PPM.

For the EZ, this difference may be due to time variations of the longitude at which the single set of measurements reported here was made. Highly resolved ground-based and Pioneer 10 photopolarimeter visible images of the planet (Swindell and Doose, 1974) show significant inhomogeneities in the

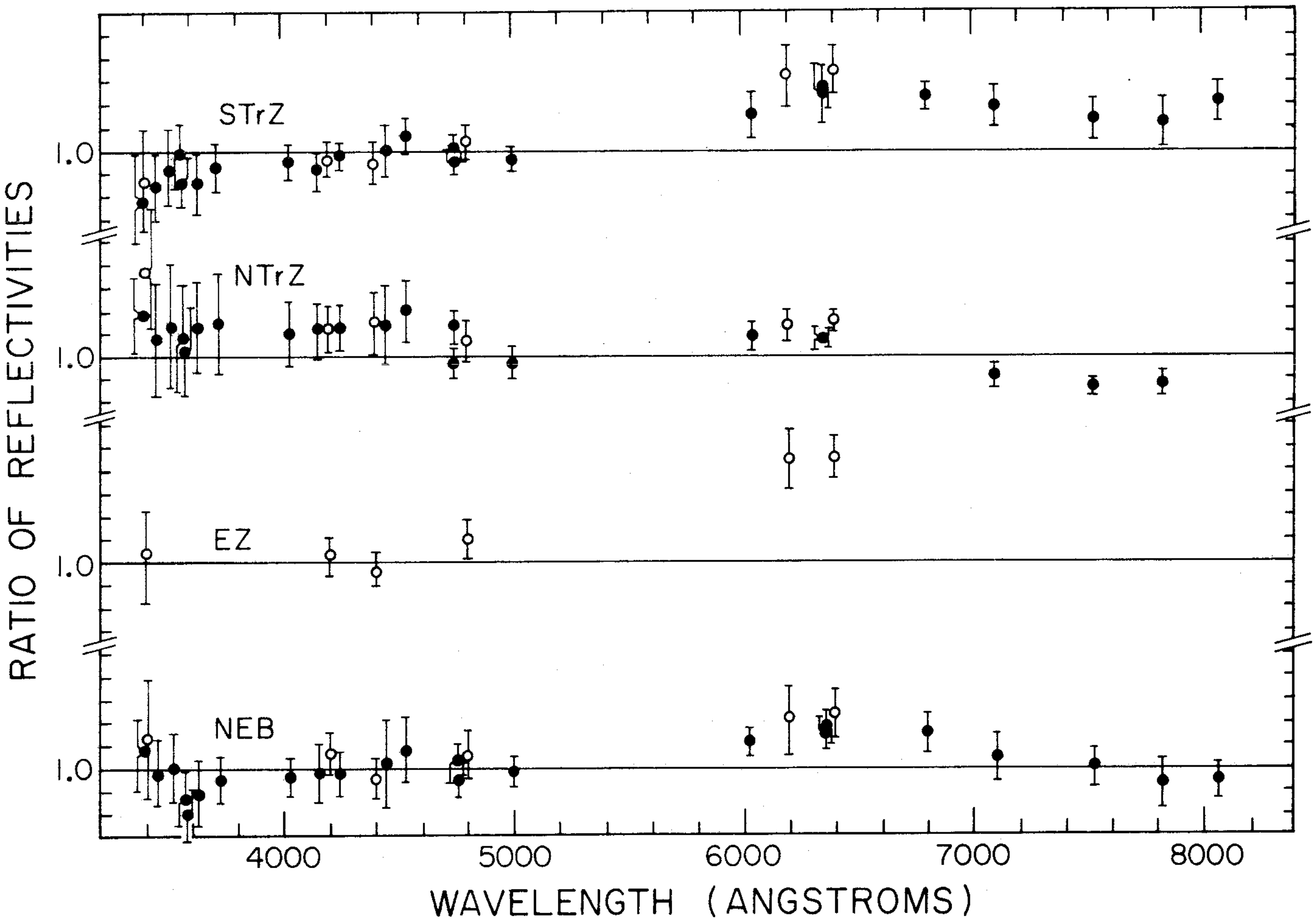

Fig. 12. -Absolute reflectivities of four regions relative to earlier measurements of Pilcher, et al. (1973). Standard wavelength measurements of Cassegrain scanner and Mc Cord photometer measurements are used in the comparison with the earlier measurements over appropriate bandpasses. Symbols as in figs. 2A and 2B.

narrow latitude region defined as the EZ.

The STrZ measurements may be less subject to the considerations of short term time variability, as they were taken over an extended period of time. None of the individual measurements which contribute to the average shown in fig. 2A (including: 3 scans and 3 sets of observations at the standard wavelengths for $\lambda \leq 4785 Å$, 8 scans and 3 sets of observations at the standard wavelengths for $\lambda \geq 4785 Å$, and 1 set of observations with the McCord photometer) displays a reflectivity as high as that measured by PPM for $\lambda \geq 6000 Å$. These results are credible to the extent that they are confirmed by observations using both photometers.

Such differences, if not due to the differences in calibration techniques used, must be attributed to time variations in the reflectivity of this region and may also be affected by the properties of the central thin belt dividing the north and south sections of the STrZ. Further monitoring of the reflectivity of this and other regions is recommended, as well as attempts at greater spatial resolution.

The corresponding values for the isotropic single scattering albedo of the EZ and the STrZ at 6370Å and 8150Å (the positions of the S(1) lines in the 4-0 and 3-0 H_2 quadrupole bands, respectively) are lower than those given in Table 3 of PPM. Using the scale in figs. 1 - 3 of PPM, the values for the isotropic single scattering albedos of the EZ (using a smooth curve through the discrete measurements) and the STrZ are given in Table 6.

D. Equivalent Widths and Depths of Bands

Reliable information about the equivalent widths and depths of the

TABLE 6

ISOTROPIC SINGLE-SCATTERING ALBEDOS OF THE CONTINUUM

Region	6370Å	8150Å
EZ (meridian)	0.979 (I/F=0.62)	———
STrZ (meridian)	0.993 (I/F=0.79)	0.992 (I/F=0.77)

6190Å CH_4, the 7250Å CH_4, and the 7900Å NH_3 bands is contained in the measured spectra. (The 6450Å NH_3 band is omitted from consideration because the difference between the reflectivity at the band center and the nearby continuum is on the order or less than the error of the measurements.) The equivalent width and the depth, respectively , are defined as

$$W = \int_{\Delta\lambda(\text{band})} \left[\frac{(I/F)_{\text{continuum}} - (I/F)_{\text{band}}}{(I/F)_{\text{continuum}}} \right] d\lambda \qquad (4)$$

$$D = 1 - \text{MIN} \left[(I/F)_{\text{band}} \; / \; (I/F)_{\text{continuum}} \right] \qquad (5)$$

These values are tabulated in Table 7 for each of the spectra shown in figs. 2 - 8. They are determined by averaging the results of measurements of the individual spectra which comprise the results shown in the figures. In this way, the uncertainty resulting from the variation of absolute reflectivities from one measurement to the next is not included in the uncertainty of the width and depth measurements.

The uncertainty in the values of the band widths and depths shown in Table 7 results almost entirely from the uncertainty in the assumed value of the continuous reflectivity. Additional uncertainty in the equivalent width of the 7900Å NH_3 line results from the unknown shape of the absorption at wavelengths of strong telluric absorption. The band depth is included, even though it is less directly useful than information about the equivalent width, as it is less affected by the uncertainty in the value of the continuum reflectivity near the band.

TABLE 7

EQUIVALENT WIDTHS AND LINE DEPTHS

Region	6190Å:CH$_4$		7250Å:CH$_4$		7900Å:NH$_3$	
	W(Å)	D	W(Å)	D	W(Å)	D
STrZ (meridian)	14±2	0.15±.02	77±5	0.56±.01	90±10	0.32±.02
STrZ (limb)	12±3	0.11±.03	82±8	0.59±.03	83±12	0.30±.05
NEB (meridian)	13±2	0.18±.02	85±7	0.60±.01	90 ±9	0.30±.02
GRS (meridian)	16±2	0.17±.02	74±4	0.53±.02	95±10	0.31±.02
GRS (limb)	14±1	0.17±.02	—	—	—	—
NTrZ (meridian)	15±2	0.17±.01	86±5	0.64±.02	87±10	0.29±.03
NTrZ (limb)	10±3	0.14±.03	95±7	0.67±.03	80±10	0.26±.04
SEB (meridian)	16±2	0.19±.02	78±7	0.52±.02	90±10	0.29±.03
SPR	18±4	0.15±.03	73±5	0.58±.03	109±15	0.30±.03
NPR	12±2	0.17±.02	92±13	0.60±.02	101±13	0.30±.04

As in PPM, there appear to be few correlations between the widths or depths of bands between belts and zones in general. However, for all regions, the equivalent width (and depth) drops from center to limb for the 6190Å CH_4 and 7900Å NH_3 bands. Alternately, for all regions, the width (and depth) increases from center to limb for the 7250Å CH_4 band. Unfortunately, these increases are on the order of or barely above the uncertainty of the measurements, but they do appear to be consistent from region to region.

While the equivalent width for the 6190Å CH_4 line is slightly larger than that quoted by PPM for the NTrZ, the NEB, and the STrZ, it is much lower than the values, ranging from 20.4 to 35.0, given by Teifel (1969a, 1969b) or Bugaenko et al. (1971) (Table 5 of PPM). The 7250Å CH_4 band equivalent width is close to the values given by PPM, Teifel, and Bugaenko et al. The 6190Å band measurements indicate real variations in time (or differences in the manner in which the reflectivity of the continuum has been defined). Variations in equivalent widths are noted on an even shorter time scale for H_2 quadrupole bands (Hunt and Bergstralh, 1974). These variations indicate real changes in the type and distribution of scatterers in the Jovian atmosphere.

E. Future Work

Continuing work should be done to achieve higher spatial resolution in order both to: (1) seperate reflectivities of regions defined by narrow latitude (and longitude) ranges, and (2) provide accurate limb structure measurements, over a wide range of wavelengths.

The limb structure work may be useful in the determination of the geometric albedo of separate regions. A reliable value for the phase integral may be obtained from the Pioneer 10 and 11 imaging photopolarimeter data (Tomasko et al, 1974). Thus, a reliable estimate may be made for the spatially resolved Bond albedo.

Measurements of limb structure may be made with presently existing images of Jupiter at high spatial resolution over a wide wavelength range (Terrile and Westphal, 1974). With data for the spatially resolved thermal emission from the Pioneer 10 and 11 infrared radiometer measurements (Part 2 of this thesis), estimates of the net energy output and the lateral exchange of thermal energy between adjacent regions may be made. Such comparisons may provide an important constraint on the existing planetwide and local atmospheric circulation system for Jupiter.

REFERENCES

Arvesen, J.C., Griffin, R.N. and Pearson, B.D. 1969, "Determination of Extraterrestrial Solar Spectral Irradiance from a Research Aircraft." Appl.Opt., 8, 2215-2232.

Bugaenko, L.A., Galkin, L.S. and Morozhenko, A.V. 1971,"Spectrophotometric Studies of the Giant Planets." Soviet Astronomy - A.J., 141,1184-1205.

Code, A.D. 1973,"Ground Based and Extraterrestrial Observations of Stellar Flux." in Problems of Calibration of Absolute Magnitude and Temperature of Stars, ed. B. Hauck and B.E. Westerlund, Reidel, New York, pp. 131-145.

Coffeen, D.L. 1973,"Pioneer 10 Observations of Jupiter: An Appeal for Ground-Based Coverage." Icarus, 20, 52-53.

Coffeen, D.L. 1974, "Optical Polarization Measurements of the Jupiter Atmosphere at 103° Phase Angle." J. Geophys. Res., 79, 3645-3652.

Duncan, C.H. 1969, "Radiation Scales and the Solar Constant." Goddard Space Flight Center Report, Number X-713-69-382, Greenbelt, Md.

Harris, D.L. 1961, "Photometry and Colorimetry of Planets and Satellites." in Planets and Satellites, ed. G.P. Kuiper and B.M. Middlehurst, Univ. of Chicago Press , Chicago, chapter 8.

Hayes, D.S., Oke, J.B. and Schild R.E. 1970, "A Comparison of the Heidelberg and NBS-Palomar Spectrophotometric Calibrations." Astrophys. J., 162, 361-362.

Hunt, G.E. and Bergstralh, J.T. 1974, "Structure of the Visible Jovian Clouds." Nature, 249, 635-636.

Irvine, W.M., Simon, T., Menzel, D.H., Charon, J., Laconte, G., Griboval, P. and Young, A.T. 1968a,"Multicolor Photoelectric Photometry of the Bright Planets. II. Observations from Le Houga Observatory." Astron. J., 73, 251-264.

Irvine, W.M., Simon, T., Menzel, D.H., Pikoos, C. and Young, A.T. 1968b, "Multicolor Photoelectric Photometry of the Bright Planets. III. Observations from Boyden Observatory." Astron. J., 73, 807-828.

McCord, T.B. 1968a,"A Double Beam Astronomical Photometer." Appl. Opt., 7, 475-478.

McCord, T.B. 1968b, "Color Differences on the Lunar Surface." Ph.D. Thesis, California Institute of Technology.

Oke, J.B. 1964, "Photoelectric Photometry of Stars Suitable for Standards." Astrophys. J., 140, 689-693.

Oke, J.B. and Schild, R.E. 1970, "The Absolute Spectral Energy Distribution of Alpha Lyrae." Astrophys. J., 161, 1015-1023.

Pellicori, S.F., Russell, E.E. and Watts, L.A. 1973, "Pioneer Imaging Photopolarimeter Optical System." Appl. Opt., 12, 1246-1258.

Pilcher, C.B., Prinn, R.G. and McCord, T.B. 1973, "Spectroscopy of Jupiter: 3200 to 11,200Å." J. Atmos. Sci., 30, 302-307.

Swindell, W. and Doose, L.R. 1974, "The Imaging Experiment on Pioneer 10." J. Geophys. Res., 79, 3634-3644.

Taylor, D.J. 1965, "Spectrophotometry of Jupiter's 3400-10000Å Spectrum and a Bolometric Albedo for Jupiter." Icarus, 4, 362-373.

Teifel, V.G. 1969, "Molecular Absorption and Possible Structure of the Clouds of Jupiter and Saturn." J. Atmos. Sci., 26, 854-859.

Terrile, R.J. and Westphal, J.A. 1974, private communication.

Tomasko, M.G., Clements, A.E. and Castillo, N.D. 1974, "Limb Darkening of Two Latitudes of Jupiter at Phase Angles of 34° and 109°." *J. Geophys. Res.*, *79*, 3653-3660.

The page number 46 has been omitted inadvertently.
No part of the text is missing.

PART 2

THE JOVIAN THERMAL STRUCTURE
FROM PIONEER 10 INFRARED RADIOMETER DATA

I. INTRODUCTION

This paper will present some of the data retrieved by the infrared radiometer on board the Pioneer 10 spacecraft. The planet has been mapped in two channels: a "short wavelength" channel with a bandpass centered close to 20 microns and a "long wavelength" channel with a bandpass centered close to 40 microns. Preliminary results and a description of the intrumentation is given by Chase et al. (1974). The experiment was designed to provide a measure of the relative abundances of H_2 and He and of the net energy output of the planet, as described in Hunten and Münch (1973). These determinations rely on a family of model atmospheres, as calculated by Trafton (1967), based on considerations of radiative-convective equilibrium. The work presented here has been motivated, in part, by differences between the limb structure observed and that predicted by Trafton's models.

This paper presents simple models of the atmospheric thermal structure which are consistent with data from both channels. Some bounds on the relative abundance of helium and molecular hydrogen are also made, as hydrogen is assumed to be the major opacity source at these wavelengths, and the relative opacity of both channels is influenced by the amount of helium present in the atmosphere. The models are <u>not</u> constrained to considerations of radiative equilibrium, but only to local thermodynamic equilibrium and to convective equilibrium below the region to which the most transparent channel (40 micron) is sensitive. An attempt has been made to make the models independent from others in the literature. This is not entirely possible in devising the thermal structure above the region to which the most opaque channel (20 micron) is sensitive. The effect of different assumptions regarding this overlying structure is discussed. The results are compared with various other models which are derived from inversion of thermal emission at various wavelengths and from considerations of radiative-convective equilibrium. Finally, the implications of the spectra resulting from the models are discussed, especially with respect to the effective temperature of the planet.

II. DATA

During the approximately two hour period in which the radiometer measurements were made, a complete "image" of the planet was obtained in each channel. The latitude and longitude grid of these images was calculated using the spacecraft trajectory along with information about the viewing angle of each channel, the spin rate, and roll timing supplied by the spacecraft. A somewhat more detailed description of these calculations, along with a discussion of the correlation of the images with data at other wavelengths, will be published in a separate paper. The data presented in this paper are the unsmoothed data retrieved by the radiometer, separated into "bins" defined by latitude. It is unlikely that any point on the planet was observed more than once. Therefore, when data from a given latitude bin is discussed as characteristic of a given feature of the planet, the assumption of longitudinal homogeneity must be made. The ramifications of this assumption for the latitude bins examined will be discussed in more detail.

Figure 1 shows the sensitivity characteristics of the two channels used in the observations. In this paper, the shorter and longer wavelength channels will be referred to as the 20 and the 40 micron channels, respectively. Figures 2-5 display the data used in the derivation of the temperature profiles. The data numbers returned from each channel by the spacecraft are directly proportional to the intensity observed in each channel as follows:

$$\mathrm{DN}\ (40\ \mu\mathrm{m}) = F_{40\mu\mathrm{m}}(\mathrm{erg/s/cm^2/ster/\mu m})/5.28409 \qquad (1)$$

$$\mathrm{DN}\ (20\ \mu\mathrm{m}) = F_{20\mu\mathrm{m}}(\mathrm{erg/s/cm^2/ster/\mu m})/16.8518 \qquad (2)$$

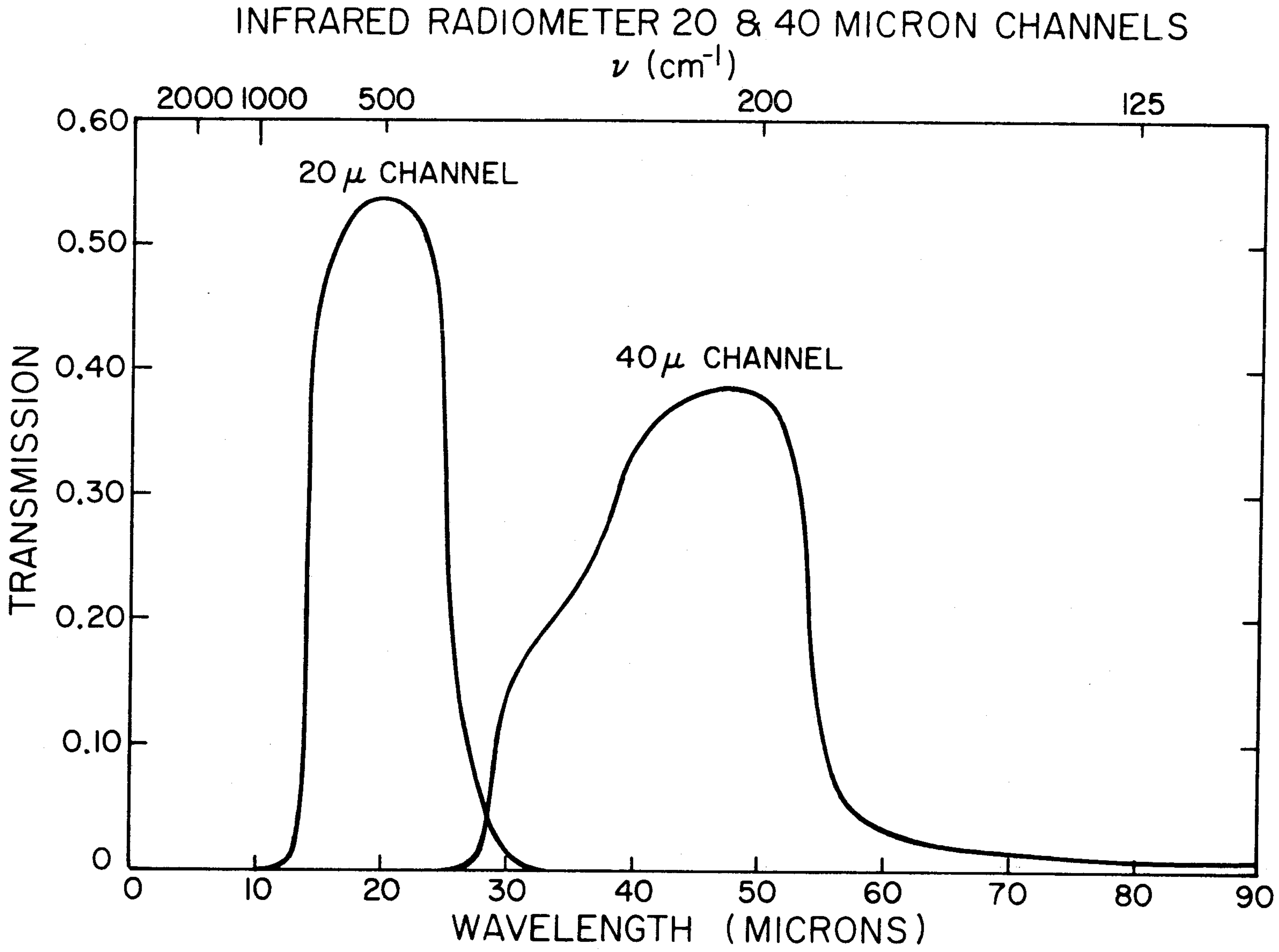

Fig. 1. - Transmission characteristics of Pioneer 10 infrared radiometer channels. The transmission is shown on an absolute scale.

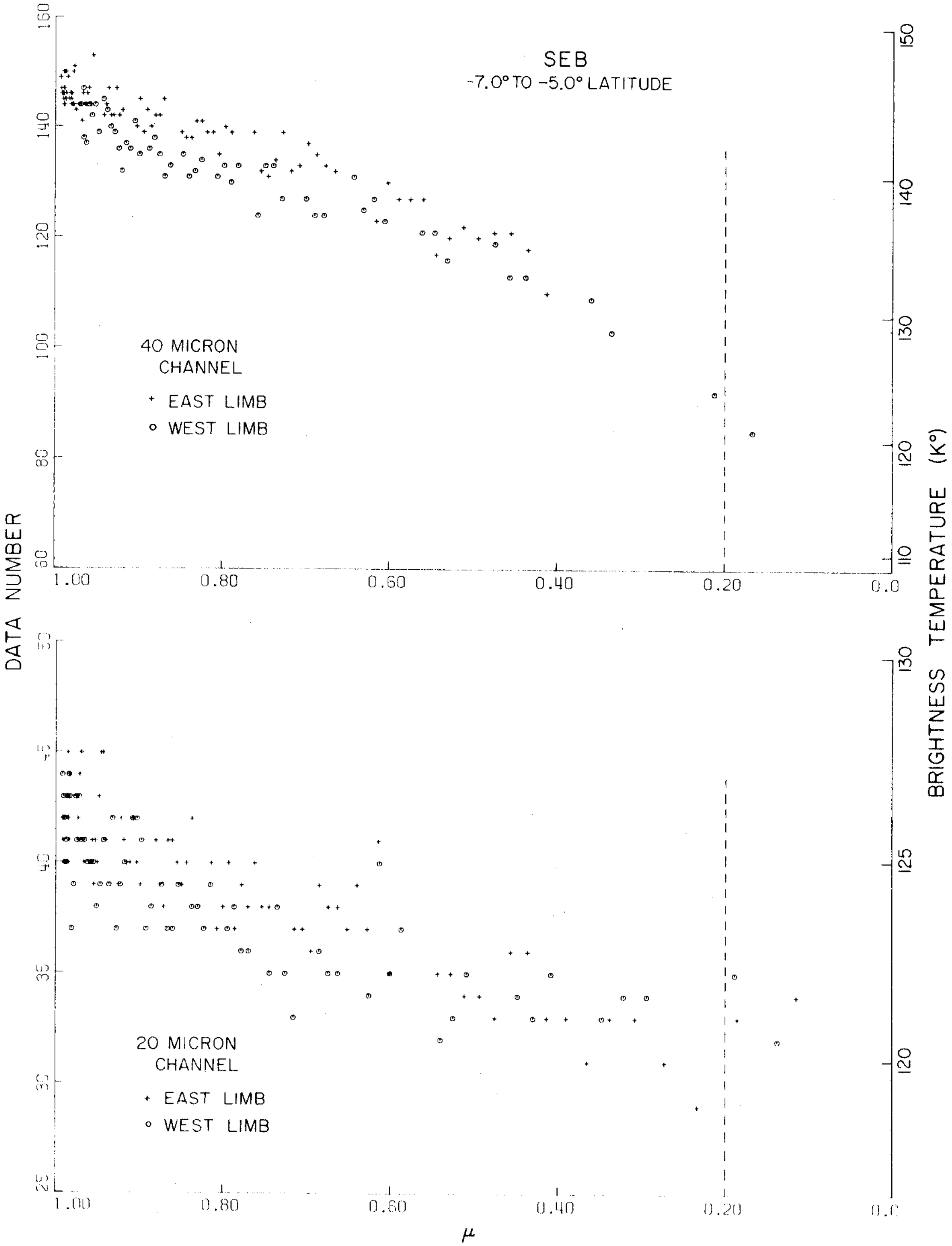

Fig. 2. - Data for latitude range of the South Equatorial Belt. μ is the cosine of the local emission angle. "East limb" and "west limb" refer, respectively, to locations to the Jovian eastward and westward side of the subspacecraft point. The dashed vertical line signifies that no data are considered for $\mu < 0.20$.

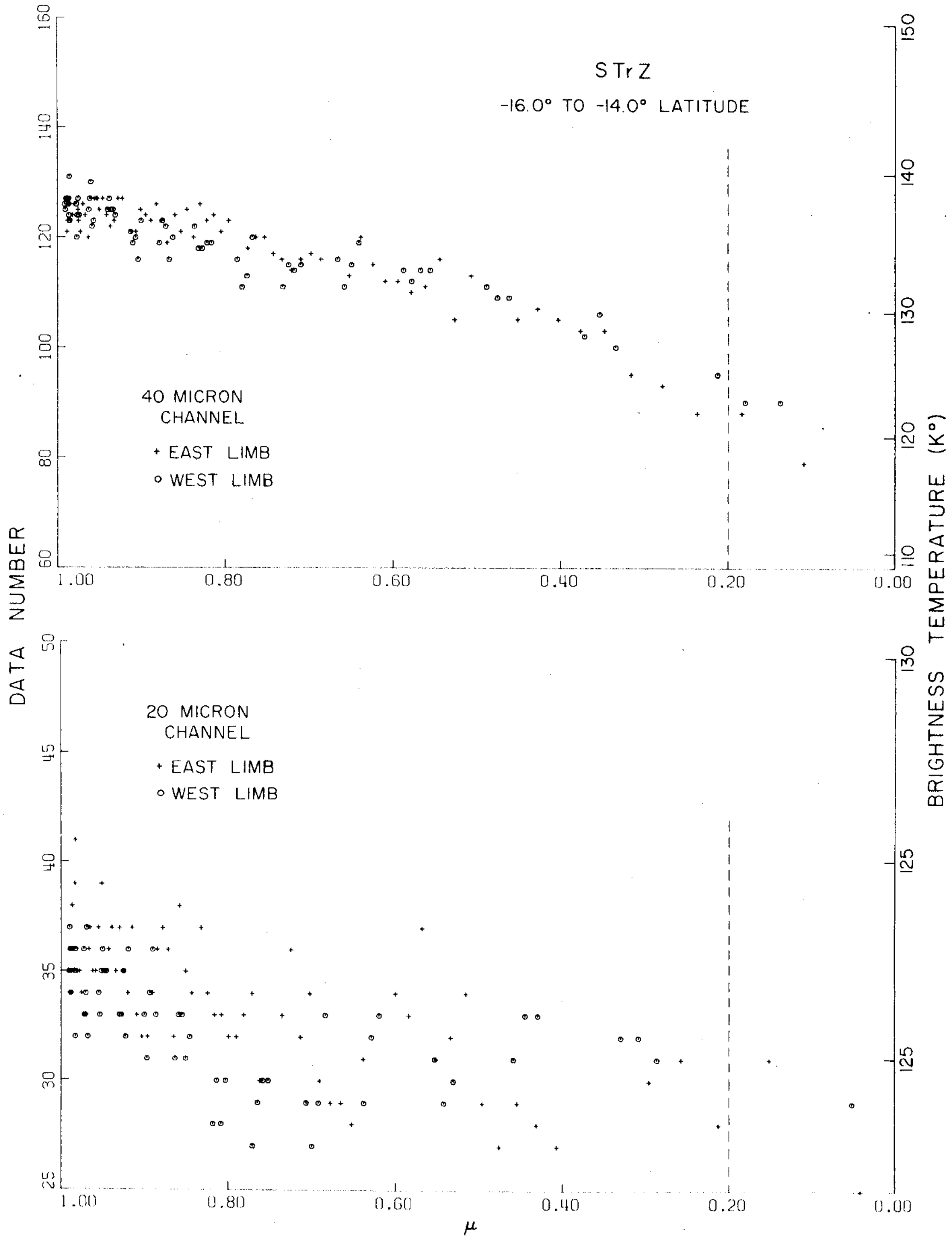

Fig. 3. - Data for latitude range of the northern part of the South Tropical Zone. Symbols are the same as in Fig. 2.

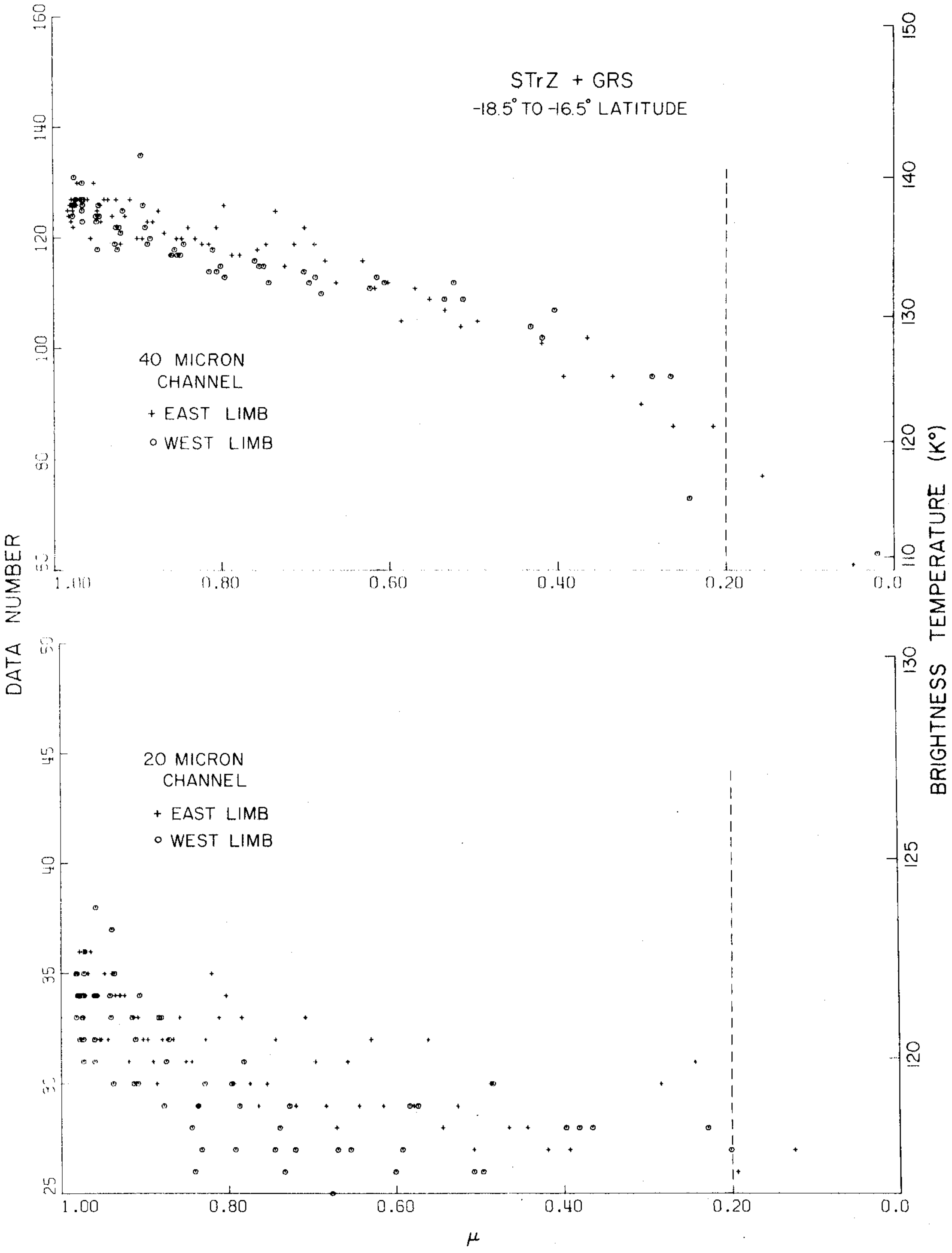

Fig. 4. - Data for latitude range of the southern part of the South Tropical Zone and of the Great Red Spot. Symbols are the same as in Fig. 2.

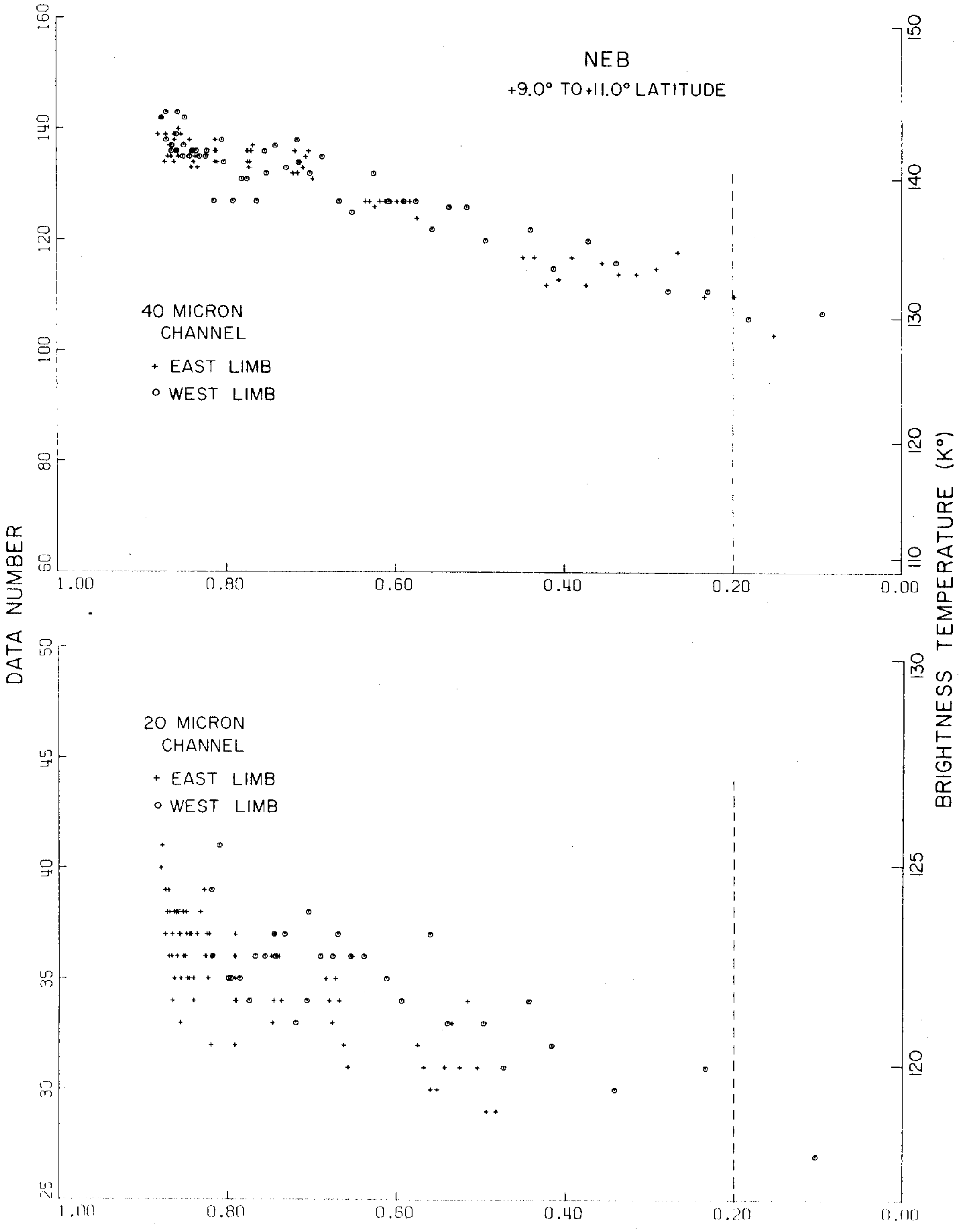

Fig. 5. - Data for latitude range of the North Equatorial Belt. Symbols are the same as in Fig. 2.

On the right hand ordinate scale are the equivalent black body brightness temperatures corresponding to the intensity values displayed on the left-hand ordinate scale as data numbers. The intensities are plotted against μ, the cosine of the local emission angle.

Of primary consideration are the data for latitudes corresponding to the position of the South Equatorial Belt (SEB) in fig. 2 and the South Tropical Zone (STrZ) in fig. 3. We shall discuss the STrZ data for a latitude band which contains the Great Red Spot (GRS) on the western limb in fig. 4, as well as the correlation between data from the SEB and the North Equatorial Belt (NEB) in fig. 5. The viewing angle of the spacecraft placed the SEB and STrZ close to the apparent disk center. The data corresponding to the positions of both these features is, therefore, least susceptible to the alignment of the image with the true position of the center of the planet. Differences in the behavior of the intensity as a function of μ within the STrZ and comparisons between the SEB and the NEB will be discussed further. The resolution of the scans in latitudes is about 2 degrees for the SEB and the STrZ, and is somewhat larger for the NEB data. In each of figures 2-5, the resolution element is smaller than the width of the feature under observation. The resolution element of the radiometer is effectively 0.3 degrees by 1.0. The long dimension is in the direction of the spacecraft roll, which is oriented roughly north-south on the planet. Considerations of spacecraft geometry during the period when data were taken lead to the conclusion that points no closer to the edge of the disk than $\mu = 0.20$ should be considered because of possible confusion with regions beyond the edge of the planet. Such a restriction does not seriously limit the range of data available, as seen in figs. 2-5. A marker has been placed in these figures to show that data have not been considered for values of $\mu \leq 0.20$.

Figures 2 and 3 show differences in the intensity received from the SEB and the STrZ. In each channel, at all values of μ, the intensity orginating from the zone is lower than the corresponding value for the belt. The NEB (fig. 5) appears like the SEB in the 40 micron channel, but is somewhat cooler in the 20 micron channel toward the planetary limb (low values of μ). The influence of the GRS can be seen in fig. 4 at $\mu \approx 0.75$ as a 2°K cooling in the 20 micron channel, with respect to a corresponding position on the east limb of the planet.

The ground-based observations of Murphy and Fesen (1974) are sensitive to a wavelength range (17-28 microns) close to that of the 20 micron channel of this experiment. Their meridional scans of the planet show a mean central brightness temperature of 136°K and a belt-to-zone contrast of about 14%. The Pioneer 10 observed brightness temperature of 127°K in the 20 micron channel in the SEB center, the brightest observed area, is significantly lower than their value, although our measured intensity contrast is close to 30%. The reduction in the intensity contrast in their observations may easily be due to the lack of spatial resolution in the ground-based observations with respect to that available in our data. The high value of the brightness temperature may be due to calibration errors in either of the systems or to real time changes in the emission characteristics of the relevant section of the planet. Murphy and Fesen also observe greater limb darkening in their east-west scans, but this may be due, again, to the poorer spatial resolution available in the ground-based measurements. Low's (1969) whole disk brightness temperature for a similar bandpass is 126°K, and his value of intensity near the equator over the belts (Low, 1966) is a relatively high 150°K. For both sets of observations, our 20 micron channel results are relatively low. Once again, this must be attributed to either calibration errors in any of the observations or to real time changes in the emission characteristics of the planet.

III. METHOD OF ANALYSIS

This section provides a description of the assumptions made and the numerical routine used in calculating the intensity of radiation emerging from the top of a model atmosphere. In addition, the information content of the data with respect to the thermal structure and chemical composition is demonstrated. Finally, the method by which the thermal profile was derived from the data is briefly outlined. The results of this inversion procedure are given in the next section.

A. The Thermal Structure

The vertical temperature structure is considered free to vary and consists of a series of heights with the temperature specified at each height. The initial height is considered a reference level and is set arbitrarily to zero; the pressure at this level is specified as a free parameter. The temperature at an arbitrary height between grid points is determined by linear interpolation. Above the region where the temperature is specified, the atmosphere is considered to be isothermal at the temperature of the highest point specified in the grid. Below the given temperature grid, the atmosphere is assumed to be in convective equilibrium and the variation of temperature and pressure with depth are assumed to follow an adiabatic relationship consistent with the chemical composition. The pressure and density are determined by integrating upward from the reference level with the equation of hydrostatic equilibrium consistent with the ideal gas equation of state. This technique is used in the overlying isothermal region also. These are then converted to a final grid of even height intervals with appropriate thermodynamic parameters specified at each.

The temperatures and pressures are established on a grid of even height intervals in the adiabat using the assumption of hydrostatic equilibrium and the appropriate thermodynamic relationships. These depend on the local gravitational acceleration and the effective specific heat at constant pressure, c_p, for the mixture. The gravitational acceleration is assumed constant and equal to 2280 cm/s^2, a value taken from Newburn and Gulkis (1972), § I , which is appropriate for equatorial regions. The effective specific heat of hydrogen is determined at each level by the equilibrium value for the ortho- and para-states of molecular hydrogen at the temperature of that level, interpolating Table #7 of Trafton (1967).

B. Chemical Composition

H_2, He, and CH_4 are assumed to be uniformly mixed throughout the atmosphere, so that their partial pressures are a constant fraction of the total pressure. Ammonia, however, reaches saturation at levels close to those from which the detected radiation originates. The NH_3 mixing ratio is specified at the deepest level of the model and it is assumed to be uniformly mixed for all higher levels where the saturation vapor pressure exceeds the partial pressure. Where the partial pressure tends to exceed the saturation vapor pressure, however, it is set to the value of the saturation vapor pressure to the total pressure. If the partial pressure at any level does not exceed the saturation vapor pressure, the molar fraction of ammonia is set to the value of the level immediately below it, with which it is assumed to equilibrate. Following Lasker (1963), the saturation vapor pressure of NH_3 is given by:

$$P_{sat} = A \cdot \exp\ (\nu/\theta) \qquad (3)$$

where $A = 1.308 \times 10^7$ atm, $\nu = -3753.56^\circ K$, and θ is temperature. The effect of the ammonia saturation on the temperatures in the adiabatic region are computed as first given by Lasker (1963) and later by Trafton (1965, 1967). The difference in the temperatures at a constant pressure level between the wet and dry adiabat near the level where saturation begins is small and has little effect on the detected intensity.

For the models considered, the molar fraction of H_2 ranges from 100% to 50%. A value of 80% is used as an initial model, because it is close to the average value used in models with a solar-like abundance of elements, near 86% (Lewis, 1969; Weidenschilling and Lewis, 1973) and the center of the range determined by the inversion of the 17 - 40 micron spectrum obtained by Houck et al. (1974) of 60 to 90%. The average determination of the mixing ratios of NH_3 and CH_4 in chemical equilibrium models with a solar-like abundance of the elements are about 1.5×10^{-4} and 6.2×10^{-4}, respectively. These values are close to those obtained from relative abundances determined from spectroscopic data, assuming equal path-lengths for absorption by the different constituents (summarized in Section 2.11 of Newburn and Gulkis, 1972) of $3.0 - 0.8 \times 10^{-4}$ for NH_3 and $10.0 - 3.0 \times 10^{-4}$ for CH_4. In addition, the ammonia mixing ratio is close to that which Gulkis et al. (1973) find consistent with the microwave spectrum.

C. Calculation of Emergent Intensity

The models used in the calculations presented here are purposely simple. They involve only gaseous absorption and, in some cases, complete obscuration by a thick cloud layer. The radiative transfer equations given here follow the format given in Wark and Fleming (1966), except that height, z, has been substituted for the logarithm of pressure as an independent variable.

The monochromatic intensity emerging from a non-scattering atmosphere with temperature given by $\theta(z)$, with a uniform opaque cloud whose top is at height z_0, is given by:

$$I_\lambda = B_\lambda[\theta(z_0)] \cdot T(\lambda,z,\mu) + \int_{z_0}^{+\infty} B_\lambda [\theta(z)] \frac{\partial T}{\partial z}(\lambda,z,\mu)\, dz/\mu \qquad (4)$$

where $B_\lambda[\theta(z_0)]$ is the Planck function at temperature θ, evaluated at wavelength λ and where $T(\lambda_1 z_1 \mu)$ is the transmission between height z and clear space ($z \to +\infty$) at emission angle cosine μ. For a semi-infinite cloud-free atmosphere, the first term approaches zero.

The intensity observed by each channel is the convolution of the monochromatic intensity with the channel sensitivity function. Thus, for a channel with sensitivity described by $f(\lambda)$, we have:

$$I = \int_{-\infty}^{+\infty} f(\lambda)\, I_\lambda\, d\lambda \approx \int_{\Delta\lambda} f(\lambda)\, I_\lambda\, d\lambda \qquad (5)$$

where $\Delta\lambda$ is the range over which $f(\lambda)$ is significantly greater than zero. Further simplification of equations (4) and (5) is possible only if B_λ may be reasonably approximated by a constant value over the $\Delta\lambda$ range. This assumption is not made in the calculations presented here.

The calculations of the transmission at each level of the model are based on the assumption that H_2 and NH_3 are the only constituents which are optically active in the wavelength of interest for each channel.

CH_4 is an important opacity source in the 8 micron region, due to its ν_4 vibrational fundamental, but this does not affect the 20 micron channel. NH_3 possesses a rotational band in the 100 micron (100 cm^{-1}) region which is wide enough to affect the radiation detected by the 40 micron channel. The vibrational-rotational bands of NH_3 near 10 microns were neglected because preliminary calculations showed little effect on the flux detected by the 20 micron channel. The remainder of the opacity is provided by the collisionally-induced dipole of H_2.

The reduction in the transmission provided by ammonia is computed by using a random-band technique introduced by Goody (1952), using line width and strength parameters estimated by Gille and Lee (1969) for use in Jovian atmospheric models. The NH_3 rotational band parameters given by Gille and Lee are based on the measurements of Dowling (1968) and are more comprehensive than those used in Trafton's models (1965, 1967, 1973a). The equivalent homogeneous path-lengths, pressures, and temperatures for the non-homogeneous conditions of the models are determined by an absorber-weighted approximation suggested by Taylor (1972) for use in his calculations of the effect on the transmission provided by the CH_4 opacity near 8 microns. Preliminary testing for the NH_3 rotational line parameters has shown that this algorithm gives results in agreement with those of the Curtis-Godson method (Goody, 1963) without the necessity of making new estimations at each wavelength. The plane-parallel approximation is used: the absorber-weighted path-length for rays emerging away from the local normal is simply increased over that for normally emergent radiation by a factor of $1/\mu$.

The H_2 collisionally-induced dipole opacity is calculated as in Trafton (1965, 1967, 1973b). The smooth variation in the transmission of

H_2 makes it possible to assume monochromatic calculations without prohibitively close spacing of wavelengths. Optical depth is calculated as in Trafton, and the optical depth for radiation away from the center of the disk is simply given, as above, by the optical depth of normal radiation divided by μ.

A grid of wavelengths is used in these calculations which is coincident with that used by Trafton (1966), although it has been truncated to include only the wavelengths to which each of the channels in the radiometer is sensitive. The value of the transmission to clear space above each level is computed separately for H_2 and NH_3. The effective transmission is given as the product of the two values. The intensities are calculated at each wavelength of the grid. These are convolved into the channel sensitivity by interpolating among the established intensities of the grid at one micron intervals.

The calculations have been checked by comparison with simple models where the results can be determined analytically. Comparisons with previous models of Trafton, those in publication and those prepared for this mission analysis, show no differences, except that arising from the different methods of estimating the opacity of the NH_3 rotational lines. Good agreement is also obtained in a comparison with Taylor's (1972) graph of the location of optical depth unity as a function of frequency.

D. Information Content of the Data

An approximate representation of the atmospheric region where the flux detected by each channel originates is given by figure 6. A simplified representation of the radiative transfer weighting function for each

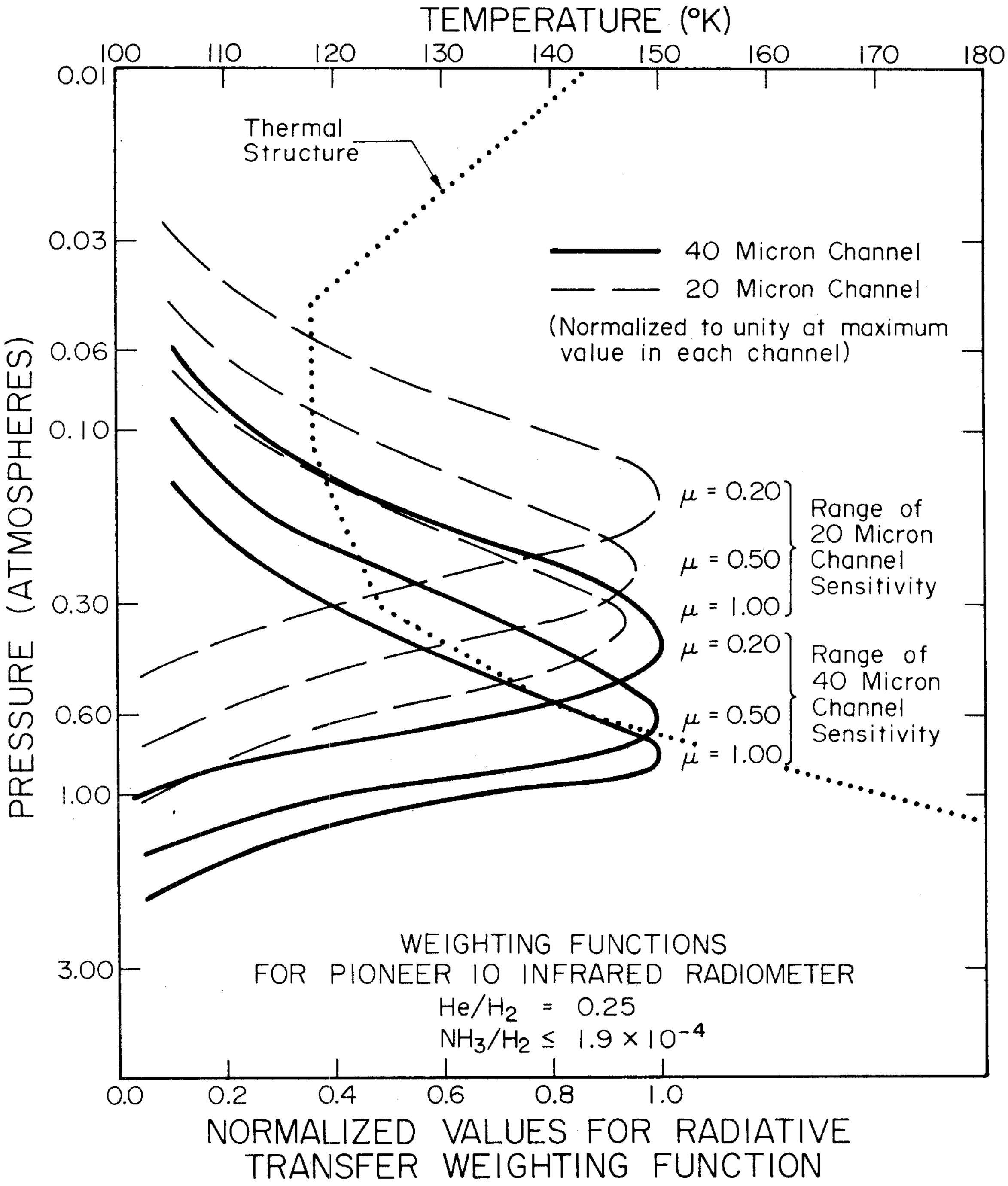

Fig. 6. - Radiative transfer weighting functions for each channel at $\mu = 1.00$, 0.50, and 0.20. $He/H_2 = 0.25$ and thermal structure is displayed although it does not greatly affect the weighting functions. A greater He abundance increases the overlap of the weighting functions for each channel and a lower abundance of He reduces the overlap.

channel is given by:

$$\overline{\text{R.T.W.F.}} = \int_{\Delta\lambda} \frac{\partial T(\lambda,\mu,z)}{\partial z} f_\lambda \, d\lambda \quad . \tag{6}$$

The weighting functions, normalized to unity at the maximum value for each channel, are displayed in fig. 6 for a sample non-scattering atmosphere with the mixing ration $He/H_2 = 0.25$. The functions displayed are calculated for $\mu = 1.00$, 0.50, and 0.20. This illustration demonstrates that at the "initial" value of $He/H_2 = 0.25$, the 40 micron channel at $\mu = 0.20$ is sensitive to approximately the same level of the atmosphere as the 20 micron channel at $\mu = 1.00$, providing some overlap in the regions to which each channel is sensitive. The range in μ displayed in the figure covers about 98% of the apparent disk radius.

Adopting the criterion that data from different channels or different parts of the disk are independent of each other only if their weighting functions intersect each other near or below one half the peak value, it is apparent that only the $\mu = 1.00$ and 0.20 samples in each channel are independent. Furthermore, the overlap of the weighting functions for the 40 micron channel at the limb ($\mu = 0.20$) and for the 20 micron channel at the disk center ($\mu = 1.00$) reduces the amount of independent samples of different atmospheric levels to three; for the example in fig. 6, these are centered roughly at pressure levels of 0.67, 0.30 and 0.13 atmospheres. The result of attempts to use a spacing which is too close may often be a derived structure which contains artificial oscillations (Conrath and Revah, 1972).

Among the models tested, the pressures associated with each of these three samples changes significantly in a clear atmosphere only with a change in the molar ratio He/H_2 and is rather independent of the temperature structure of the model.

E. Technique of Inverting the Data

Formal algorithms for deriving a representation of the mean vertical thermal structure which best fits infrared data have been devised by Wark and Fleming (1966), Chahine (1968), Smith (1970), and also by Encrenaz and Gautier (1973) with respect to this section of the Jovian spectrum. Each of these methods uses a "relaxation method", i.e. a method of successive approximations to converge on a solution; a procedure similar to these has been adopted to invert the data presented here. One may assume that the flux observed in a particular channel at a given position on the disk originates from a single level of the atmosphere. For example, intensity observed at the disk center in the 40 micron channel is assumed to be correlated only with the temperature at 0.67 atm in fig. 6. To the extent that this is only an approximation, the temperature adjustments must be iterated, with results of the model converging on a best fit to all available data. The overlap in the region sampled by the 20 and 40 micron channels is important in that assumptions made in the model, such as the value for He/H_2, may be adjusted so as to minimize any discrepancies existing between the model results in both channels. The assumptions which result in the most consistent fit to the data are incorporated into the best fit model.

Iterations on models are halted when either (1) a given model response is within one standard deviation of the mean for all values of μ between 1.00 and 0.20 in both channels (where a standard deviation for each channel has been conservatively estimated as equivalent to 1.5°K, as described below), or (2) the change in a given model response from the last iteration is less than one standard deviation for all values of μ between 1.00 and 0.20 in both channels. For the latter case, it is always clear that there is an inconsistency between the directions in which the temperature structure must change in order to fit both the 40 micron channel data and the 20 micron channel data simultaneously. In such cases, it is assumed that the model has used an inappropriate choice of initial conditions (such as composition). Differences between the response of models which are considered consistent fits to the data are, therefore, always on the order of the one standard deviation level quoted above for the noise in the data.

IV. RESULTS

The Pioneer 10 infrared radiometer data yield information about the temperatures and cloud heights of the belts and zones near the level of the cloud tops, the fractions of hydrogen and helium present, and the radiation balance of the planet and of local regions of the planet. This section discusses the details of the derived results for a variety of initial assumptions. A comparison of these results with other models for the average vertical thermal structure will be given along with a general discussion in the next section.

A. Exceptions to Latitudinal Homogeneity

Because no point on the planet was viewed at more than one value of μ, to invert the data it was necessary to treat the planet as horizontally homogeneous within bands of constant latitude, a point first made in the last section. For the STrZ, data for the east limb is used near $\mu = 0.75$ to avoid the systematic effect of the GRS in reducing the observed intensity. Near $\mu = 0.85$, the west limb intensity of the SEB is less than the east limb, an effect especially noticeable in the 40 micron channel data. An image of the planet in the 5 micron region obtained by Westphal and Terrile (1973) a few hours before the spacecraft encounter (when the aspect of the planet was approximately the same from the earth as later viewed by the spacecraft) is helpful in understanding this effect. At 5 microns, the eastern half of the SEB appears bright and contiguous, whereas the western half shows reduced intensity as well as a narrow dark strip in the center. These details are apparently unresolved by the spacecraft radiometer. The western limb has therefore been weighted more heavily in the fitting procedure, as it provides a more adequate representation of the bright intensity which is characteristic of the SEB at the resolution of the spacecraft radiometer.

B. Overlying Thermal Structure

In the initial model, we assume $He/H_2 = 0.25$, an adiabat below the 40 micron $\mu = 1.00$ sounding level (0.75 atm), and an isotherm above the 20 micron $\mu = 0.20$ sounding level (0.16 atm).

The isothermal assumption of this model is not, however, consistent with the Jovian spectrum in the 8 micron region. The spectra of Gillett, Low and Stein (1969) as well as more recent observations by Gillett (1973) exhibit a bright feature just below 8 microns. A simple interpretation of this feature is that it is due to emission in a region of increased opacity produced by the 7.7 micron CH_4 band, and that the emission originates in an atmospheric level which is thermally inverted. This interpretation is substantiated by center-to-limb brightening. A preliminary analysis of the 8-14 micron spectra, as well as the center-to-limb observations, has been undertaken with the purpose of determining a thermal structure most consistent with the data. A thermal structure, T(z), consistent with the 8-14 micron data has been used in all subsequent models presented here. It is found that results do not depend highly on the details of this overlying structure; in fact, a substitution of the thermal inversion in the crude engineering model by Divine (1971) makes no perceptible difference in results.

On the other hand, the lack of limb brightening in the 20 micron channel can be used to define a minimum thickness of the isothermal region between the 0.14 atm level and the onset of the thermal inversion. When this thickness is minimized in the model, the temperature minimum value must also be made as small as possible in order to fit the data. While a constraint minimizing this thickness is somewhat arbitrary, it facilitates a fit to the center-to-limb scan of Orton and Gillett (1974) at 8.15 microns, which shows darkening close to the disk center with brightening at the limbs. It can be fit by placing the inversion quite close to the region with a non-negative lapse rate. In addition, Ridgway (1974) has reported brightness temperature values in his very high resolution spectral observations which are more than 10 degrees below the value of the temperature minimum in the model without the inversion. A model in which the tropopause temperature is as low as possible may be useful in fitting this spectral observation. The location of the inversion region in pressure in the 8-14 micron spectrum model may be adjusted by variations in the molar fraction of methane, which dominates the opacity at wavelengths where radiation originates from this region.

C. The South Equatorial Belt

The derived thermal structure for the SEB data with the preceeding assumptions is identified in fig. 7A, and comparison with the data is shown in figs. 7B (40 micron channel data) and 7C (20 micron channel data).

The result of including this inverted region in the model with the stated constraint is also shown in figs. 7A-7C. The fit to the data is equally as good as the model with the overlying isothermal region. The difference in the temperature minimum values for both models is 5°K. Inversion models which rise even more steeply may be modeled, but the length of the isothermal segment must increase significantly in such cases.

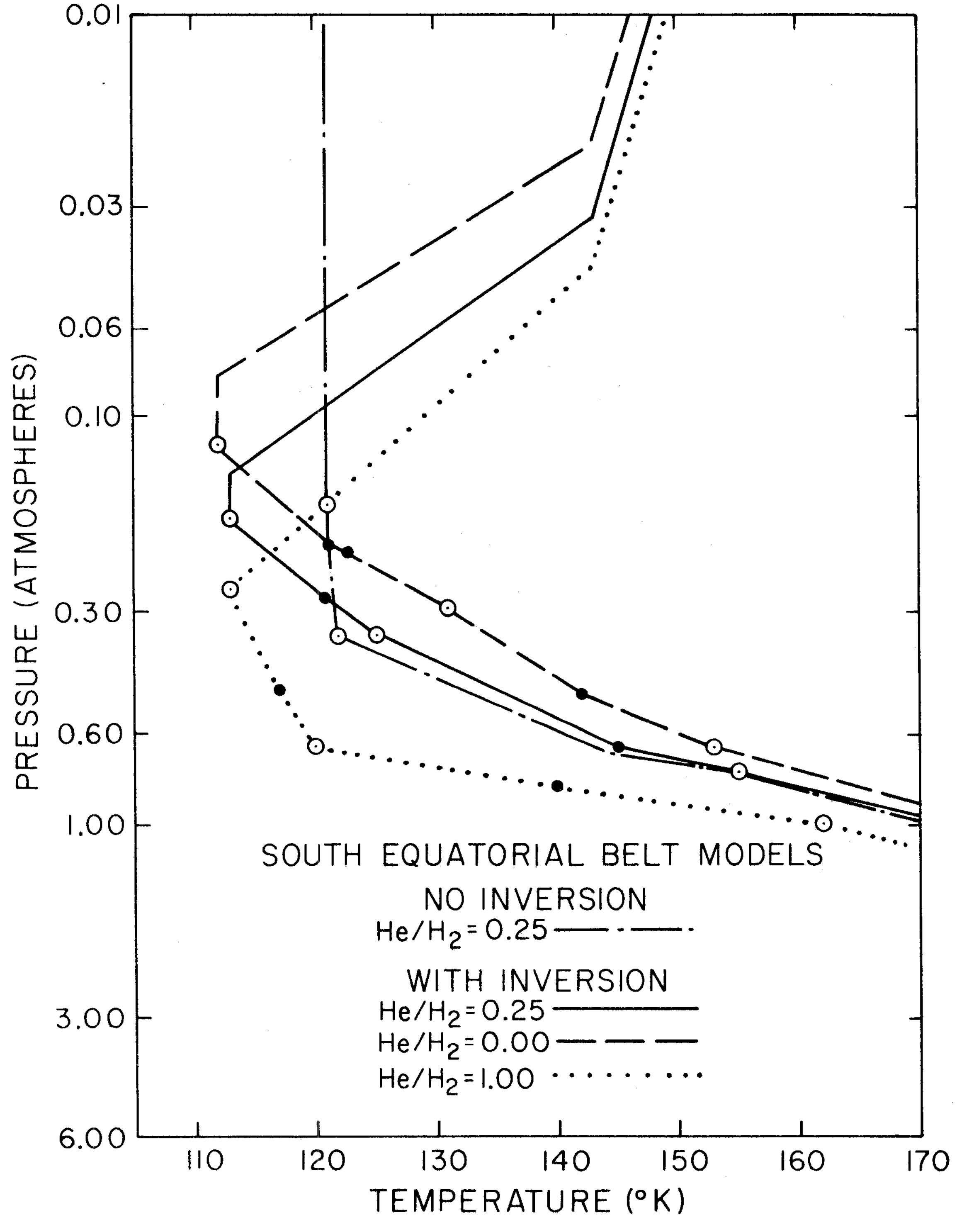

Fig. 7A. -Derived models for South Equatorial Belt. No scattering is assumed. Open circles show location of unit optical depth in each channel for $\mu=1.00$ and $\mu=0.20$. (Unit optical depth for 40 micron channel at $\mu=0.20$ and 20 micron channel at $\mu=1.00$ approximately coincident near 0.30 atm pressure.) Filled circles show unit optical depth for each channel at $\mu=0.50$.

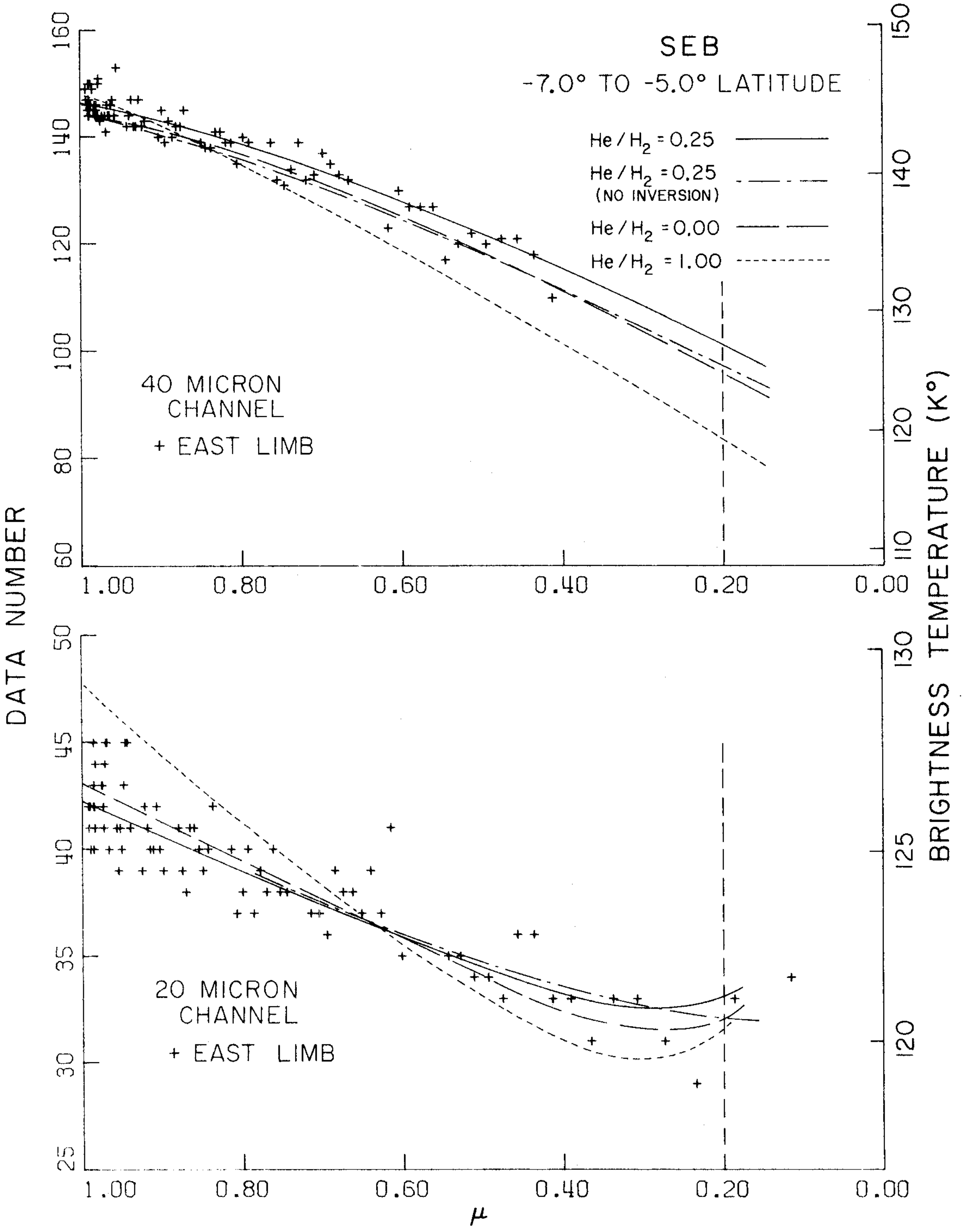

Fig. 7B. (top) 7C. (bottom) -Model fit to South Equatorial Belt data. Models are those shown in fig. 7A. West limb data not considered, as explained in text.

For the He/H_2 = 0.25 model with the inverted thermal structure best fitting the 8-14 micron data, the cold isothermal segment is about 8 km long. The best fit model results using 0% and 50% He mixtures are also displayed in figs. 7A-7C. The temperature minimum in these thermally inverted models is 112-113°K. For all models following, we shall test the model fit to the data with the He/H_2 ratio set to 0.00, 0.25, and 1.00. In the text following, these will be referred to as the "low", "nominal", and "high" helium mixing ratio models, respectively.

The figures show that the nominal He abundance models do very well in fitting the data. On the other hand, the high He abundance models display a severe discrepancy between the 40 micron channel data at μ = 1.00. Both sample from approximately the same atmospheric level, but the 40 micron results are below the data and the 20 micron results near μ = 1.00 are higher than required to provide a good fit. For the low He abundance case, the fit is not quite as good as that provided by the nominal He abundance model, being marginally higher than the data at μ = 0.20 in the 40 micron channel, but providing a good fit everywhere else. The thermal structure providing the best fit in the nominal abundance case shows consistency with the adiabatic lapse rate for this composition. The high abundance model best fit is somewhat superadiabatic and the low He abundance model is somewhat subadiabatic in the region characterized by a positive lapse rate. With respect to the best fit models to the SEB data, then, the high helium abundance model is effectively ruled out, and the initial assumed composition provides a marginally more consistent fit to the data than the pure hydrogen case.

D. Uncertainty in Derived Thermal Structure

To demonstrate the sensitivety of the best fit to perturbations in the temperature dependence on the pressure, figs. 8A and 8B show the result of perturbing the initial composition model best fit to the SEB data by (1) decreasing the pressure at each level of the best fit model by 10%, and (2) decreasing the temperature at each level of the best fit model by 2 degrees. The effect of the pressure change is quite dramatic in the 40 micron channel results where the lapse rate is relatively high, and it is comparable to the 3 degree depression in the thermal structure. In the 20 micron channel results, however, the effect of the pressure modification is not nearly so great as the temperature decrease, due to the weaker temperature variation with pressure near the temperature minimum. The closer proximity of the inversion region near $\mu = 0.20$ in the 20 micron channel is noticeable as a limb-brightening effect, but such an effect might be disguised in the data noise. The temperature perturbation of the model is significant in both channels, and the sensitivity to pressure is as great only when a comparable change in the temperature is implied by the pressure change.

More than 68% of the data for the SEB are enclosed in perturbations of the model by $\pm 1.5^{\circ}$K from the best fit thermal profile. This may be taken as an estimate of the one standard deviation (1 σ) noise implicit in the data. This serves as a conservative estimate of uncertainty of 1.5 degrees is the most appropriate.

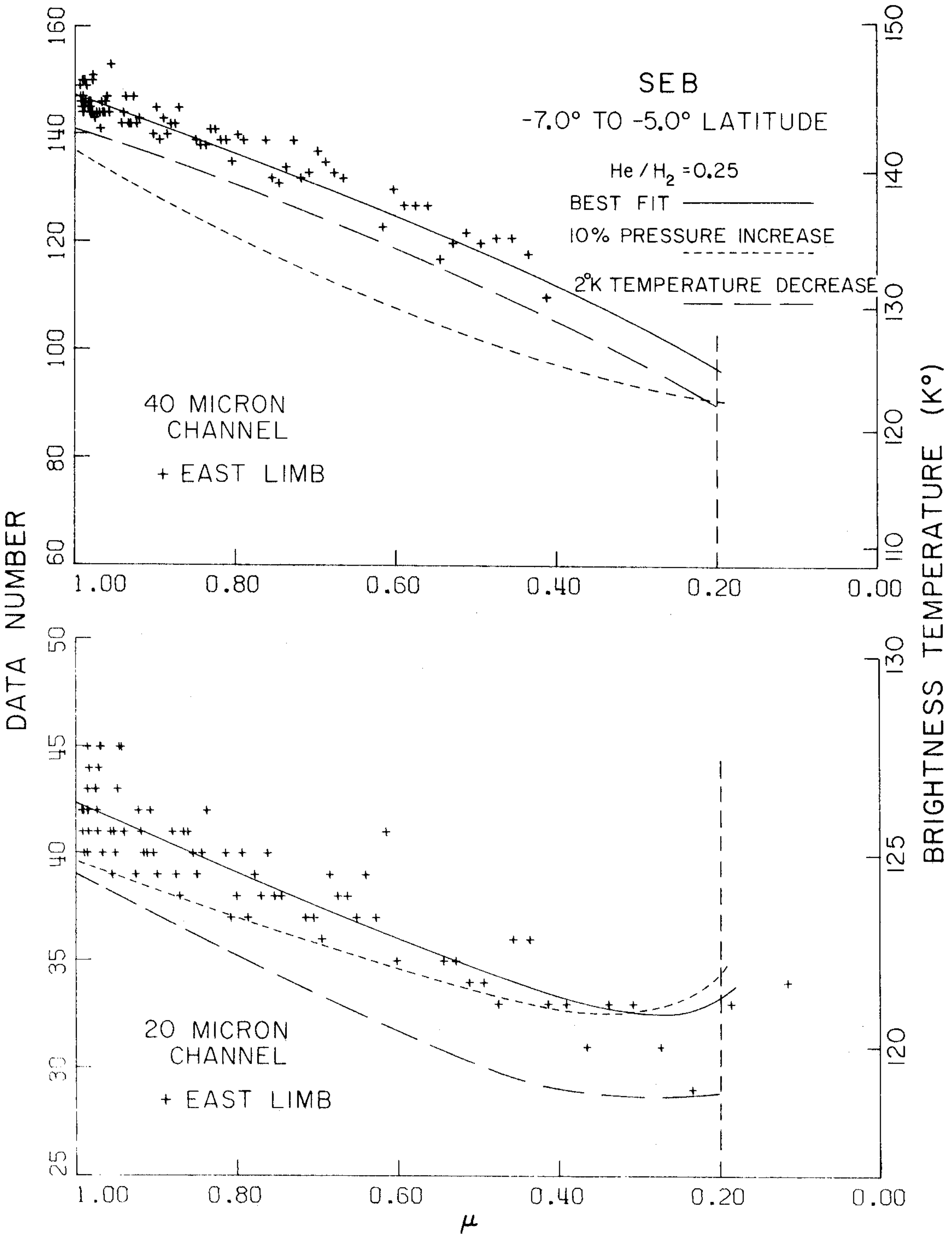

Figs. 8A.(top) 8B.(bottom) -Result of perturbing best fit model to SEB data in pressure and temperature.

E. The South Tropical Zone

The best fit clear atmosphere models to the STrZ data (latitudes -16.0 to -14.0 degrees) for the east limb are shown in fig. 9A. A comparison of model results with the data for the 40 and 20 micron channels (fig. 9B and 9C, respectively) show a good fit to data with both low and nominal He abundance models. In the high He abundance case, there is again a discrepancy between the 40 micron channel at $\mu = 0.20$, where the model is not as bright as the data, and in the 20 micron channel at disk center, where the model is brighter than the data. The pure H_2 model is somewhat brighter than the 20% helium case at the limb in the 40 micron channel, but this difference does not exceed the noise of the data. The derived thermal structures are all subadiabatic above the region where the adiabatic temperature structure has been assumed. Again, the high helium abundance model is rejected as inconsistent with the data, whereas the nominal and low helium abundance models cannot be ruled out on this basis.

F. South Tropical Zone with Clouds

An alternative model for the STrZ observed intensities provides a minimum deviation from the thermal profile of the belt region by means of a layer of obscuring cloud. The following models for the STrZ have used the limiting case of an obscuring cloud: a laterally homogeneous and optically thick cloud top which obscures all radiation below it and behaves like a black body emitter at the ambient temperature. The initial step in the fitting procedure places the cloud top in the derived thermal profile for the SEB data at a position which best fits the STrZ data.

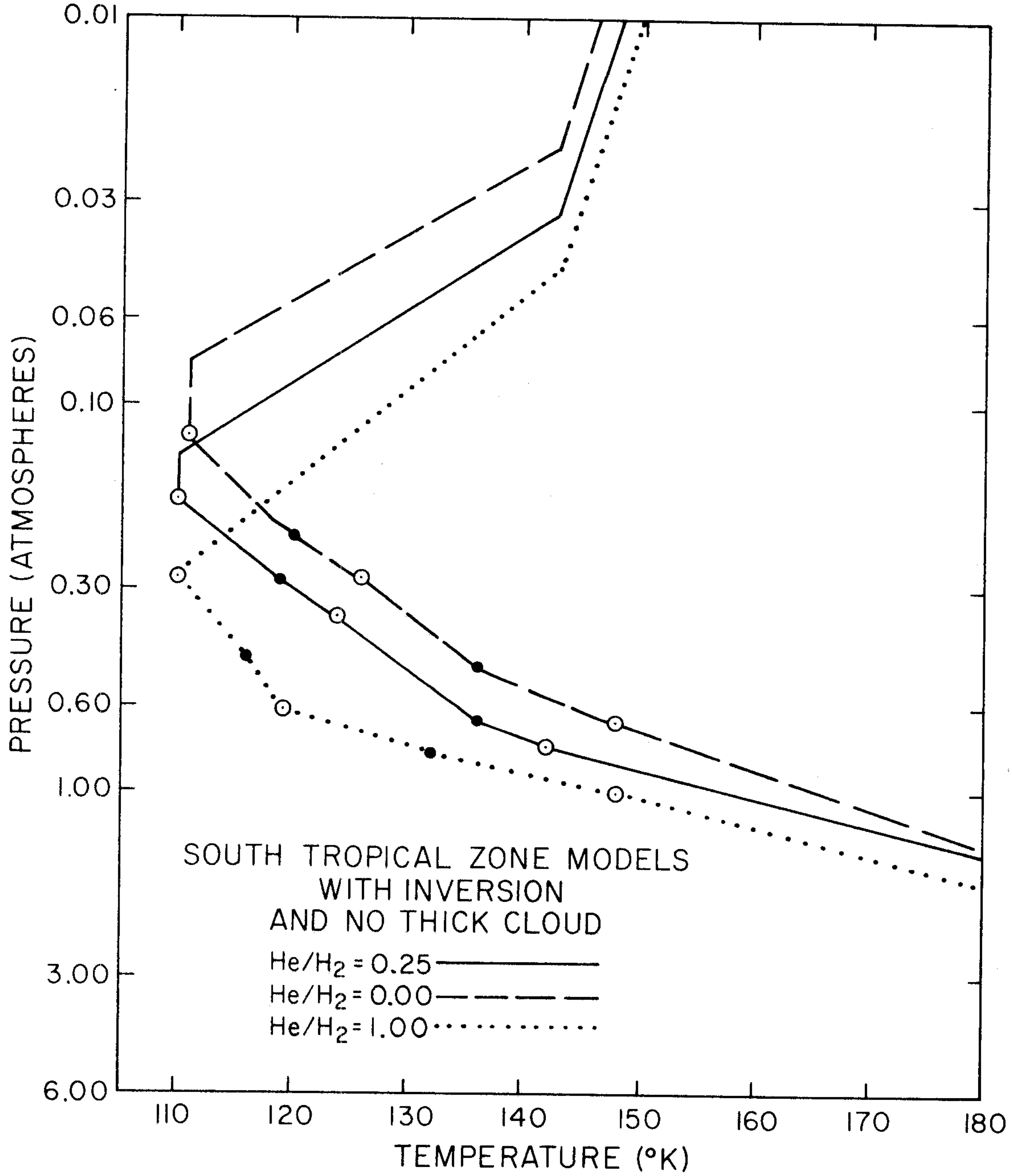

Fig. 9A. -Derived models for South Tropical Zone (northern part). No scattering is assumed. Symbols as in fig. 7A.

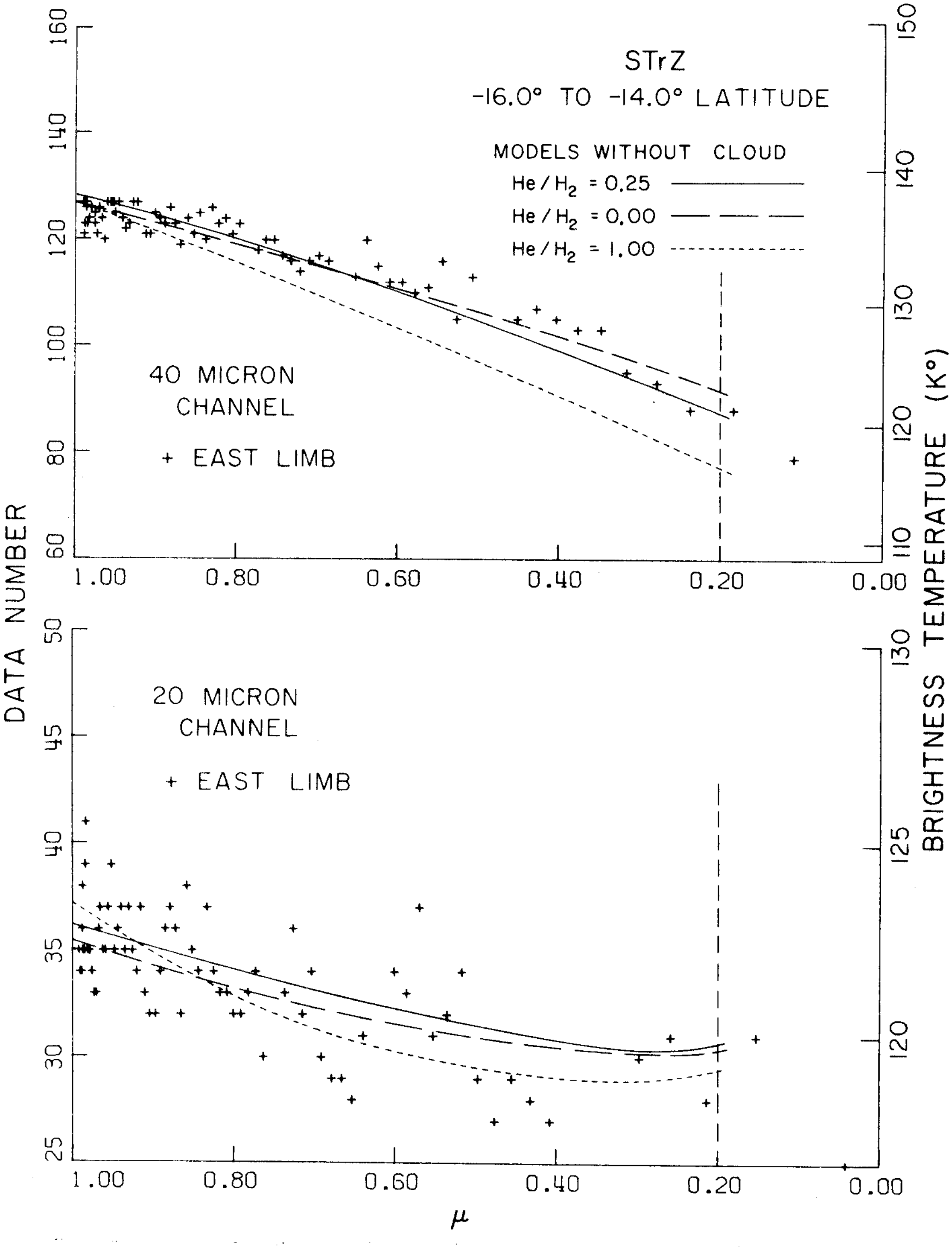

Figs. 9B.(top) 9C.(bottom) -Fit to South Tropical Zone (northern part) data. Models are shown in fig. 9A. West limb data not considered, as explained in text.

The fit to the data is then improved by using the inversion procedure for a clear atmosphere, and the cloud top position is once again checked in the revised thermal structure.

The thermal structures and comparison with STrZ data derived using this procedure are shown in Figs. 10A-10C. Once again, it is apparent that the high He abundance case is inconsistent with the data in both channels. Both the low and nominal He abundance models show a consistent fit to the data: the low He abundance model is marginally a poor fit to the 40 micron channel data at $\mu = 0.20$ in this case, as it is in the best fit model for the SEB data.

The derived thermal profiles for the nominal He case from SEB and STrZ data (both "clear" and "cloudy" models) are compared in fig. 11 . Both STrZ models display a 2 to 3 degree lower minimum temperature than the SEB model, and all models have identical values for the length of the short isotherm at the temperature minimum (18 km). Near the 0.75 atm level the temperature difference between the "clear" STrZ model and either the SEB model or the "cloudy" STrZ model is 12-13 degrees. The temperatures deeper in the model are assumed to have this difference, as well, since adiabatic extrapolations inward are used in each.

G. The North Equatorial Belt and the Great Red Spot

Models have also been generated in order to fit data from the NEB (+9 to +11° latitude) region, for the STrZ at the approximate latitude of the GRS (-18.5 to -16.5°) along the east limb, and the limited data for the GRS itself. In all these models the nominal He abundance has been used, as it has provided a consistent fit to all the data. The NEB model comparison with data is shown in figs. 12A and 12B. The NEB thermal

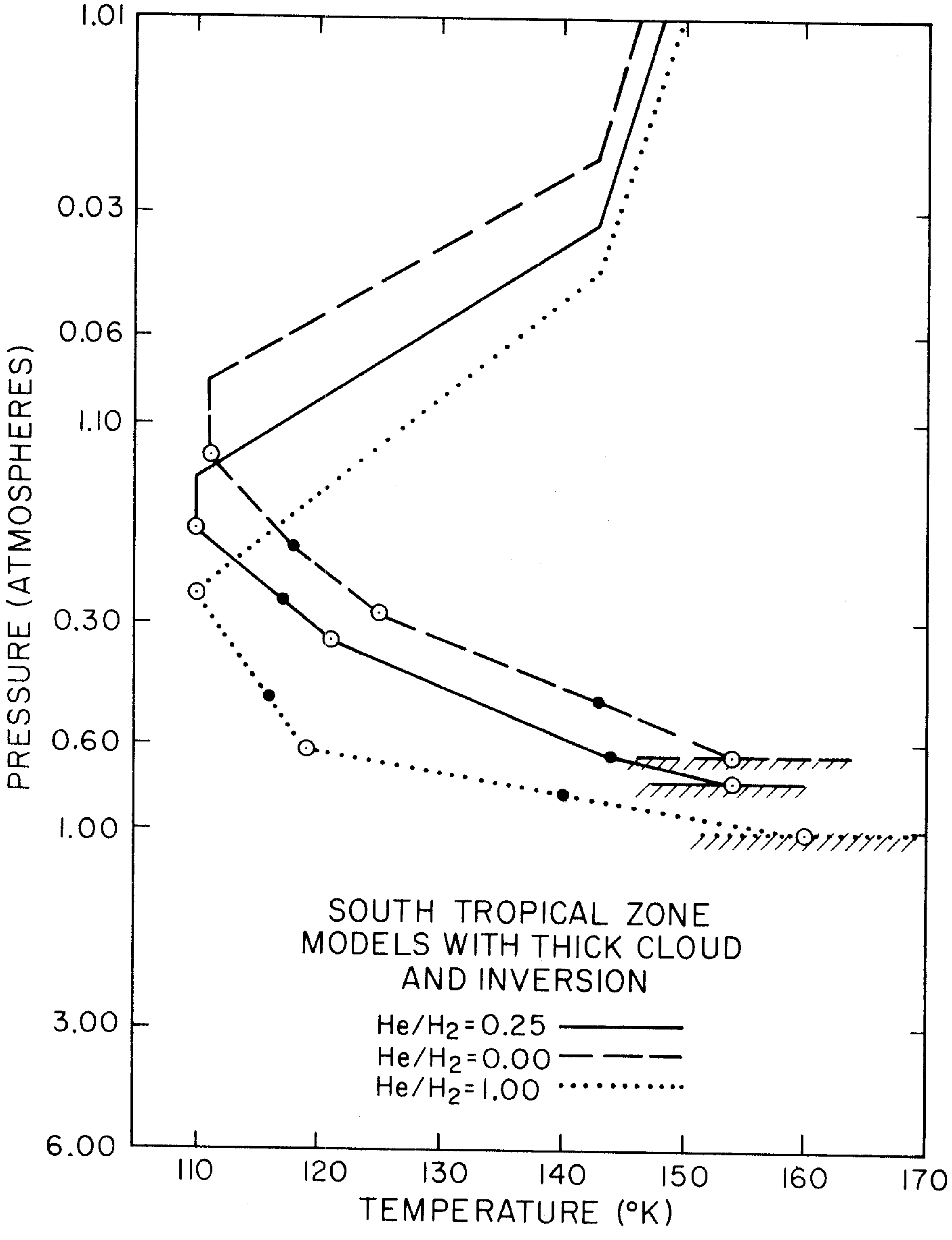

Fig. 10A. -Derived models for South Tropical Zone (northern part) for presence of thick cloud and minimum deviation from SEB thermal structure. Hatched areas represent location of thick cloud top.

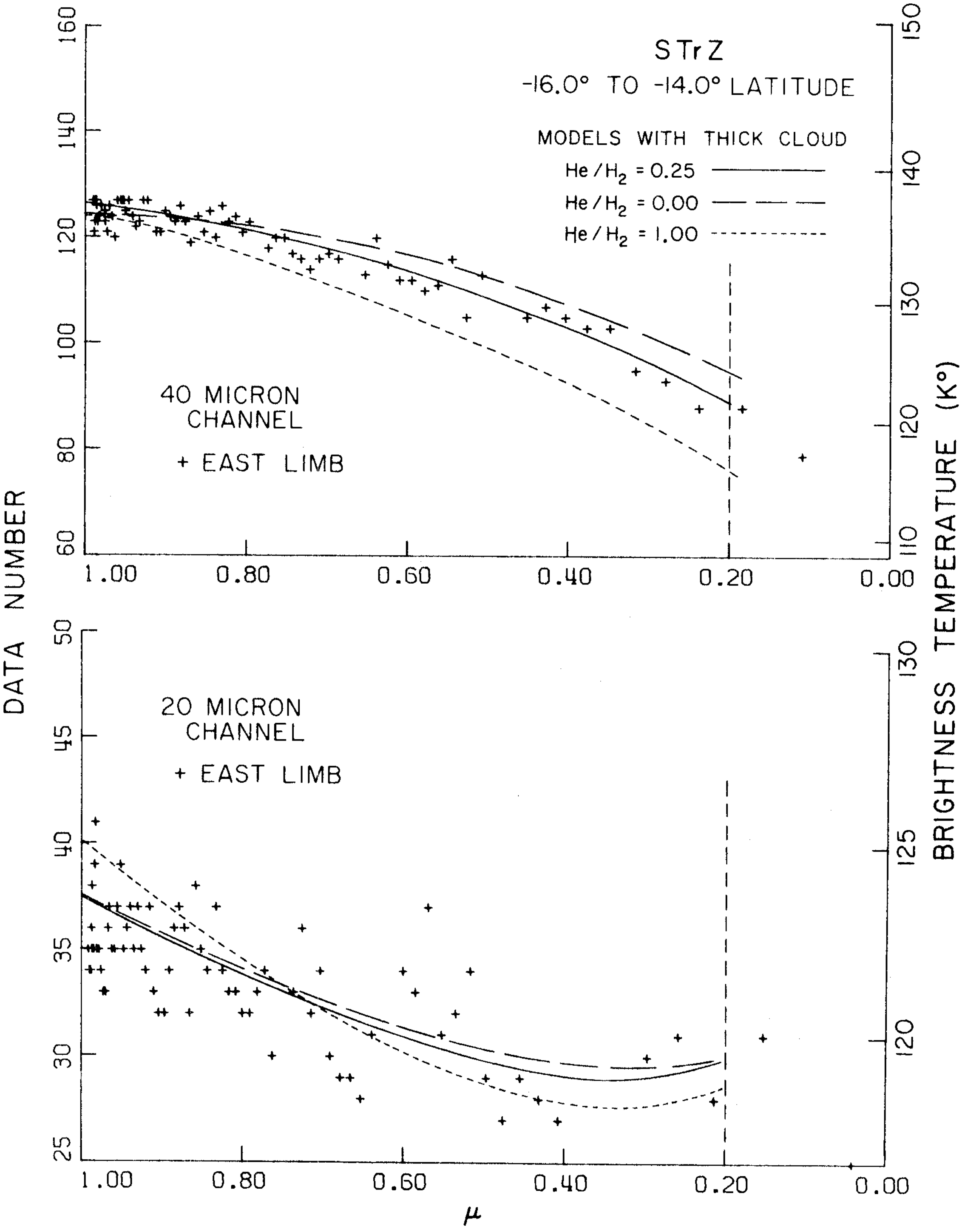

Figs. 10B.(top) 10C.(bottom) -Fit to South Tropical Zone (northern part) data for models with thick cloud. Models shown in fig. 10A. West limb data not considered, as explained in text.

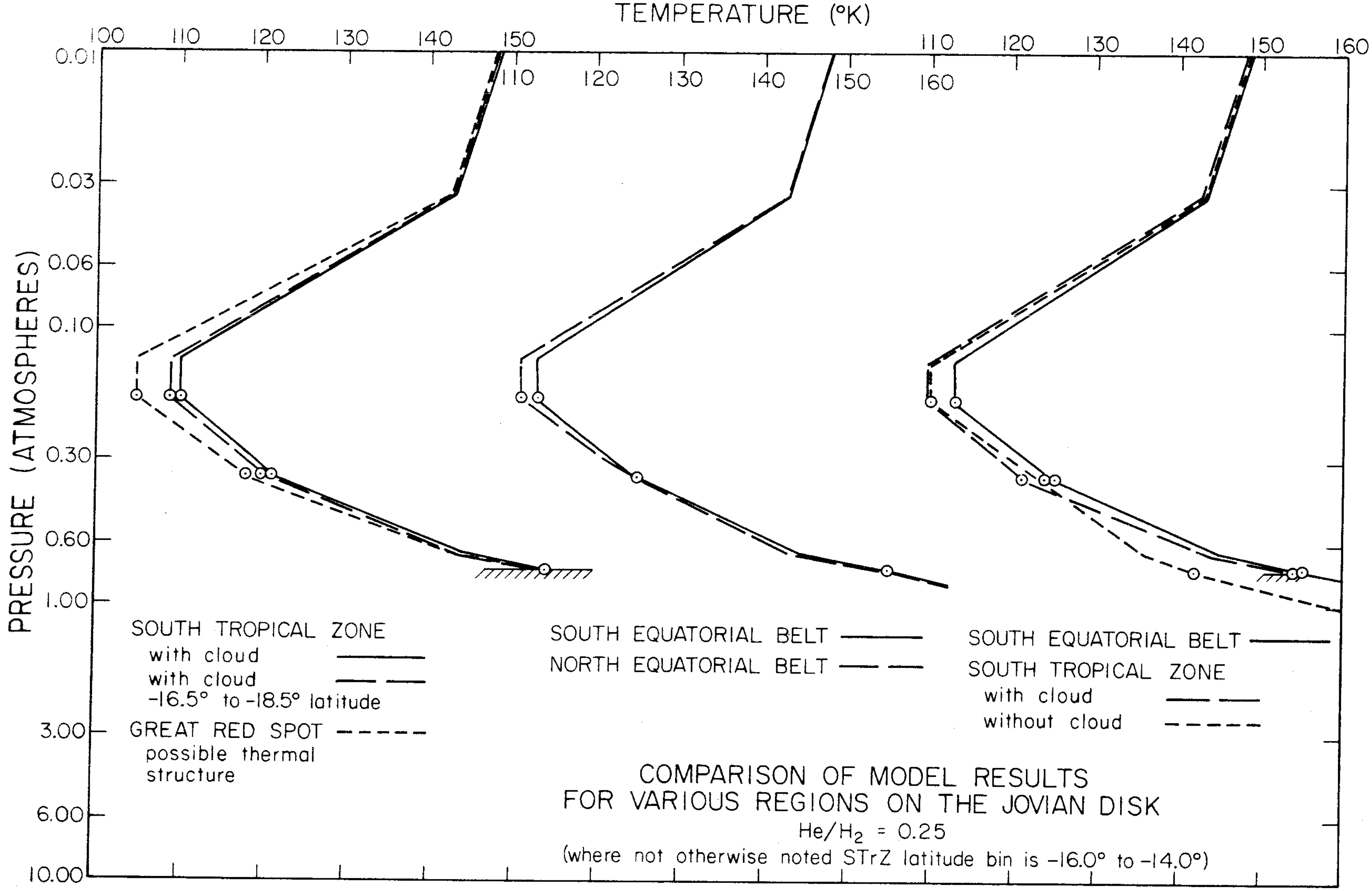

Fig. 11. -Comparison of derived thermal structures for various regions of planet. Circles have same significance as in fig. 7A.

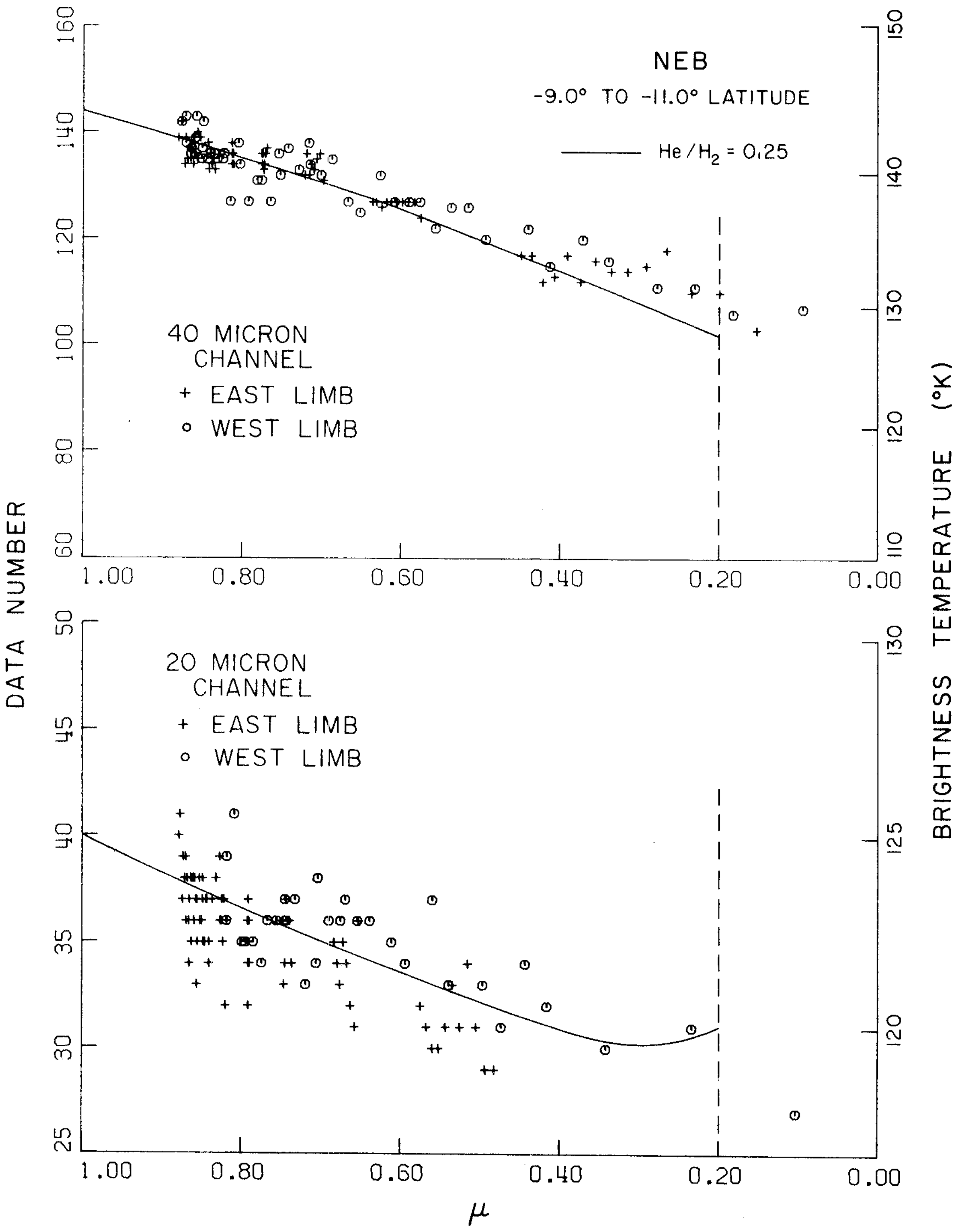

Figs. 12A. (top) 12B. (bottom) -Model fit to North Equatorial Belt data. Data from both limbs is shown. Model is shown in center of fig. 11. Deviation of model from 40 micron channel data near limb is discussed in text.

profile (fig. 11) is negligibly different from the SEB near 0.75 atm, and falls to 111°K at the temperature minimum. The fit to the 40 micron channel data at the limb is not very good, and is not improved by changing the chemical composition. The data at this point may, however, be subject to the same systematic error which causes a "ringing" on the northern edge of the planet where the radiometer intercepted the limb, i.e. an artificial bright crescent, which can be seen in enhanced version of the planetary image particularly for the 40 micron channel. This effect is not observed as strongly in the 20 micron channel data.

The fit to STrZ data for latitudes -18.5 to -16.5 degrees and comparison with the model shown previously for a more northern latitude bin are displayed in fig. 11 .. Comparison with data is shown in figs. 13A and 13B. The "cloudy" model has been used in the fit. It is apparent that the derived profiles for the two latitude regions are no more than 2 degrees apart at any given pressure level. As a whole, the data and derived thermal profiles for the eastern half of the zone are quite uniform.

Data for the Great Red Spot cannot be fit simply by varying the height of the obscuring cloud in the STrZ models. For example, the 40 micron intensity difference between the east and west limbs at -18.5 to -16.5° latitude and $\mu \approx 0.75$ can be modeled by raising the height of the cloud top some 2 km with no change in the thermal structure (fig. 11). However, a fit to the 20 micron channel data in the vicinity of the Red Spot can be obtained only by changing the cloud top level upward some 16 km, but the consequence is a drastic inconsistency in the 40 micron

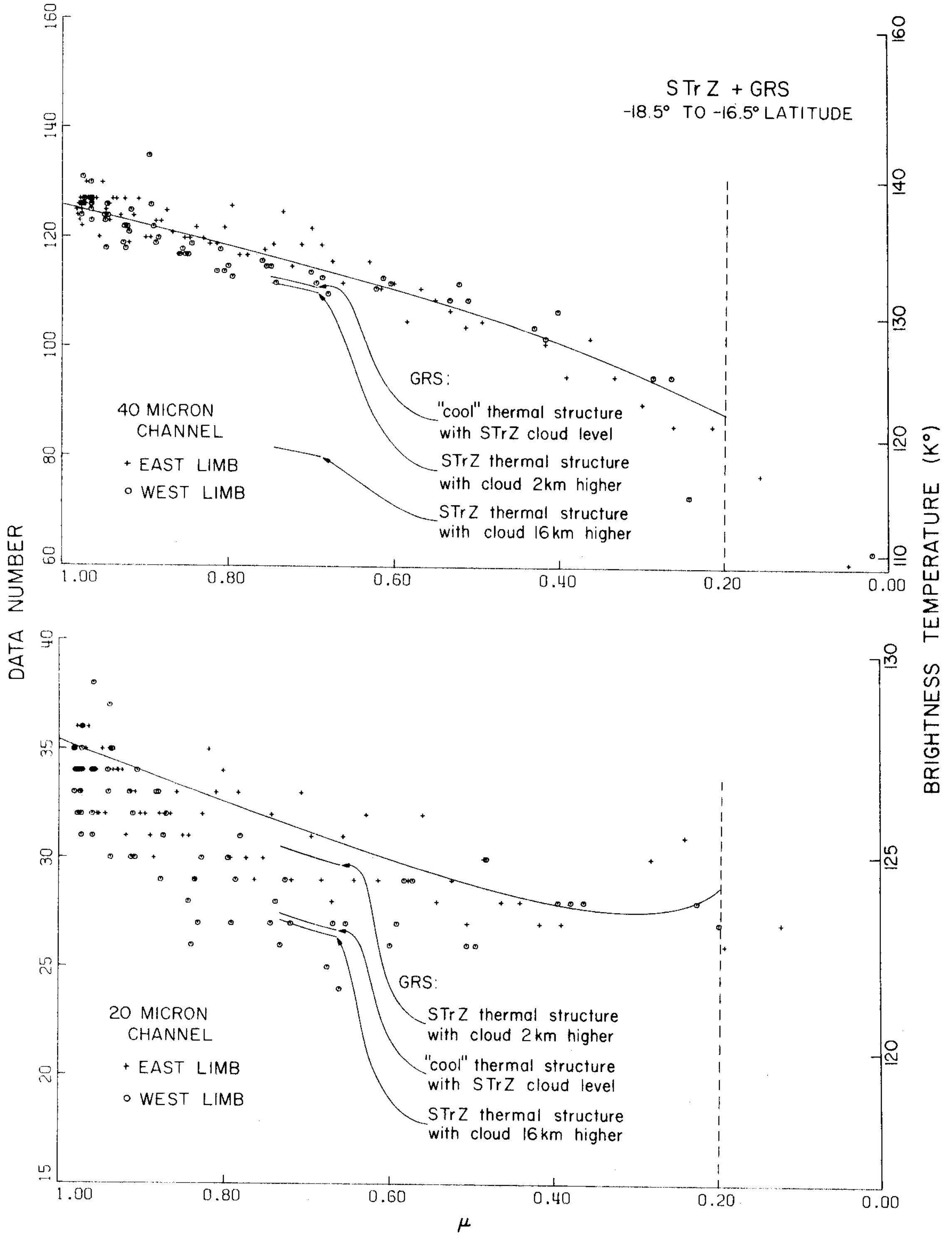

Figs. 13A.(top) 13B.(bottom) -Fit to South Tropical Zone (southern part) data for models with thick cloud, and fit of models to Great Red Spot data. Models shown on left side of fig. 11. Great Red Spot is seen as depression in west limb data relative to east limb data near μ=0.70 .

channel data. Thus, to model the data, we require a mechanism which produces a large variation between the adjacent GRS and STrZ intensities in the 20 micron channel and rather little in the 40 micron channel.

A possible candidate which is successful in this respect is a model similar to the STrZ "cloudy" model. Instead of changing the cloud height, however, a perturbation in the thermal structure may be affected. The perturbation from STrZ structure takes a linear form in height, with no variation from the STrZ structure at the cloud top and a maximum variation at the tropopause. The maximum variation is characterized by a free parameter. This model fits the GRS data quite well (figs. 13A and 13B), and results in a tropopause temperature about 5 degrees cooler than the temperature of the STrZ "cloudy" model.

The non-uniqueness of the GRS model should be emphasized, however. Other variations in the thermal structure may fit as well, either with or without changes in the cloud top level. Furthermore, we cannot rule out more complex models, such as a haze which is a more efficient scatterer near 20 microns than 40 microns. More than these two data will be necessary to reduce the number of simple models which are consistent with the present data.

H. Summary of Results

In summary, the results presented in this section demonstrate the following. Foremost, it is possible to fit the data with simple, non-scattering models. The compositions tested show that the case in which $He/H_2 = 1.00$ is inconsistent with the data. On the other hand, the assumptions of either $He/H_2 = 0.00$ or 0.25 are consistent, the latter marginally more so than the former. Perturbation of the best fit model temperatures which enclose 68% of the data serve to provide a conservative estimate (1.5°K) of the one standard deviation level of the data noise. Both the pure H_2 and the 80% H_2 with 20% He models for the SEB are consistent with the assumption of an adiabatic structure deeper in the planet. A "clear" atmospheric model for STrZ data is somewhat subadiabatic and some 12° cooler than the adiabat in the SEB model. The STrZ data may be fit equally well, however, by a model minimizing the deviation from the SEB thermal structure with a thick cloud acting like a black body emitter at the temperature of its top. For either model of the STrZ, the value of the temperature minimum is 110°K; the SEB temperature reaches a 113°K minimum. The values of this minimum may be increased or decreased by, respectively, decreasing or increasing the temperatures in the inversion region. The values quoted above are the result of assuming a T(z) for the inversion which is consistent with the brightness of the CH_4 band near 8 microns. The thermal structure model for the NEB is much like the SEB model; the model fit to the southern part of the STrZ is also close to the structure derived for the northern part. The GRS data is not consistent with a single thick cloud in the thermal structure derived for the STrZ "cloudy" model, but a thermal structure somewhat cooler by about 5°K near the tropopause fits the limited data quite well.

V. DISCUSSION

This section discusses the results derived in the last section by (a) Intercomparison of the various models results, (b) Model implications for the planetary thermal infrared spectrum and the heat budget, and (c) Comparison of the derived temperature profiles with the results of other investigators.

A. Intercomparison of Derived Model Results

Our results of the last section indicate that the compositional assumption of 50% H_2 and 50% He does not adequately describe the data; both 0% and 20% He in an otherwise pure H_2 atmosphere do quite well, on the other hand, with marginal inconsistencies in some cases for the pure H_2 composition. The set of pure H_2 models cannot be ruled out on this basis, however, and the same is undoubtedly true of models with somewhat more than 20% He by volume. Thus, for the simple families of models considered, compositions of about 35% helium by volume or less in an otherwise pure H_2 atmosphere provide model sets consistent with the data.

The "clear" and "cloudy" models for the STrZ represent two extreme alternates: no obscuration with a maximum deviation from the SEB thermal structure, and full obscuration (below a well-defined level) with minimum deviation from the SEB thermal structure. These two models must be considered to represent the end members of a family of models which undoubtedly fit the STrZ data equally well. No method exists at present to discriminate the validity of even the extreme alternatives. The "clear" model implies a maximum variation of temperature (about 13 degrees) along isobars between adjacent SEB and STrZ regions. For this case to be consistent with the investigations of Ingersoll and Cuzzi (1969), this average temperature difference could only be tolerated for about 12 km below the visible cloud level, assuming that the flow at this atmospheric level is adequately described by the geostrophic approximation. This is entirely possible if the tops of the visible clouds are below the 0.65 to 0.75 atm level. On the other hand, the rotational velocity differences analyzed by Ingersoll and Cuzzi could be generated by temperature differences of only 1 degree, extending over 150 km which is on the order of our data noise.

The "cloudy" model is attractive, however, for a variety of reasons. First, the 5 micron intensity, which should suffer a minimum of extinction from molecular absorption by any known atmospheric constituents, is extremely different in the SEB and STrZ regions (Westphal et al. , 1974). This would be difficult to achieve only with variations in the thermal structure between these two regions. Therefore, it is likely that some form of obscuration takes place in the STrZ with respect to the SEB at some level in the atmosphere. Second, a cloud presence in the STrZ and absence in the SEB provides a mechanism by which the difference in visible albedo which defines these two regions may be easily explained. Third, the location of the best fit cloud top correlates highly (within 4 km) with the location at which NH_3 is expected to condense, assuming its abundance is close to the assumed mixing ratio of 1.5×10^{-4}. Therefore not only the cloud presence, but its approximate location could be predicated by a reasonable _a priori_ assumption about the planetary physical chemistry, in which the obscuring cloud is interpreted as a thick layer of ammonia ice particles. If the obscuring material is NH_3 ice, then its absence in the SEB must be explained by appealing to a wind structure in which a downdraft in the SEB systematically clears the region of condensing ice. This clearing mechanism must be sufficient to allow the large amount of observed 5 micron radiation to be emitted, as well.

The tropopause temperature in both "clear" and "cloudy" STrZ models is systematically lower than that derived for the SEB in all model compositions. This difference may be accounted for by differences in the effective heating of this atmospheric level, assuming it to be in radiative equilibrium. For instance, a simple "two-stream" (Eddington) approximation in which this level equilibrates with the flux emitted by the planet below predicts a temperature about 0.84 times the local effective temperature of the planet. The approximate 2 - 3°K temperature difference between the STrZ and the SEB at this level would imply a difference between the local effective temperatures of these regions of about 2 - 4 degrees. This is on the order of the differences in the local effective temperatures of the SEB and the STrZ as determined later in this report. Alternately, if particulate absorption of sunlight in the violet and ultraviolet, as suggested by Axel (1972), provides an effective heat source for this atmospheric level, the higher albedo of the zones with respect to belts (Pilcher et al.,1973; Part 1) might also be able to account for this systematic difference. If the thermal structure proposed for the GRS (fig. 11) is correct, however, then the low tropopause temperature would not correlate with the low albedo of the GRS with respect to the STrZ.

B. Spectra and Total Flux of the Models

Figures 14A and 14B show the specific intensity for SEB and STrZ models, respectively. The graphs show the equivalent intensity from a whole disk and are computed from the best fit models described earlier. Figure 14C shows the expected brightness temperature spectrum for the whole disk, combining the results shown in figs. 14A and 14B as if the whole planet behaved like a homogeneous region with 40% belts and 60% zones. The features prominent in these spectra include the ammonia pure rotational band near 100 cm^{-1} (100 microns), and two of the collisionally-induced H_2 rotational lines near 360 cm^{-1} (28 microns) and 600 cm^{-1} (17 microns).

Variations in the spectral response of the different models given as best fits to the same region are below the noise level of the data. Had the convergence criterion for the consistency of each model fit to the data been artificially made more stringent, these differences in the spectral response would vanish. It is felt that the differences in the spectral responses of the models are at least an accurate reflection of the data quality.

A whole disk spectrum of the planet from about 700 to 200 cm^{-1} has been presented by Houck et al. (1974). While these results are preliminary, correlation with the morphology of fig. 14C is good. This preliminary comparison does confirm the validity of the assumption that H_2 is the major opacity source at these wavelengths; however, a feature at 23 microns (435 cm^{-1}) is identified in the observed spectrum. The extent of the influence of this feature on the observed intensities in the 20 micron channel must await the final results of these investigators.

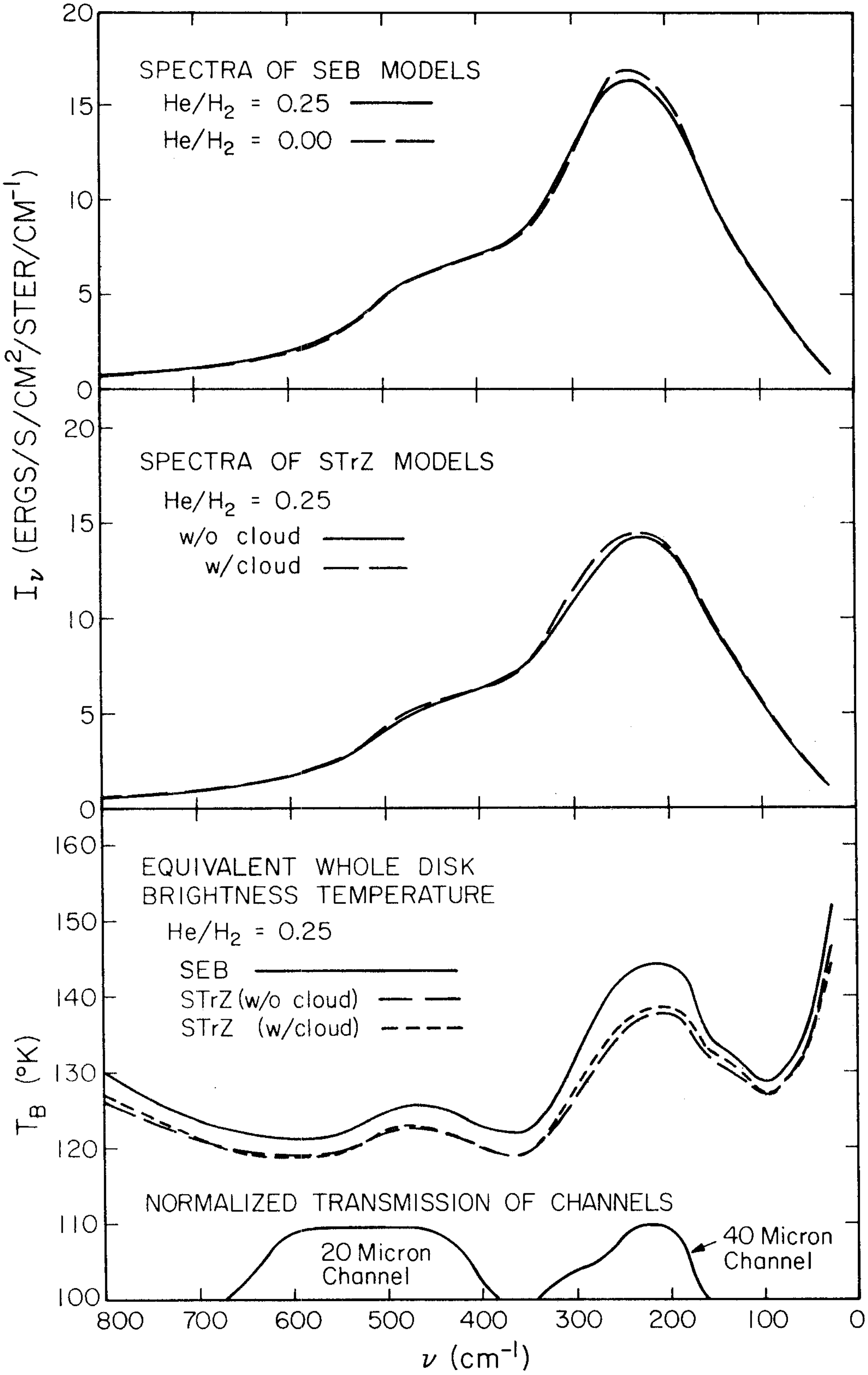

Figs. 14A.(top) 14B.(middle) 14C.(bottom) -Spectra of various models for South Equatorial Belt and South Tropical Zone. For reference, normalized transmission function of each channel is displayed at bottom of fig. 14C.

The specific intensity values, such as those displayed in figures 14A and 14B, may be used to derive the local effective brightness temperature for the SEB and STrZ regions. The contribution to the total intensity from wavelengths shorter than 12.5 microns (800 cm^{-1}) has been taken from the 8 - 14 micron spectral results mentioned above. While the contribution of this section of the spectrum amounts to only about 2% of the total computed planetary flux, and its omission would result in slightly more than a 0.5°K drop in the computed effective temperature, we have tried to avoid this systematic error. Following Westphal's (1971) meridional scans of the planet in the 8.2 and 13.5 micron region which show little contrast between belts and zones, the spectra of belts and zones at these wavelengths have been assumed to be identical. Center-to-limb structure has been derived by a model in Part 3 for this spectral region which is mostly dominated by molecular NH_3 opacity. The predicted limb-darkening is in close agreement with the scans of Wildey and Trafton (1972) in the 8 - 14 micron region.

Table 1 shows the computed effective brightness temperatures for each model, including the flux contribution from the region below 12.5 microns. These values have been derived in a manner similar to that used in generating the spectra in figs. 14A and 14B , assuming (1) azimuthal symmetry about the vertical and (2) the thermal structure given by the models. The SEB models imply an effective temperature of 128.9°K, with estimates ranging from 128.7 to 129.1°K. The STrZ models imply an effective temperature of 125.7°K with estimates ranging from 125.4 to 125.9°K. To within a ±0.3 degree maximum variation, then, these results may be considered independent of assumptions with respect to chemical composition, extent

TABLE 1

LOCAL EFFECTIVE TEMPERATURE (°K)

Region	He/H_2			
	0.00	0.25	Ave	
SEB (no inversion)		128.9	128.9 ± 0.1	
SEB	129.1	128.8		
STrZ (without cloud)	125.4	125.4	125.4 ± 0.0	125.7 ± 0.4
STrZ (with cloud)	126.2	125.9	126.1 ± 0.2	

of cloudiness, or thermal structure above the tropopause for models consistent with the data. The differences in the effective temperature values for each region are below the 1.5°K standard deviation measure derived previously and cannot, therefore, be considered significant.

If we assume that all zone regions emit similarly to the STrZ and all belts emit like the SEB, then a planet covered by 40% belts and 60% zones would have a corresponding effective temperature of about 127.0°K. This is lower than the value of 134 ±4°K measured by Aumann et al. (1969) and Armstrong et al. (1972). An increase in the belt to zone ratio would not be sufficient to satisfactorily reduce this discrepancy. We must conclude either that (1) both sets of observations cited immediately above or our results suffer from calibration errors on an order equivalent to about 7 degrees near 40 microns, or (2) there is some fundamental error in the opacity model assumed in these derivations which makes a significant change in the derived shape of the spectrum, or (3) other regions of the planet are brighter at 40 and 20 microns than the SEB or NEB appear in our observations.

The plausibility of the first two explanations is difficult to verify. Calibration errors are difficult to ascertain and are usually only fully resolved by independent observations. Higher resolution spectra could determine to what extent either calibration errors or errors in the spectral shape have been made. A simple test can be made, however, to determine the amount of flux originating from regions other than the equatorial belts and zones (explanation #3). Table 2 displays the average flux detected by each channel of the radiometer for the whole disk, expressed as an equivalent brightness temperature. The equivalent brightness

TABLE 2

EQUIVALENT BRIGHTNESS TEMPERATURE (°K)

	20 Micron Channel	40 Micron Channel
WHOLE DISK	121.3	136.2
SEB (He/H_2 = 0.00)	122.7	138.0
(He/H_2 = 0.25)	123.8	138.6
STrZ (He/H_2 = 0.00)	120.6	133.4
(without cloud) (He/H_2 = 0.25)	120.9	133.0
STrZ (He/H_2 = 0.00)	121.8	135.5
(with cloud) (He/H_2 = 0.25)	121.9	134.9

temperatures are also listed for the case in which the whole disk limb structure can be characterized by the limb structure observed at constant latitude for the SEB and STrZ. Were the planet emitting significantly more radiation in the direction of the spacecraft than the SEB or the STrZ, one would expect to see larger equivalent temperatures for the whole disk in either channel of the radiometer. The table shows that only the 20 micron channel whole disk temperature is not bracketed by the equivalent values for the SEB and STrZ. In fact, it is lower than either the SEB or STrZ values, and suggests that the polar regions are dimmer, not brighter, than the equatorial region near 20 microns. In turn, this suggests that the average temperature at the approximate level of the atmosphere sampled by the 20 micron channel is lower near the poles than the equator. It does not in any way support the argument that the flux levels seen by earth-based bolometric infrared measurements, which were taken not far from the plane in which the spacecraft observations were made, are the result of a significant increase in the brightness of regions further from the equator. The results of the infrared radiometer on board Pioneer 11 will cover areas further from the equator and may be able to determine the extent to which the poles contribute to the total thermal output of the planet.

C. Comparison with Other Models

Figures 15A and 15B display the models for the SEB and STrZ for the pure hydrogen and the 20% helium dilution models derived in the last section. The following models are also displayed: (1) the neutral atmosphere inversion of the Pioneer 10 radio occultation data (Kliore, et al., 1974), (2) the model adiabat best fitting spectral data in the microwave

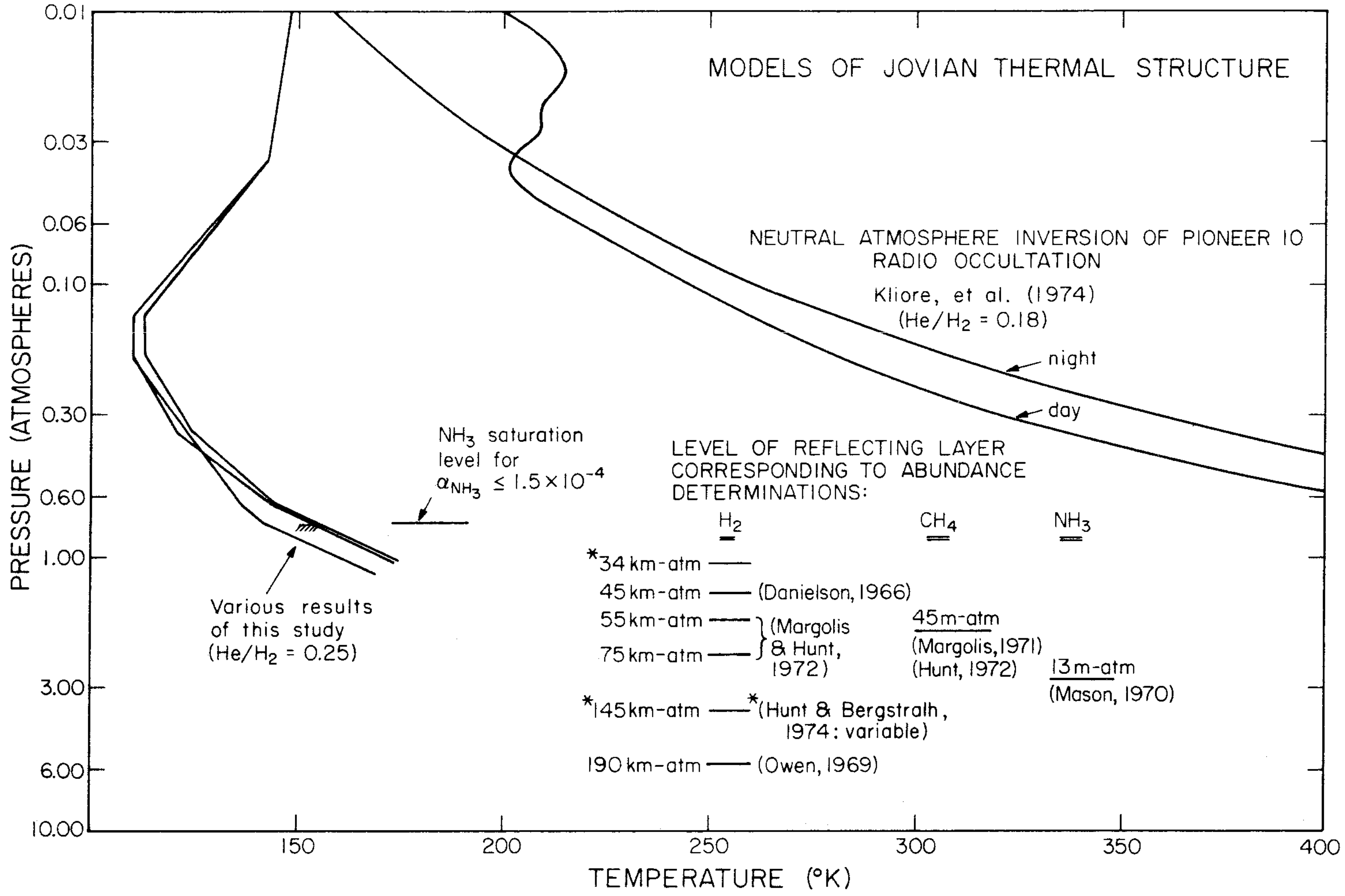

Fig. 15A. -Comparison of derived results (fig. 11, right) with alternate Pioneer 10 results. Also displayed are locations of reflecting layers defined by spectroscopic data for: $He/H_2=0.25$, $\alpha_{CH_4}=6.2\times10^{-4}$, $\alpha_{NH_3}\leq1.5\times10^{-4}$ (defined by saturation equilibrium).

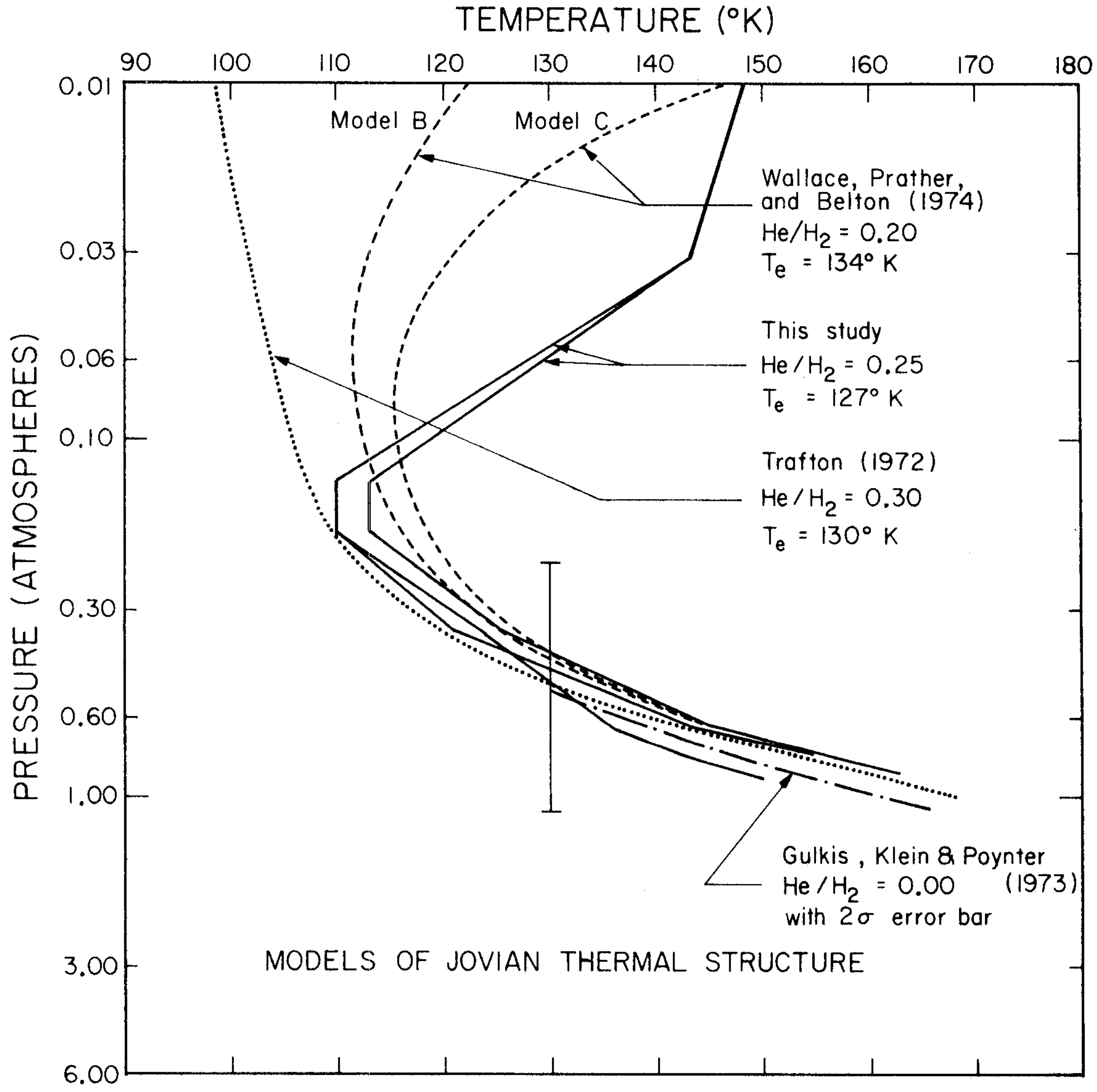

Fig. 15B. -Comparison of derived results with other models. Trafton (1972) and Wallace et al. (1974) models from radiative-convective equilibrium considerations. Gulkis et al. (1973) adiabat is best fit to microwave spectrum of thermal emission.

region (Gulkis et al., 1973), (3) the radiative-convective equilibrium model of Trafton (1972) constrained to fit an effective planetary temperature of 130°K, and (4) the radiative-convective equilibrium models B and C of Wallace, Prather, and Belton (1974) which are similar to the previous model but include possible results of solar heating of the atmosphere, and are fit to an effective planetary temperature of 134°K.

The radio occultation results (fig.15A) differ from ours by as much as 200 degrees at equivalent pressures, or by more than an order of magnitude in pressure at equal temperature levels. In order for the radio occultation results to be correct, there must be obscuring material of some sort which allows significant optical depth to be reached in the infrared at pressure levels substantially lower than in unobscured models, such as our "clear" models. There would be little difficulty in approximately reproducing the mean intensity for the 20 and 40 micron channels reported here as well as the 8-14 micron spectrum, with an obscuring layer in the thermal structure given by Kliore et al. However, the behavior of the obscuring layer would have to be quite complex in order to produce the observed limb-darkening in the 40 micron channel without assuming a local lapse rate which is superadiabatic. In addition, there remains the disagreement with the Gulkis et al. (1973) model fit to the microwave emission, which should be minimally affected by such scatterers. There would also be great difficulty in reproducing the observed path-lengths for hydrogen in the visible and near infrared were this obscuring layer optically thick at these lower wavelengths. Figure 15A includes an indication of the depth at which a reflecting layer must be placed in order to duplicate the path-length for H_2 derived by various observers. (For reference, CH_4 and NH_3 reflecting layer positions are also indicated.) For all abundance measurements, the reflecting layer is at a pressure greater than one atmosphere. It is difficult to see how the path-length could be increased to this extent by multiple scattering near the 0.01 atm level where Kliore et al. propose to put the obscuring material.

The correlation between the radio results and our models may be subject to some systematic errors. A drop in the temperature derived for a given pressure is achieved by lowering the refractivity of the atmospheric constituents, or by lowering the mean molecular weight by a factor of about one half in order to approximate our results. The requisite drop in the mean molecular weight is impossible, assuming hydrogen and helium as the major atmospheric constituents. Alternatively, a drop in the refractivity provided by hydrogen and helium is not possible with simple molecules as the refractivity generally increases with molecular weight. An alternative would require a continuous mixture of electrons with neutral particles, lowering the net refractivity to the observed levels, but no further. This necessitates the action of an ionizing mechanism effective down to the levels of several atmospheres in pressure. Moreover, the number of electrons in the occultation ray path must not be great enough to severely attenuate the received signal. The discrepancy of these results with ours and the microwave emission model remains unresolved and deserves further study. We mention the difficult inversion problem of multipath propogation in the neutral atmosphere as an additional possibility.

Our models all lie within the region considered by Gulkis et al. (1973) as a fit to the microwave spectral data to within the two standard deviation level (error bar shown in fig. 15B). The results of this paper also come close to some of the preliminary models of Taylor and Hunt (1972) in fitting the 8 - 14 micron ground-based spectral observations. These are not shown in Fig. 14, but they are discussed in Part 3 of this thesis.

As shown in Fig. 15B, Trafton's radiative convection model with He/H_2 - 0.30 and $Te = 130^\circ K$ is in approximate agreement with the results of this study in the adiabatic region. However, higher in the atmosphere, the deviation in the thermal structure is much greater. Trafton's model gives significantly lower intensities in the 20 micron channel than those observed, particularly toward the limb. Such models by Wallace et al. (1974) which are compositionally similar are also close to the thermal structure of the SEB model in the adiabatic regime. Higher in the atmosphere, the temperatures of the models rises, due to heating by the thermalization of sunlight absorbed by CH_4 in model B, and the additional absorption of ultraviolet solar radiation by a distribution of particulate materials in model C. Model C is more similar to the models, but the inversion is not so steep. The structure of this inversion is largely determined by the 8 - 14 micron spectral study, however, and will be discussed further in Part 3.

Further observational work in the thermal infrared should be done in the spectral region used as the data base for these observations. Such observations, like those of Houck et al. (1974), would establish the validity of the assumptions made in this study, such as the extent to which H_2 and NH_3 alone control the opacity. On the other hand, bolometric thermal infrared observations made outside the bulk of the earth's atmosphere with a reliable calibration would yield values for the effective temperature of the planet (for the latitudes facing the earth) which would be completely model-independent. Further work should also be done in the laboratory to establish with somewhat better accuracy the structure and intensity of the NH_3 rotational band which is so important in the 100 cm^{-1} region.

VI. CONCLUSIONS

The data retrieved by the 20 and 40 micron channels of the Pioneer 10 infrared radiometer have been used to generate simple models of the average vertical thermal structure of the outer Jovian atmosphere above the South Equatorial Belt (SEB) and the South Tropical Zone (STrZ). Additional models have been generated for the thermal structure over the North Equatorial Belt (NEB) and the Great Red Spot. These models are summarized in Figs. 7A, 9A, 10A, and 11. Models consistent with the data are composed of a primarily hydrogen atmosphere with 0 - 35% dilution in volume by helium. All models contain no scattering and pure gaseous absorption, except for a thick obscuring layer at a well-defined location which matches the STrZ data and provides minimum deviation from the thermal structure derived from data in the SEB region. This "cloudy" model is more appealing than the "clear" model because of (1) its consistency with 5 micron flux variations between belts and zones, (2) its correlation with the visible albedo changes, and (3) the coincidence of the obscuration level with the ammonia saturation level.

In all models, the tropopause temperature is cooler in the STrZ than the SEB; the NEB is slightly cooler than the SEB; and a possible model for the thermal structure over the Red Spot is about 5 degrees cooler than the STrZ at the tropopause. The cooling at the STrZ tropopause with respect to the same level in the SEB is consistent with both (1) radiative equilibrium with a cooler local effective temperature, and (2) a higher albedo and, therefore, less heating by absorbed sunlight.

The models are generally consistent with spectral fits determined by Gulkis et al. (1973) for microwave emission data, but they are quite inconsistent with the results of the neutral atmosphere inversion of the Pioneer 10 radio occultation results (Kliore et al., 1974). A fit to both the radiometer data and the radio occultation data might be made by adding an infrared obscuring layer close to the 0.05 atm level. However, the inconsistency between the radio occultation data and the microwave data would still exist, and the presence of an obscuring layer would be inconsistent with path-lengths derived from data in near infrared and visible wavelengths for H_2 absorption lines. The models derived in this paper are hotter than the radiative-convective equilibrium models of Trafton (1972) and Wallace et al. (1974) at levels near the tropopause and above. This is partly due to different effective temperatures (ours is cooler than theirs).

Spectra generated by the models are used to estimate local effective temperatures for the SEB (129°K) and the STrZ (126°K). Both these values are below the effective planetary temperature (134°K) measured by Aumann et al. (1969) and Armstrong et al. (1972).

REFERENCES

Armstrong, K.R., Harper, D.A., Jr. and Low, F.J. 1972, "Far-Infrared Brightness Temperatures of the Planets." Astrophys. J., 178 L89-L92.

Aumann, H.H., Gillespie, C.M., Jr. and Low, F.J. 1969, "The Internal Powers and Effective Temperatures of Jupiter and Saturn." Astrophys. J., 157, L69-L72.

Axel, L. 1972, "Inhomogeneous Models of the Atmosphere of Jupiter." Astrophys. J., 173, 451-468.

Chahine, M.T. 1968, "Determination of the Temperature Profile in an Atmosphere from its Outgoing Radiance." J. Opt. Soc. Amer., 58, 1634-1637.

Chase, S.C., Ruiz, R.D. Munch, G., Neugebauer, G., Schroeder, M., and Trafton, L.M. 1974, "Pioneer 10 Infrared Radiometer Experiment: Preliminary Results." Science, 183, 315-317.

Conrath, B.J. and Revah, I. 1972, "A Review of Non-statistical Techniques for the Estimation of Vertical Atmosphere Structure from Remote Infrared Measurements.: in Mathematics of Profile Inversion, ed. L. Colin, NASA TM X-62, 150, Pp. 1-36 - 1-99.

Danielson, R.E. 1966, "The Infrared Spectrum of Jupiter." Astrophys. J., 143, 949-960.

Divine, T.N. 1971, "The Planet Jupiter (1970)." NASA Space Vehicle Design Criteria (Environment) NASA SP-8069, Dec.

Dowling, J.M. 1968, "The Rotation-Inversion Spectrum of Ammonia." J. Molec. Spectrosc., 27, 527-538.

Encrenaz, Th. and Gautier, D. 1973, "An Iterative Method to Infer the Jovian Atmospheric Structure from Infrared Measurements." Astron. and Astrophys., 26, 143-147.

Gille, J.C. and Lee, T-H. 1969, "The Spectrum and Transmission of Ammonia under Jovian Conditions." J. Atmos. Sci., 26, 932-940.

Gillett, F.C. 1973, unpublished communication.

Gillett, F.C., Low, F.J., and Stein, W.A. 1969, "The 2.8-14 Micron Spectrum of Jupiter." Astrophys. J., 157, 925-934.

Gillett, F.C. and Westphal, J.A. 1973, "Observations of 7.9-Micron Limb Brightening on Jupiter." Astrophys. J., 179, L153-L154.

Goody, R.M. 1952, "A statistical Model for Wider Vapour Absorption." Quant. J. R. Met. Soc., 78, 165-169.

Goody, R.M. 1963, Atmospheric Radiation, Part I: Theoretical Basis, (Oxford, Clarendon Press) 436 pp.

Gulkis, S., Klein, M.J., Poynter, R.L. 1973, "Jupiter's Microwave Spectrum: Implications for the Upper Atmosphere." IAU Symposium on Exploration of the Planetary System, Torun, Poland.

Houck, J. Pollack, J.B., Schack, D., and Reed, R. 1974, "Aircraft Observations of Jupiter Between 16 and 40 Microns: A Determination of the Helium to Hydrogen Ratio and the Vertical Temperature Structure, 5th Annual Meeting, Div. of Planetary Sciences, Am. Astron. Soc., Palo Alto, Calif.

Hunt, G.E. and Bergstralh, J.T. 1974, "Structure of the Visible Jovian Clouds." Nature, 249, 635-636.

Hunten, D.M. and Münch, G. 1973, "The Helium Abundance on Jupiter." Sp. Sci. Rev., 14, 433-443.

Ingersoll, A.P. and Cuzzi, J.N. 1969, "Dynamics of Jupiter's Cloud Bands." J. Atmos. Sci., 26, 981-985.

Kliore, A., Coin, D.L., Fjeldbo, G., Seidel, B.L., and Rasool, S.I. 1974, "The Atmospheres of Io and Jupiter Measured by the Pioneer 10 Radio Occultation Experiment." 17th Plenary Meeting of COSPAR, Sao Paulo Brazil.

Lasker, B. 1963, "Wet Adiabatic Model Atmospheres for Jupiter." Astrophys. J., 138, 709-719.

Lewis, J. 1969, "The Clouds of Jupiter and the NH_3-H_2O and NH_3-H_2S Systems." Icarus, 10, 365-378.

Low, F.J. 1966, "Observations of Venus, Jupiter and Staurn at $\lambda 20\mu$." Astrom. J., 71, 391.

Low, F.J. and Davidson, A.W. 1965, "The Thermal Emission of Jupiter and Saturn." Bull. Amer. Astron. Soc., 1, 200.

Margolis, J.S. 1971, "Studies of Methane Absorption in the Jovian Atmosphere. III. The Reflecting Layer Model." Astrophys. J. 167, 553-558.

Margolis, J.S. and Hunt, G.E. 1973, "On the Level of H_2 Quadrupole Absorption in the Jovian Atmosphere." Icarus, 18, 593-598.

Mason, H.P. 1970, "The Abundance of NH_3 in the Atmosphere of Jupiter." Astrophys. and Space Sci., 7, 424-436.

Murphy, R.E. and Fesen, R.A. 1974, "Spatial Variations in the Jovian 20-Micrometer Flux." Icarus, 21, 42-46.

Newburn, R.L. and Gulkis S. 1972, "A Survey of the Outer Planets Jupiter, Saturn, Uranus, Neptune, Pluto, and Their Satellites." Space Sci. Rev., 14, 179-271.

Orton, G.S. and Gillett, F.C. 1974, "Thermal Structure of the Outer Atmosphere of Jupiter and Saturn from Center-to-Limb Observations in the Thermal Infrared." 5th Annual Meeting, Amer. Astron. Soc., Div. of Planetary Sciences, Palo Alto, Calif.

Owen, T. 1969, "The Spectra of Jupiter and Saturn in the Photographic Infrared." Icarus, 10, 355-364.

Pilcher, S.B., Prinn, R.B., McCord, T.B. 1973, "Spectroscopy of Jupiter: 3200 to 11,200 Å." J. Atmos. Sci., 30, 302-307.

Ridgway, S. 1974, "The Infrared Spectrum of Jupiter: 750-1700 cm^{-1}." 5th Annual Meeting, Amer. Astron. Soc., Div. of Planetary Sciences, Palo Alto, Calif.

Smith, W.L. 1970, "Iterative Solution of the Radiative Transfer Equation for the Temperature and Absorbing Gas Profile of an Atmosphere." Appl. Opt., 9, Pp. 1993-1999.

Taylor, F.W. 1972, "Temperature Sounding Experiments for the Jovian Planets." J. Atmos. Sci., 29, 950-958.

Taylor, F.W. and Hunt, F. 1972, "The Infrared Spectrum of Jupiter and Radiative Properties of the Clouds." 3rd Annual Meeting, Amer. Astro. Soc., Div. of Planetary Sciences, Kona, Hawaii.

Trafton, L.M. 1965, "A Study of the Energy Balance in the Atmospheres of the Major Planets." Ph.D. Thesis, Calif. Institute of Technology.

Trafton, L.M. 1967, "Model Atmospheres of the Major Planets." Astrophys. J., 147, 765-781.

Trafton, L.M. 1972, unpublished communication.

Trafton, L.M. 1973a, "A Comment on Jovian Greenhouse Models." Icarus, 19, 244-246.

Trafton, L.M. 1973b, "On the He-H_2 Thermal Opacity in Planetary Atmospheres." Astrophys. J., 179, 971-976.

Wallace, L., Prather, M., and Belton, M.J.S. 1974, "The Temperature Structure of the Atmosphere of Jupiter." Atrosphys. J., 193, 481-493.

Wark, D.Q. and Fleming, H.E. 1966, "Indirect Measurements of Atmospheric Temperature Profiles from Satellites. I. Introduction." Mon. Weather Rev., 94, 351-362.

Westphal, J.A. 1971,"Observations of Jupiter's Cloud Structure near 8.5μ." in Planetary Atmospheres,ed. C.Sagan et al., Springer-Verlag,New York,Pp.359-362.

Westphal, J.A., Matthews, K., and Terrile, R.J. 1974, "5-Micron Pictures of Jupiter." Astrophys. J., 188, L111-L112.

Westphal, J.A. and Terrile, R.J. 1974, unpublished communication.

Wiedenschilling, S.J. and Lewis, J.S. 1973, "Atmospheric and Cloud Structures of the Jovian Planets." Icarus, 20, 465-476.

Wildey, R.L. and Trafton, L.M. 1972, "Studies of Jupiter's Equatorial Limb Darkening During the 1965 Apparition." Astrophys. J. Suppl. (No. 194), 23, 1-34.

PART 3

OBSERVATIONS AND ANALYSIS OF 8-14 MICRON THERMAL EMISSION OF JUPITER: A MODEL OF THERMAL STRUCTURE AND CLOUD PROPERTIES

I. INTRODUCTION

This study attempts to determine an accurate representation of the average vertical thermal structure of the atmosphere of Jupiter in the region roughly bounded by 1.0 to 0.01 atmospheres in pressure. Certain aspects of the cloud structure are also defined. This study is both (1) a communication of observations and (2) an analysis of a broader set of data in the 8-14 micron region. (1) Spatially resolved observations of Jupiter in the thermal infrared near 8 microns made by the author and Dr. Fred Gillett of the Kitt Peak National Observatory with the Palomar Mountain 200-inch telescope are reported in section II. (2) A simple model of the vertical thermal structure and clouds is described in sections III and IV, which conforms to both spectral and center-to-limb observations in the 8-14 micron wavelength region, including those given in this report.

Below the level of about 0.10 atm pressure, the model derived here makes use of the thermal structure of the Pioneer 10 infrared models (Part 2). The thermal structure for the region above the 0.10 atm pressure level is derived to be consistent with ground-based 8-14 micron data. Both model sets were derived concurrently. Within certain limits, largely imposed by assumptions regarding chemical composition, the final model presented here is most consistent with both Pioneer 10 infrared data and the ground-based 8-14 micron data.

II. OBSERVATIONS

The observations reported in this section were originally motivated by the limb-brightening observations of Gillett and Westphal (1973) near 8 microns. The limb-brightening, observed at a wavelength where the Jovian spectrum implies the presence of the 7.7 micron fundamental band of methane in emission, confirmed the existence of a thermal inversion in the outer atmosphere of Jupiter. Furthermore, it gave considerable support to the identification of the spectral feature near 8 microns as due to CH_4 emission, rather than a "window" resulting from the absence of strong opacity sources at that wavelength. However, analysis of this data in quantitative terms was hampered by the lack of knowledge of the aperture position with respect to the true radius of the planet. The observations reported here were made in order that a better positional control be maintained. These observations have been presented by Orton and Gillett (1974) and were made concurrently with the scans of Saturn reported by Gillett and Orton (1975). It is with Dr. Gillett's kind permission that this author presents the observations made by both of us as a part of the larger quantitative analysis of the infrared emission characteristics of the planet with respect to its mean vertical thermal structure and cloud properties.

On the night of 10/11 September 1973, the 200-inch telescope was used with the cooled filter wheel spectrometer used by Gillett and Westphal. This spectrometer has an average resolution of $\Delta\lambda/\lambda \approx 0.015$, and was used with an aperture size of 3 seconds of arc. Each scan of the planetary disk, lasting on the order of 20 minutes, was made with simultaneous photography which provided a check on both the aperture position at several points in the scan as well as the scan orientation. Care was taken so that scans were always oriented closely parallel to the equator of Jupiter.

At 8.15 microns, scans were made over the Jovian South Tropical Zone (STrZ), as it was wide enough to fill the aperture and was a reasonably homogeneous region at visible wavelengths, as well. No observations at shorter wavelengths, closer to the CH_4 band center, were possible because of the increased signal attenuation by telluric water vapor. A scan was taken at 8.44 microns, outside the wavelength region dominated by methane opacity; unfortunately a guiding error placed this scan near the equatorial region rather than the STrZ. The scans were apparently affected by a drift in the zero baseline; this has been approximately removed by a linear interpolation between the sky signal beyond the east and west limbs of the planet.

The scans of Jupiter are shown in figs. 1 and 2 for 8.44 microns and 8.15 microns, respectively. The intensity is normalized to the value at the disk center in all scans. For the single 8.44 micron scan (fig. 1), the relative error has been estimated from the noise in the sky intensity; for the 8.15 micron scans (fig. 2) it has been estimated from the deviation of the normalized data from the mean of the four scans which comprise this figure. This error is shown in both figures as a vertical bar at disk center. Scans of α Tauri were made through the aperture center to determine the system response. The width of the response function at half the maximum sensitivity (half-width) was determined as 2.8 ± 0.2 seconds of arc. The response function is displayed at an arbitrary normalization on the same spatial scale. The radius is

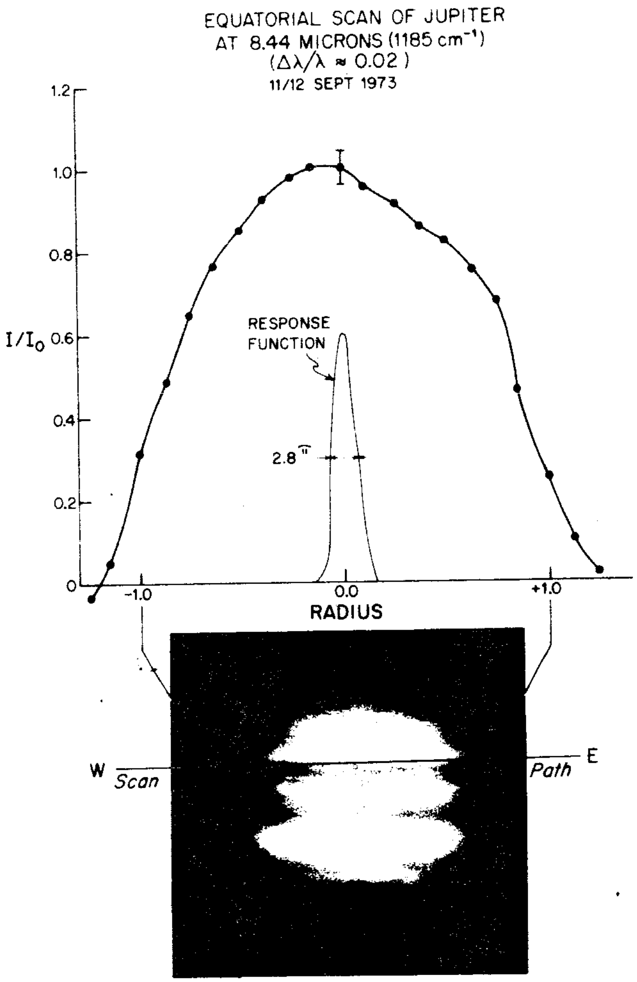

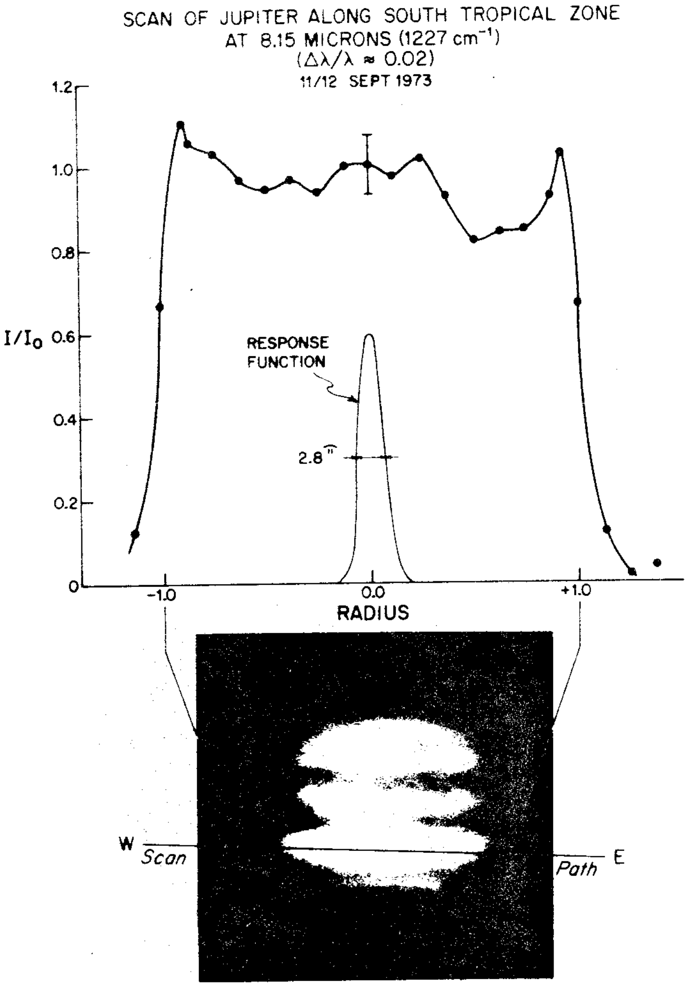

Fig. 1. (left) -Results and path of 8.44 micron scan.

Fig. 2. (right) -Average results and path of 8.15 micron scan. In both figures, data are normalized to value at center.

normalized to unity at the position of the edge of the visible disk: negative values represent positions west of the disk center, and positive values are east.

The 8.44 micron intensity displays limb-darkening, as in the scan by Gillett and Westphal at the same wavelength. It is expected, therefore, that unit optical depth at this wavelength is in the neighborhood of region where the temperature is decreasing with height. The 8.15 micron intensity which is in the region dominated by methane opacity shows definite limb-brightening, confirming again the association of limb-brightening with this emission feature. Moreover, each of the four scans making up this average result also displays a weak maximum at the center. The simplest interpretation requires radiation emerging from the limbs to originate in the region of thermal inversion, whereas radiation emerging from near the disk center originates from a level in the atmosphere where the temperature is decreasing with height. In this interpretation, therefore, the observed 8.15 micron radiation is required to originate quite close to an atmospheric level characterized by a temperature minimum in the average vertical thermal structure.

The sense of east-west asymmetry observed, however, was not consistent among the scans. Therefore, the asymmetry of the data displayed in fig. 2 represents only a simple average of the observed intensities, and, in view of the difficulties with the baseline drift, it may not be real.

The quantitative interpretation of these scans with respect to models of the atmospheric structure shall be discussed later in this report.

III. MODEL PARAMETERS AND RADIATIVE TRANSFER CALCULATIONS

The model presented in this paper has been derived by matching the average vertical thermal structure and the opacity sources in the model with the available 8-14 micron data. This data includes the spectral observations of Gillett et al. (1969), Aitken and Jones (1972), and a recent unpublished spectrum taken by Gillett (1973). These spectra are shown in figs. 3A and 3B. At Gillett's suggestion, the Gillett et al. (1969) spectrum has been modified to agree with the calibration used in his recent observations. The Aitken and Jones spectrum has been degraded to the resolution of the other spectra and the 9.5 micron region has been omitted, due to its high noise level. Spatially resolved observations include the center-to-limb data presented in the last section, the center-to-limb data of Gillett and Westphal (1973) at 7.94 microns, and Westphal's (1971) meridional scans of the planet for bandpasses of 8.2-9.2 microns and 8.2-13.5 microns. The latter observations constitute the only measured differences between the belt and zone intensities in the 8-14 micron region.

In each model, the vertical thermal structure as a function of pressure has been established in a manner identical to that used in Part 2 of this thesis. The deep atmosphere is assumed to be in convective equilibrium. The local gravitational acceleration has been assumed to be 2288 cm/s^2 (Newburn and Gulkis, 1972), relevant to the equatorial region where most of the observations were made.

The opacity sources in the model are indicated in fig. 3 where each is expected to dominate the spectrum. For wavelengths of about 12 microns or more, the collisionally-induced dipole of H_2 is strongest.

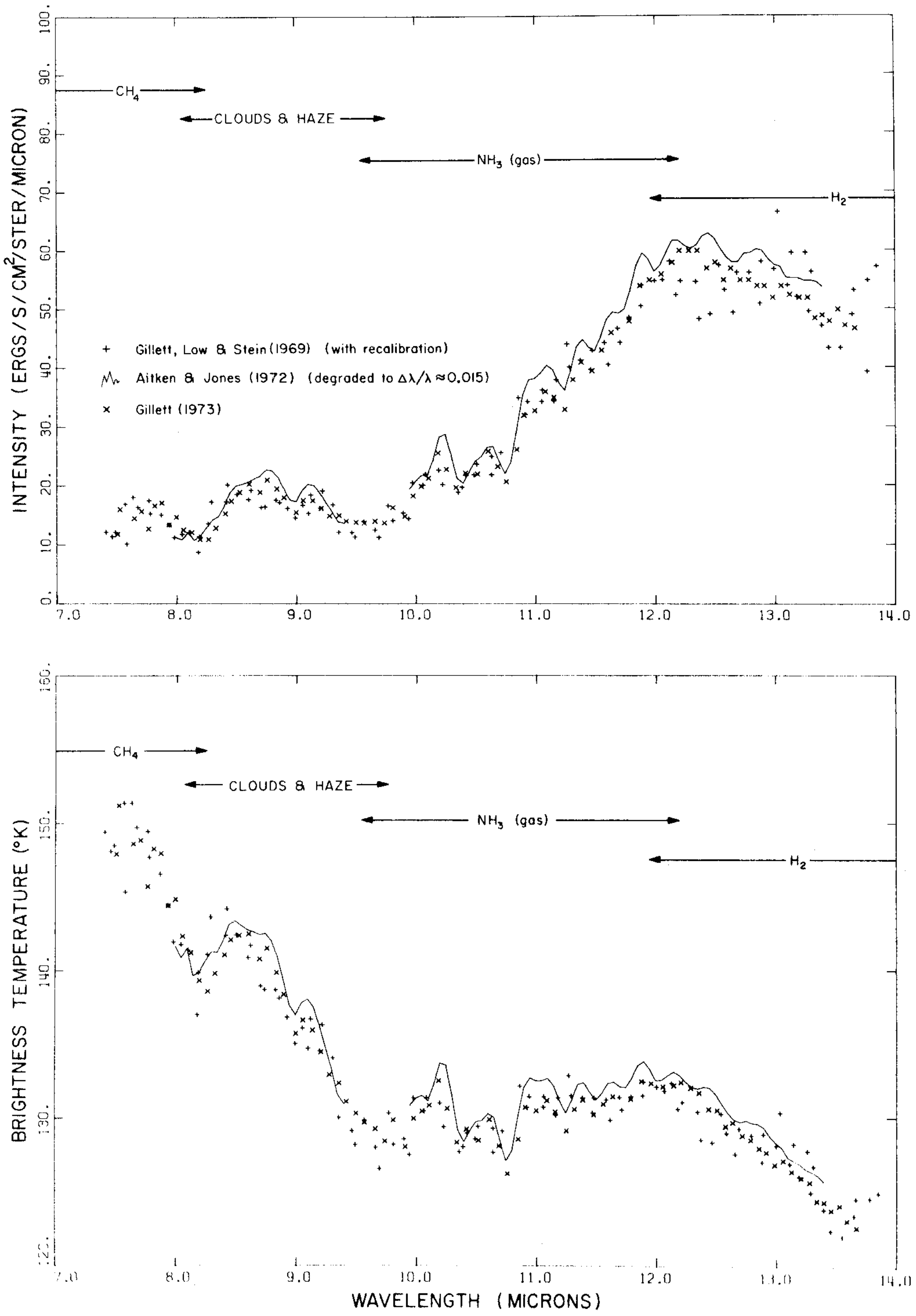

Figs. 3A. (top) 3B. (bottom) -Spectra of Jupiter from ground-based observations ($\Delta\lambda/\lambda \approx 0.015$). Opacity sources expected to dominate indicated in appropriate wavelength ranges.

The dominance of H_2 opacity at these long wavelengths is assumed in the Pioneer 10 infrared models and is generally confirmed by the spectral observations of Houck et al. (1974) in the 17-40 micron range. Gaseous ammonia absorption is expected to dominate the spectrum from approximately 9.5 to 12.0 microns. Structure in the spectrum of Aitken and Jones (with the original resolution) and in the very high resolution spectrum of Ridgway (1974a, 1974b) is correlated with line positions in the $\nu_2 NH_3$ fundamental band. The region at wavelengths shorter than about 8.2 microns is dominated by the ν_4 fundamental band of CH_4. Since this band is seen as an emission feature, radiation at these wavelengths is expected to originate from a region where temperature is increasing with height. This interpretation is consistent with the limb-brightening observations of Gillett and Westphal at 7.94 microns. Finally, in the region from 8.2 to 9.5 microns, the molecular opacity sources listed above are not sufficient to accurately describe the spectrum. The model therefore contains both optically thick clouds and a haze of solid NH_3 particles which are considered successful in approximately describing the spectrum shown in fig. 3. Ridgway (1974a) has also identified C_2H_2 and C_2H_6 in very high resolution spectra. The influence of these constituents on the spectrum at the resolution used in this study is expected to be negligible, however, and so they have been ignored.

The opacity of hydrogen was computed using the method described in Trafton (1965, 1967), with values of the opacity coefficients equal to those used in Trafton (1973) and Chase, et al. (1974). The method is identical to that used in Part 2 of this thesis. The H_2 opacity is estimated at all wavelengths in the 8-14 micron region where radiative transfer calculations are made in this study, although it is of importance only at wavelengths equal to or greater than about 12 microns, as stated above.

The opacity of gaseous NH_3 has been computed using the random band technique described by Goody (1952, 1963), since the great number of individual lines contributing to the total opacity would make direct computations exceedingly tedious and time-consuming. Line strength values have been taken from Taylor (1973a), who lists all lines with (room temperature) strengths greater or equal to 1×10^{-5} cm^{-2} atm^{-1}. The random band parameters listed by Gille and Lee (1969) have not been used because of the relative completeness of Taylor's compilation and because Taylor's line strengths give better agreement with the laboratory transmission data of France and Williams (1966). Line width values as a function of temperature, pressure, and composition are calculated as summarized in Appendix A. The uncertainty in the estimate of the NH_3 opacity has been calculated by use of different assumptions for the probability distribution of line strengths. This is explained in greater detail in Appendix A where the estimates used for the widths of individual lines are also given. The equivalent homogeneous path length, pressure, and temperature have been determined by use of an absorber-weighted approximation (Taylor, 1973a), similar to the Curtis-Godson approximation. Taylor has demonstrated that these approximations lead to adequate estimations for the transmission of the Jovian atmosphere when compared with the straightforward calculations.

The same random band technique has been used to estimate the opacity of CH_4 in the 8 micron region. Line strength values have been taken from Kyle (1968), who lists individual lines with angular momentum quantum number, J, from 1 through 16. As no line positions are given for $\lambda > 8.43$ microns ($\nu < 1186$ cm^{-1}), line positions and strengths have been extrapolated for higher rotational transitions. For line positions given by Kyle, it is observed that the frequencies of lines (with a given nuclear configuration) are adequately described by a linear dependence on J. Therefore, this linear dependence has been used to estimate line positions for $J = 16$ to $J = 25$. Similarly, it is found that line strengths are adequately described by an exponential dependence on J. This exponential dependence has been used to estimate line strengths for $J = 16$ to $J = 25$. The methane opacity contribution in the model for the wavelength range 8.33 to 8.70 microns should therefore be regarded with some caution; this extrapolation is used only because it is considered a better alternative than neglecting the methane opacity contribution in this region entirely. The estimation of the uncertainty in the opacity calculations is based on the different assumptions regarding the probability distribution of line strengths and the uncertainty in the widths of individual lines. Details of this estimate for CH_4 are also given in Appendix A. The absorber-weighted approximation has also been used to estimate equivalent homogeneous path conditions. Taylor (1972a) has shown that estimates for random band approximation and the absorber-weighted homogeneous path approximations have resulted in a reasonable estimate of CH_4 opacity relative to the straightforward calculations.

The effects of thick clouds and haze models are found to be important in describing the radiation emerging from the atmosphere for wavelengths between 8.1 and 9.5 microns. Thick clouds are modeled as black body surfaces which radiate at the temperature of the cloud top. The level of the cloud top defines the lower limit of the radiative transfer integral. The haze in the model follows the suggestion of Taylor and Hunt (1972) and has the absorption characteristics of solid NH_3 (Taylor 1973b). The optical thickness of the haze is given by the product of the absorption coefficient of the solid material times an effective thickness of solid material. Taylor and Hunt report that this is, in fact, a useful approximation of the effects of scattering for wavelengths on the order of 10 microns. The variation of effective haze thickness with height is one of the free parameters of the model. In some calculations, the influence of a grey absorbing haze has been computed by replacing the wavelength-dependent absorption coefficient of solid NH_3 by a constant at all wavelengths.

Calculation of normally emergent radiation was found to be an adequate representation of the radiation detected in the central 20% of the planetary disk, where most of the spectral observations were made. The plane-parallel approximation has not been used to calculate the increase in path-length for non-normally emergent radiation, because of the important contributions very close to the limb which are expected to greatly influence calculations of limb-brightening. Instead, the path-length increase at any layer has been calculated from a simple geometric consideration of the planetary curvature. This avoids the tendency to approach an infinite path-length at the extreme limb and replaces it with a finite value. The details of this calculation are given in Appendix B.

Center-to-limb scans of the planetary disk were simulated by computing a table of emergent radiation as a function of radial position on the disk, with a close spacing near the limb. The aperture response function is approximated by a series of concentric apertures, each with a constant response. The size and weight of each is designed to make the combination closely approximate the measured response of the aperture to a point source. The convolution of this combination of apertures was made with the tabulation of emergent radiation vs. radius assuming circular symmetry of the disk, which should be a valid approximation in view of the small aperture sizes used in the center-to-limb observations.

The numerical calculations have been tested as far as possible by independent means. The opacity calculations at each frequency correspond extremely well to Taylor's (1972b) plot of the location of the weighting function maximum vs. frequency. An exception is the region near 8.5-9.5 microns, where he has used the NH_3 random band parameters of Gille and Lee (1969), which are systematically higher than the parameters used here derived from Taylor's (1973a) compilation of gaseous NH_3 opacity data.

IV. RESULTS OF CALCULATIONS

This section demonstrates the model which has been derived as a best fit to spectral and center-to-limb data. As individual characteristics of the model can be derived unambiguously from specific wavelength regions in the spectrum, it will be shown how the model has been modified to fit the data in each region. The 12-14 micron region of the spectrum determines the thermal structure below the temperature minimum in the model. The region of the spectrum at about 8.1 microns and below determines the thermal structure in the region of the temperature minimum and the thermal inversion. The 9.5-12.0 micron region helps to determine the assumed distribution of the NH_3 gas as a function of height in the atmosphere. Finally, the 8.1-9.5 micron region determines the character of the clouds and the haze present in the atmosphere.

A. Summary of the Model

The spectrum of the best fit model is displayed in figs. 4A and 4B. The thermal structure is shown in fig. 5. In order to reduce computational time, the calculation of a nearly continuous spectrum resulting from the models has been abandoned in favor of a calculation of the intensity at twenty wavelengths. These wavelengths are at positions in the spectrum where individual features can be compared with results implied by the models. The vertical lines in figs. 4A and 4B (and in other figures comparing models with the spectrum) represent the uncertainty in the estimates of emergent intensity which result from the uncertainty in opacity estimates, as described in the last section. This uncertainty is smaller than the spread in the data. On the whole, the model fit to the spectrum is considered to be satisfactory.

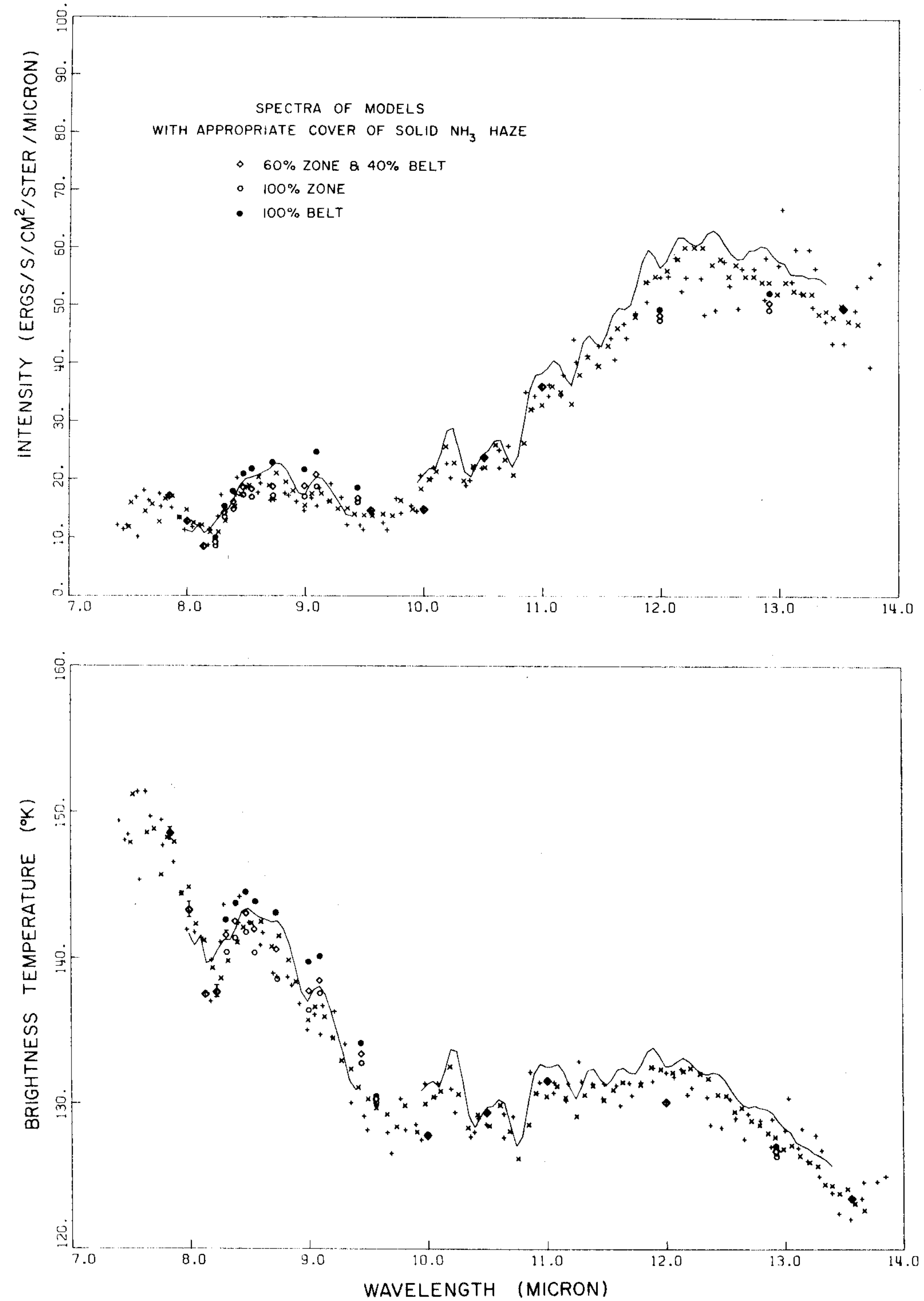

Figs. 4A.(top) 4B.(bottom) -Spectra of best fit model. Data as in figs. 3A and 3B. Error bars, where larger than symbols, indicate uncertainty in model spectrum from uncertainty in opacity estimates. Amount of obscuring haze varies from belt to zone.

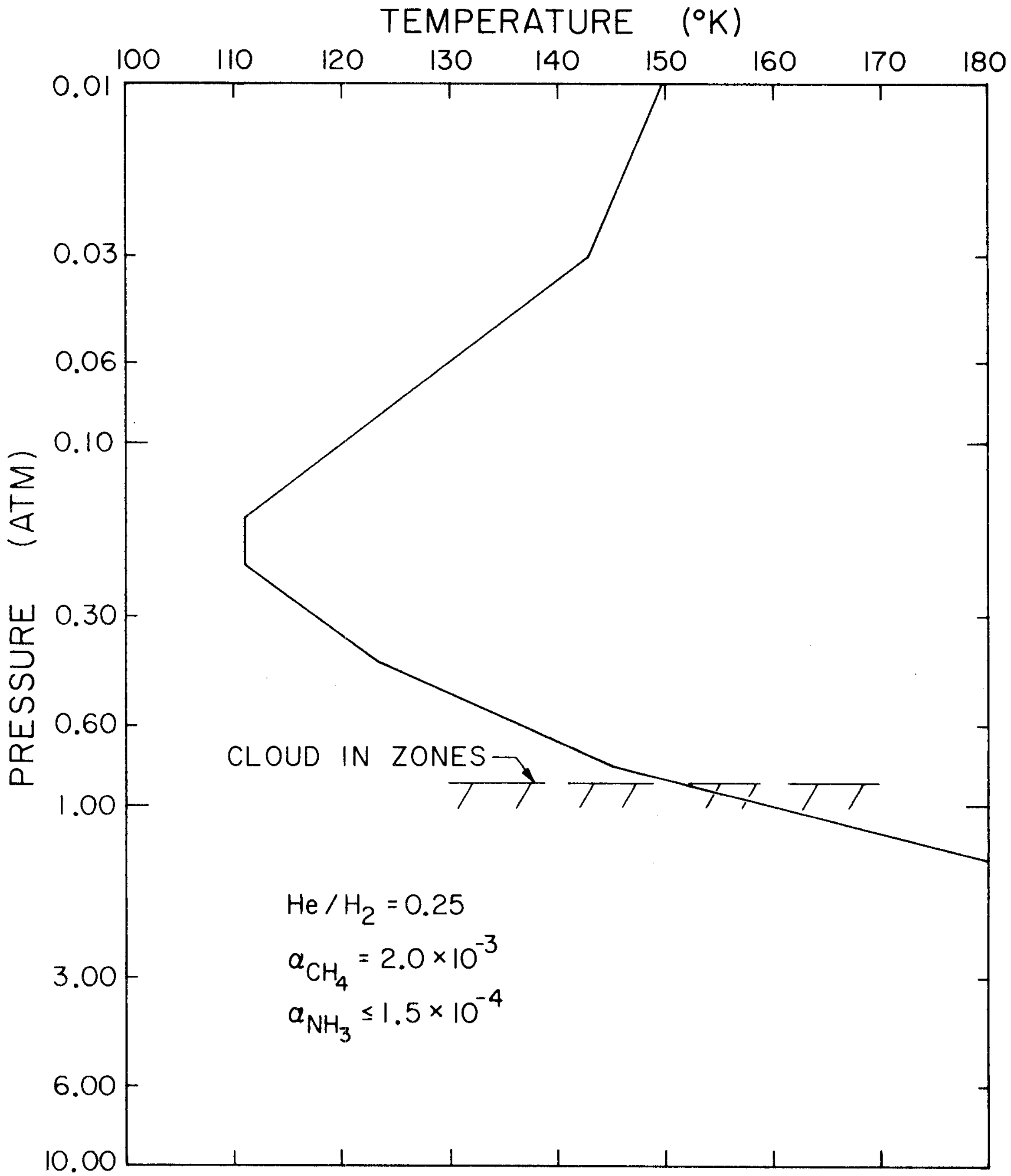

Fig. 5. -Best fit thermal structure. Level of thick cloud (in zones) is also shown. This structure produces spectrum shown in figs. 4A & 4B.

The composition of the model is taken to be predominantly H_2 with a mixture of 20% He by volume. This molar ratio, $He/H_2 = 0.25$, presents the best fit for models of the thermal structure describing Pioneer 10 infrared data. It has been adopted in the absence of any indication in the 8 - 14 micron spectral region suggesting a different composition. The molar mixing ratio of NH_3 in the deep atmosphere is taken as 1.5×10^{-4}. This value is consistent with the microwave spectrum in the neighborhood of the NH_3 inversion line near 1 cm wavelength (Gulkis et al., 1973) and with the relative abundance of NH_3 to H_2 determined from spectroscopic observation. Furthermore, this value is close to the mixing ratio implied by chemical equilibrium models of the atmosphere with a "solar" abundance of elements (Weidenschilling and Lewis, 1973). The molar mixing ratio of CH_4 is equal to 2.0×10^{-3}. This is higher by a factor of 3 than the value of 6.2×10^{-4} initially assumed in the model, which corresponds to the relative abundances of CH_4 and H_2 implied by spectroscopic observations and to the molar mixing ratio implied by the "solar" abundance chemical equilibrium models. The final mixing ratio is determined (to about a factor of two) by best fitting the 8 micron spectral region, the 8.15 micron center-to-limb data, and the 20 micron channel data of the Pioneer 10 infrared radiometer, all of which are sensitive to the region near the temperature minimum in some way.

In the model, there is a thick cloud in the zones which has a top near the 150°K (0.90 atm) level. Belts are free of the thick cloud. The haze of solid NH_3 particles, which overlies the thick cloud in the zones, exists in the belts also, but at lower concentrations.

The thick cloud presence in the zones is indicated by the Pioneer 10 infrared models for the South Tropical Zone (STrZ) data. The coincidence of the cloud location in those models with the NH_3 saturation level implies that the cloud physically consists of particles of frozen NH_3. The more diffuse haze above the 150°K level in belts and zones provides a good fit to the spectral characteristics in the 8.1 - 9.5 micron region. The difference between the abundance of the haze in belts and zones is necessary to fit the observed contrasts between belts and zones in Westphal's meridional scans of the planet.

The relative contribution of belts and zones to the spectra in the inner 20% of the disk, where the spectral observations were made, is taken to be equal to the relative areas covered by each near the disk center. A ratio of about 40% belts to 60% zones, with a 10% relative error, has been determined in two independent ways, first from the areas covered by dark and by light regions in visible photographs of the planet, and second, from the relative areas covered by bright and by dark regions, in 5 micron images of the planet (Westphal et al., 1974). Both techniques yield similar results. This modeling implicitly assumes that the emission from all zones or from all belts can be characterized in the same manner. While this is undoubtedly not strictly true, the difference in the radiation detected by Pioneer 10 between the North Equatorial Belt (NEB) and the South Equatorial Belt (SEB) is equivalent to a maximum difference of two degrees at equal pressure levels. The goals of this study, with respect to a determination of differences in the lateral variation of atmospheric conditions must, therefore, be limited to elucidation of some of the differences between belts and zones in general.

The thermal structure in both belts and zones has been assumed to be the same. The difference between the thermal structures for the SEB and "cloudy" STrZ Pioneer 10 infrared models is a maximum of 3°K and is located near the temperature minimum. The thermal structure used in the model is close to an average of the two (with somewhat more weight on the STrZ thermal structure). The results of using different thermal structures for each region, as implied by the Pioneer 10 data, are shown in figs. 6A & 6B. For these spectra, the haze contrast is the same as in the spectra shown in fig. 4. The spectrum of combined belt and zone intensities shows little change from the spectrum displayed in fig. 4. For bandpasses of 8.2 to 9.2 microns and 8.2 to 13.5 microns, corresponding to Westphal's (1971) observations, the belt to zone intensity contrast increases from 25% to 44% and from 7% to 12%, respectively, in going from fig. 4 to fig. 6.

B. Variations in the Thermal Structure Below the Temperature Minimum: 12. - 14. Micron Spectrum

The thermal structure below the temperature minimum in fig. 4 does not agree with the results of the Pioneer 10 infrared models (an average of SEB and "cloudy" STrZ thermal structures) as shown in fig. 7. The spectrum which results from modifying the thermal structure so as to agree with Pioneer 10 data is shown in fig. 8. The most dramatic changes in the spectrum are for the region between 12. and 14. microns, although changes are also noted in the 9.5-12. micron region, as well. The radiative transfer weighting functions for normally emergent radiation at 12.0 and 13.6 microns are also shown in fig. 7. It is clear that this region of the spectrum is sensitive to the thermal structure near the pressure levels of 0.4 to 0.6 atm, and that the Pioneer 10 model is some 4 to 5 degrees too hot.

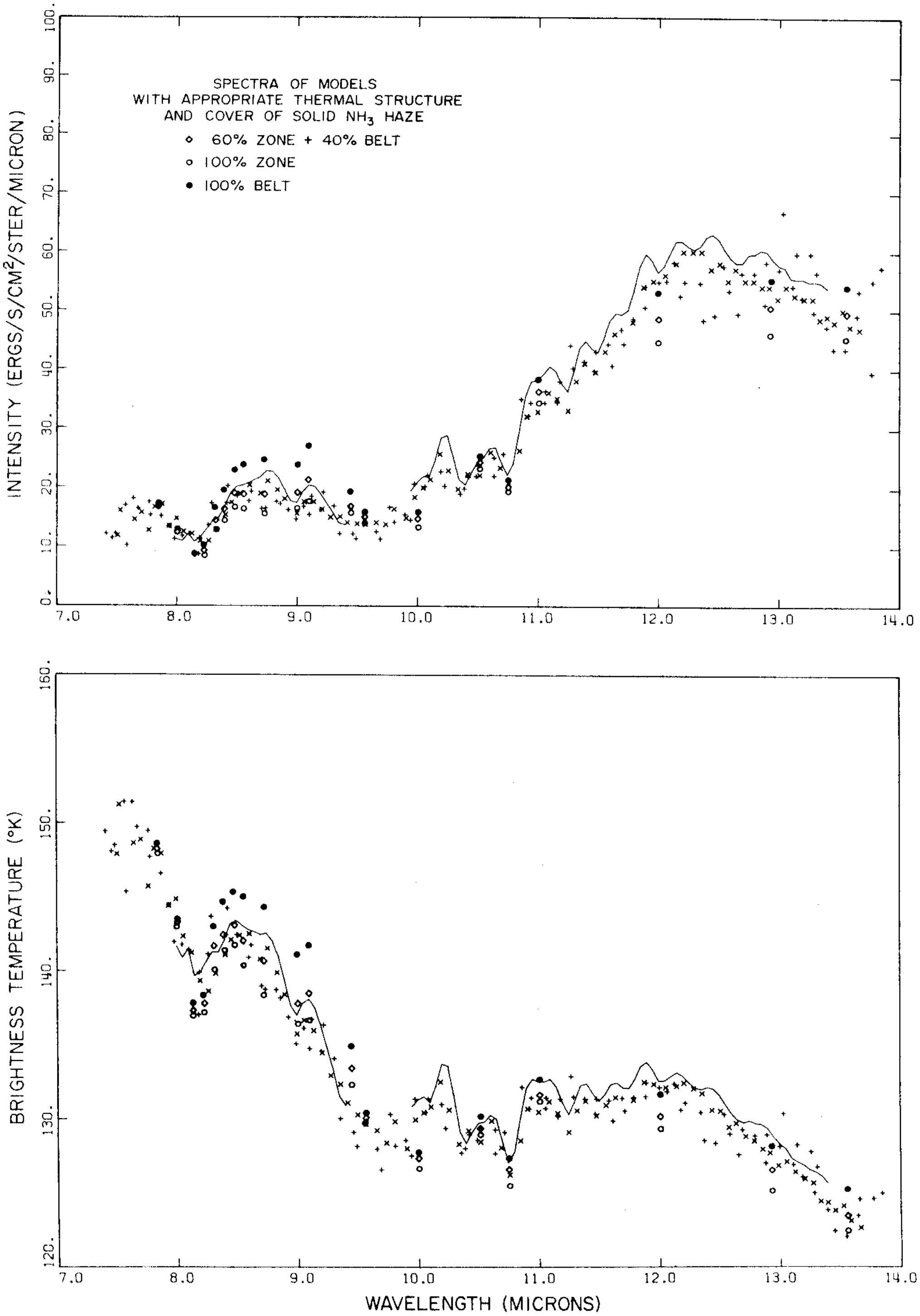

Figs. 6A. (top) 6B. (bottom) -Spectra of best fit model with variation of thermal structure from belt to zone, according to indications of Pioneer 10 infrared radiometer data. Data as in figs. 3A and 3B. Amount of obscuring haze also varies from belt to zone.

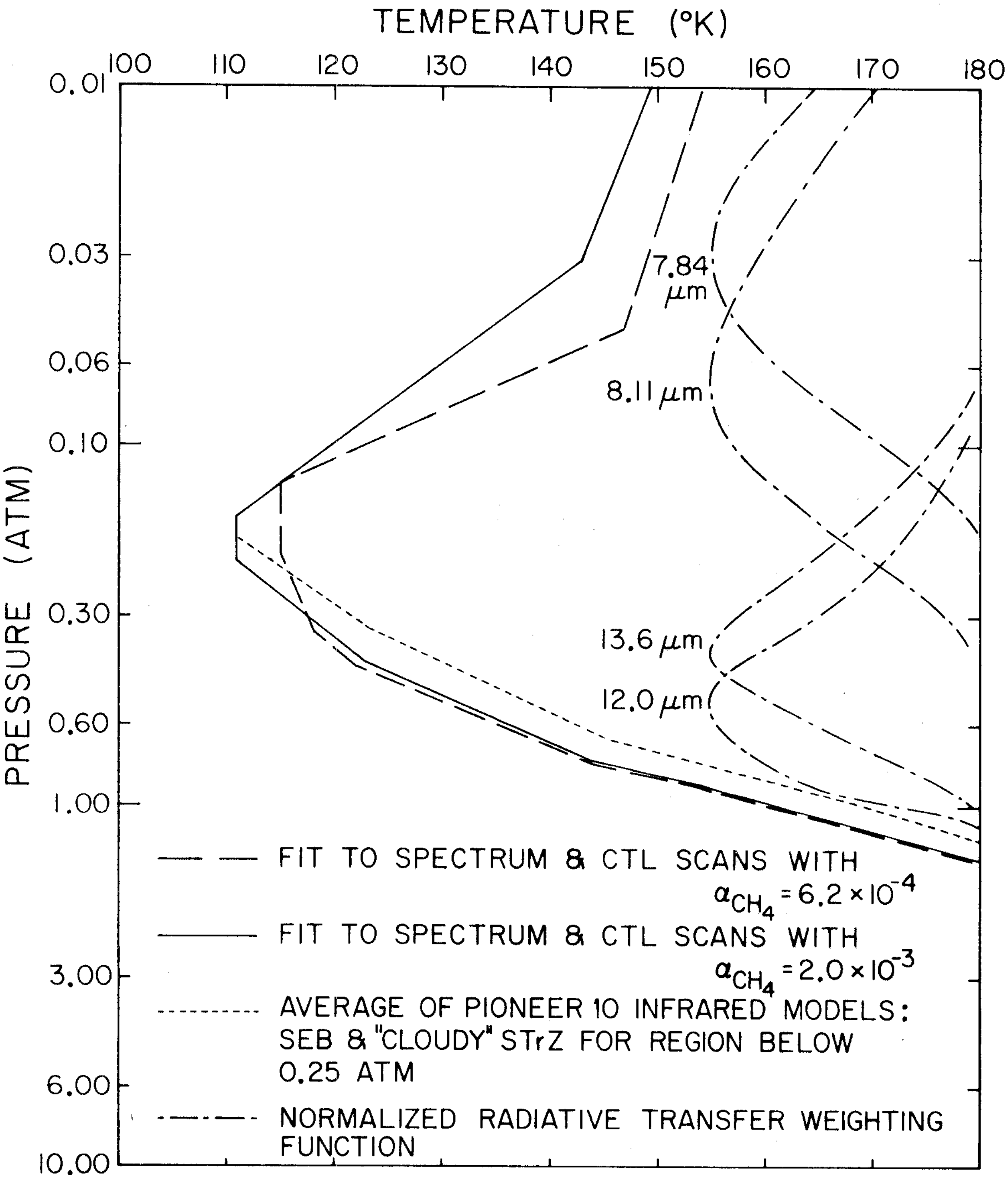

Fig. 7. -Alternate thermal structure models. Solid line is same as fig. 5. Differences are given in detail in text. Weighting functions (normalized) for normally emergent radiation are also displayed at four wavelengths.

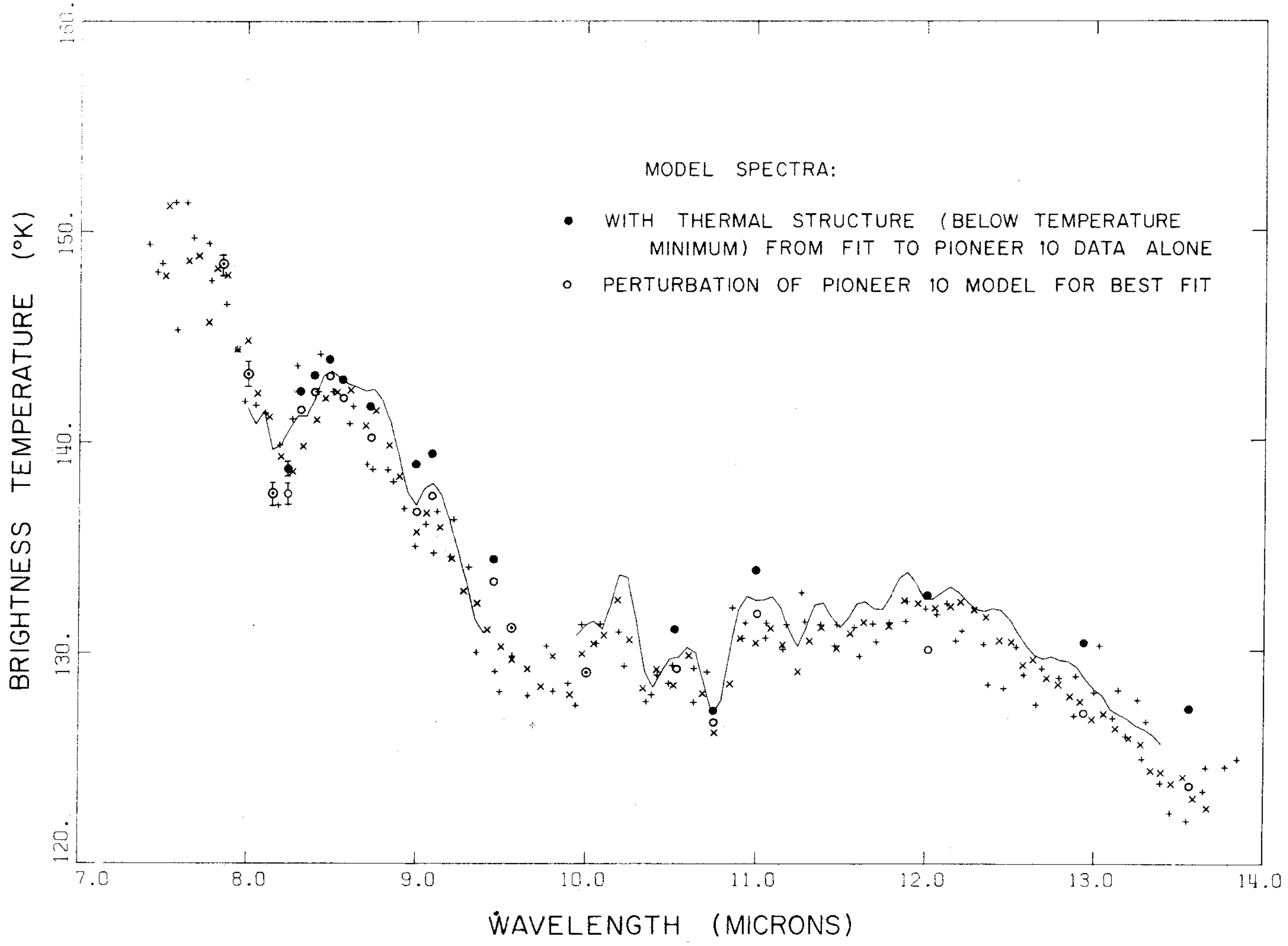

Fig. 8. - Spectra of alternate thermal structure models. Data as in Fig. 3B. Thermal structures are shown in Fig. 7. Molar mixing ratio of CH_4 is 6.2×10^{-4}.

This discrepancy of the Pioneer 10 infrared models with the data shown in fig. 8 is significant in several ways. It may denote a substantial systematic inconsistency in the calibration methods used. Barring this, it may indicate that the opacity of H_2 is stronger at 12 - 14 microns than the estimate used here, or that it is weaker at 20 to 40 microns. Not suprisingly, a change in the atmospheric chemical composition affects the opacity in the two spectral regions in the same way, and therefore does not resolve this problem.

The fit to the 12. - 14. micron spectral region has been achieved by uniformly moving the thermal structure derived from Pioneer 10 below the temperature minimum to levels where the pressure is 20% greater. This procedure probably makes a more realistic estimate of the thermal structure than a simpler model, such as an adiabat which continues up to the temperature minimum. The fit to the normalized limb structure data of each channel in the Pioneer 10 infrared radiometer is not expected to be affected by such a change in the pressure. This uniform change makes the implicit assumption that the same change is appropriate for the sections of the thermal profile to which each channel is most sensitive, but there is no information which would suggest a more reasonable alternative.

With this change in pressure relative to the Pioneer 10 model, the model spectrum is in good agreement with the data, as shown in figs. 4B and 8. One possible exception is the intensity at 12.0 microns, which is a bit low. This may indicate either that the opacity at this wavelength has been overestimated, or that the lapse rate near the 132°K level is too low and is somewhat closer to the adiabatic rate.

The uncertainty in the thermal structure determined by the 12 - 14 micron spectrum may be considered, first, on the basis of the uncertainty in spectral data and, second, on the basis of its variance from the thermal structures implied by the Pioneer 10 infrared data. The spread of observed values in the spectra (fig. 3) imply that the temperature at any pressure in the 0.4 - 0.6 atm region is determined to about ±1°K. On the other hand the difference between this thermal structure and Pioneer 10 infrared models is 8°K. The latter represents the uncertainty resulting from model assumptions or calibration differences.

C. Abundance of NH_3: the 9.5 - 12.0 Micron Spectrum

The 9.5 micron to 12.0 micron intensities are controlled by the opacity provided by molecular NH_3. Unit optical depth in this wavelength region is reached significantly above the level at which NH_3 first saturates, which is close to 150°K. The path-length for NH_3 absorption is therefore fully controlled by the saturation vapor pressure at each level, and not by the NH_3 mixing ratio at deep levels. Were the atmosphere significantly supersaturated with NH_3, the path lengths would increase with respect to the model presented here, which assumes saturation equilibrium. The intensities in this region would be lower, as a result. Alternately, for a model in which the abundance of NH_3 is significantly reduced by some mechanism, with respect to this model, the intensities in the 9.5 - 12.0 micron region would be greater than observed. The correlation of the 9.5 - 12.0 micron intensities with the data, for the case where the thermal structure has been devised so as to provide a fit to the 12. - 14. micron intensities independently, indicates that the assumption of saturation equilibrium appears to be a reasonable one.

Broad band 8 - 14 micron observations are significantly affected by the intensity in both 9.5 - 12.0 and 12. - 14. micron spectral regions (fig. 3A). Significant lateral variations in such observations would most plausibly indicate large lateral variations in either the thermal structure or the abundance of NH_3. Fig. 6A also demonstrates the 12% contrast in an 8.2 - 13.5 micron bandpass as a result of different thermal structures derived for belts and zones from Pioneer 10 infrared data. This is a bit higher than Westphal's (1971) broadband contrast observations, but it is significantly lower than the 20 - 30% contrast in recent 8 - 14 micron images of Jupiter obtained by Westphal and Terrile (1974).

In order to reproduce this contrast, either (1) the differences in the thermal structures of belts and zones must be larger than implied by Part 2 of this thesis or (2) the amount of NH_3 in belts must be below the abundance in zones. The first possibility might be correct if the contrast between belts and zones at 20 and 40 microns is higher than detected by the resolution of the Pioneer 10 infrared radiometer, which would appear doubtful. The second possibility requires NH_3 depletion in the belts relative to saturation equilibrium. Such a depletion would result, however, in higher intensities than observed in the 9.5 - 12.0 micron region, unless an additional compensating opacity source were present in the zones and active in this spectral region. This discrepancy appears to mandate further photometric observational work, with emphasis on spectral observations of belts and zones separately in the 9.5-13.6 micron region.

D. The Temperature Minimum and Thermal Inversion, the Molar Mixing Ratio of CH_4: the 7.8-8.1 Micron Spectrum

For the region near the temperature minimum and above, the thermal profile has been specified by the spectral data in the 7.84 and 8.11 micron region and the center-to-limb scan at 7.94 microns. A formalized inversion scheme, similar to the one used to derive thermal structures from the Pioneer 10 infrared data has not been used for several reasons. (1) The noise in the measured spectrum near 8 microns is fairly large and even the 7.94 and 8.11 micron weighting functions (shown in fig. 7) overlap each other to a considerable degree. (2) It is difficult to devise an effective approximation for the 7.94 micron weighting function near the limb, as the finite aperture size allows some confusion with the region beyond the edge of the disk. (3) There is some overlap in the region "sampled" by the 20 micron Pioneer 10 channel near the limb and the 8.11 micron spectral measurement, but the difference in the sizes of the respective weighting functions makes a quantitative comparison and evaluation of the two rather difficult.

The following method has been used to determine the structure of the thermal inversion shown in fig. 7. A reference level is established near 0.03 atm pressure at the approximate location of the median of the 7.94 micron weighting function (for normally emergent radiation). The available data are used to determine a crude thermal structure, characterized by the following three variables: (1) a constant lapse rate above the reference level, (2) the temperature of the reference level and (3) a constant lapse rate below the reference level. The 7.94 micron limb brightening data (Gillett and Westphal, 1973) is used to determine (1) the lapse rate above the reference level. It shows a maximum near the limb some 25-27% above the intensity at disk center. The spectral data between 7.84 and 8.11 microns is used to determine (2) the reference level temperature and (3) the constant lapse rate below the reference level.

The uncertainty of the absolute temperatures in the inversion, estimated on the basis of the dispersion in the spectral data, is about $\pm 2^{\circ}$K. However, the asymmetric limb brightening observed by Gillett and Westphal (1973) at 7.94 microns creates some ambiguity in the value of the lapse rate above the 0.03 atm pressure level. For the less brightened (east) limb, the upper inversion lapse rate may be zero. In this case, spectral data is best matched by an increase in the temperature at 0.03 atm of about 8 degrees. For the brighter (west) limb, the upper inversion lapse rate is equal to the lapse rate near the base of the inversion. The spectral data is then fit best by about a 10 degree drop in the temperature at 0.03 atm. A simple average of the brightening observed at each limb has been chosen to use with the spectral data. This average value should be closely related to the spectrum observed at disk center if the observed asymmetry of the planet represents a real variation of the thermal structure in time.

The CH_4 mixing ratio value of 2.0×10^{-3}, adopted in the final model (fig.4), is about three times the value most consistent with the abundance implied by theoretical models (Weidenschilling and Lewis, 1973) (about 6×10^{-4}) and the relative abundances of CH_4 and H_2 implied by spectroscopic data. For the latter abundance, the derived thermal structure is shown in fig. 7 and its spectrum in fig. 8 . The drop in CH_4 abundance lowers the opacity of the atmosphere in the 7.4-8.1 micron region. In order to match the spectrum, the thermal inversion for the low CH_4 mixing ratio model is required to be deeper in the atmosphere than in the model with the high CH_4 mixing ratio (fig. 7). The spectra of both models appear to provide a reasonably consistent fit to the data.

On the other hand, the model with the lower CH_4 mixing ratio does produce inconsistencies with two types of data. First, the effect of the deeper thermal inversion is to create far more limb-brightening than observed in the 20 micron channel of the Pioneer 10 infrared radiometer, as seen in fig. 9. The model is inconsistent with the Pioneer data for $\mu = 0.3$. The limb-brightening in the 20 micron channel may be avoided by decreasing the fractional amount of H_2 in the atmosphere. However, to fit the data, the He/H_2 ratio must be at least 33%. This is close to the upper limit suggested by the models fitting the Pioneer 10 infrared data, as it leads to some inconsistencies in the model results for the 20 and 40 micron channels. The high CH_4 mixing ratio model does not encounter such a degree of difficulty.

The other difficulty with the lower value of the CH_4 mixing ratio is the simulation of the center-to-limb scan at 8.15 microns, shown in fig. 10. The model with the low value of the CH_4 mixing ratio (6.2×10^{-4}) shows no limb-brightening, contrary to the observations. The high CH_4 mixing ratio model (2.0×10^{-3}) is consistent with the amount of limb-brightening observed. Limb-brightening at 8.15 microns may also be produced by increasing the amount of haze in the model with the low CH_4 mixing ratio. However, the amount of the haze necessary to increase the brightening of the model with the low CH_4 mixing ratio to the observed brightening is inconsistent with the spectrum at 8.5-

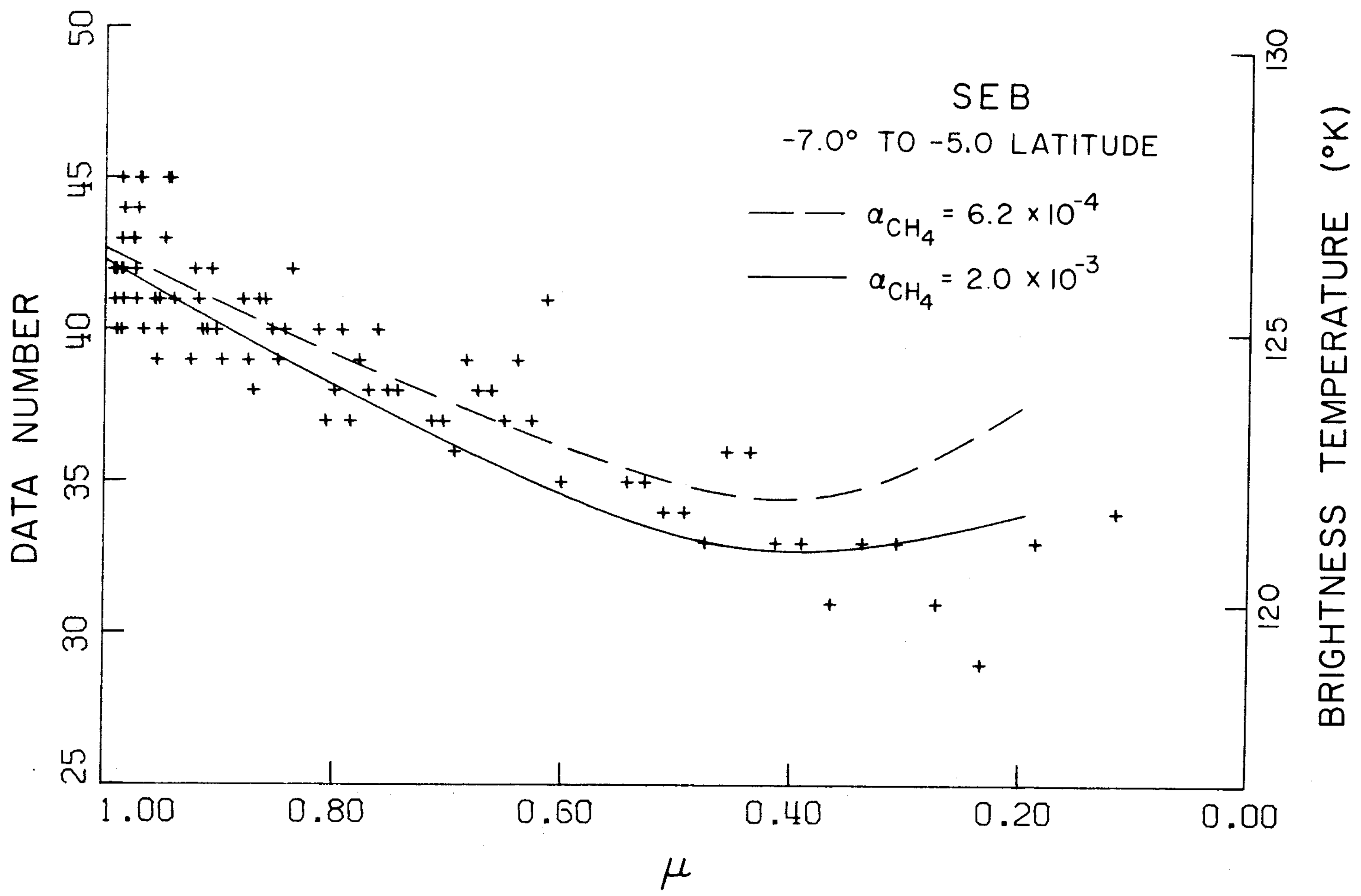

Fig. 9. -Limb structure of models for 20 micron channel of Pioneer 10 infrared radiometer 20 micron channel. Data for South Equatorial Belt (east limb) also shown. Models correspond to best fit spectral and limb structure data for different mixing ratios of methane (fig. 7).

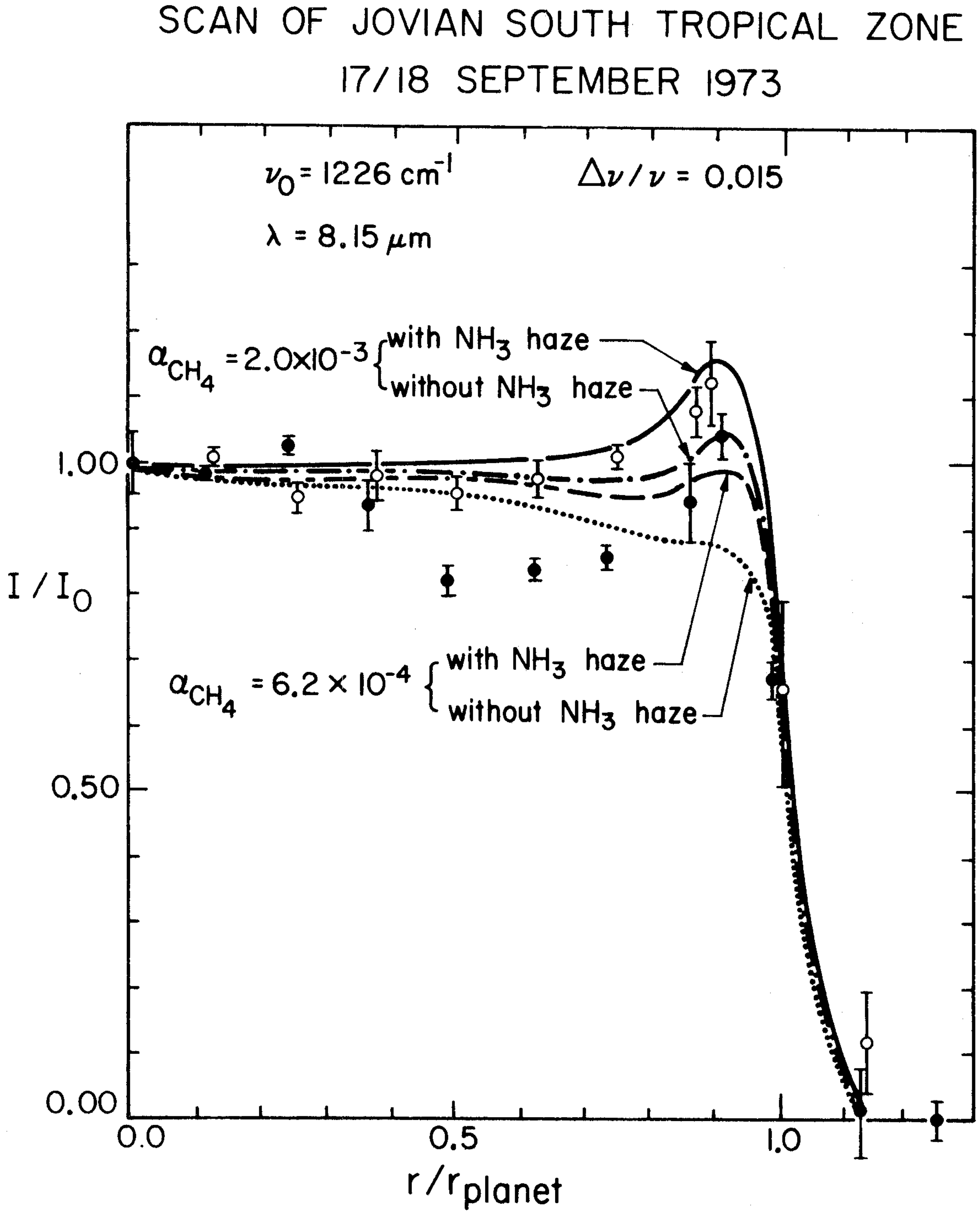

Fig. 10. -Comparison of models with limb structure data at 8.15 microns. Data is also shown in fig. 2 .

9.5 microns. It is readily observed (fig. 10) that the additional haze opacity, consistent with the spectrum, does not worsen the fit of the model with a higher abundance of CH_4.

The increase in the CH_4 abundance from the "nominal" value is therefore determined by a best fit to the Pioneer 10 20 micron channel data and the 8.15 micron observed limit structure. The final value for the mixing ratio should be good to within a factor of 1.5. Accordingly, the correlation of the structure of the thermal inversion generates an uncertainity in the thermal structure on the order of a 50% change in pressure.

The lack of the moderate central brightening in the best fit model may indicate the need for an even lower temperature minimum or that the level of the thermal inversion should be even higher. A further increase in the CH_4 mixing ratio would allow for the latter, and it might facilitate a less ambiguous fit to the 20 micron limb structure. However, it would also cause the 8.1 micron intensity to drop below observed values.

E. The NH_3 Clouds and Haze: the 8.2-9.5 Micron Spectrum

The spectrum resulting from removal of the NH_3 haze from the model, with the thick cloud still in the zones is shown in fig. 11. It is apparent that the opacity provided by the gases is not sufficient in this region. While no single simple gaseous species can be found which would provide strong enough opacities for this entire region, more complex molecules cannot by any means be positively ruled out. However, the haze of solid NH_3 particles first suggested by Taylor and Hunt (1972) appears to be a reasonable model on an *a priori* basis with respect to

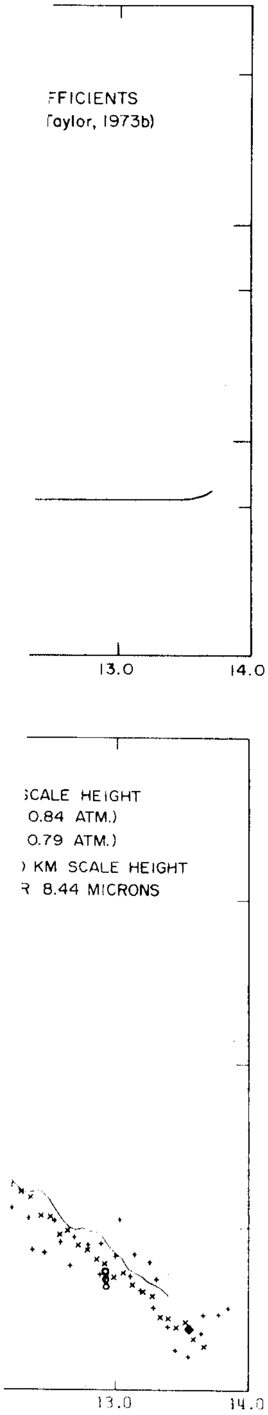

Fig. 11. Spectra of models with varying types and amounts of haze. Data as in fig. 3B. Solid NH_3 absorption coefficient displayed for comparison. Model thermal structure is that shown in fig. 5.

the presence of the thick cloud, presumed to be freezing NH_3.

The haze with the absorption characteristics of solid NH_3, as compiled by Taylor (1973b) and shown at the top of fig. 11 , is distributed exponentially in height. The assumption of an exponential distribution is quite arbitrary, but it does allow for a rather sensible change in the ratio of the density of the haze particles with the density of the gas. For example, a scale height of some 20 km produces an approximately constant ratio of the particle density of the haze to the total density of the surrounding gas. A scale height of 3.2 km produces an approximately constant ratio of the particle density to the density of NH_3 gas in the saturation region. No haze exists below the level where NH_3 saturation begins nor above the temperature minimum in the model, where it is assumed that the particles will sublimate to the gaseous state.

For the best fitting model, the scale height of this exponential distribution is 1.0 km and the location of unit optical depth at 8.44 micron (where the intensity in this spectral region is greatest) is near 0.83 atm, about 1.8 km above the thick cloud top for the haze in the belts and near 0.76 atm, about 3.8 km above the thick cloud top for the haze in the zones. For a lower value of the scale height, the spectral response approaches that of a black body, i.e. too low at 8.5 microns and too high at 9.5 microns. For a scale height which is much larger, there is a much larger difference between the intensity at 8.4 microns and 9.0 microns than is shown in the data (fig. 13).

For comparison, a haze which has a constant absorption coefficient in wavelength has been substituted for the NH_3 haze. The response of two such grey hazes, characterized by different total optical depth, is also shown in fig. 11 . The spectrum in the 8.2-9.5 micron region is close to

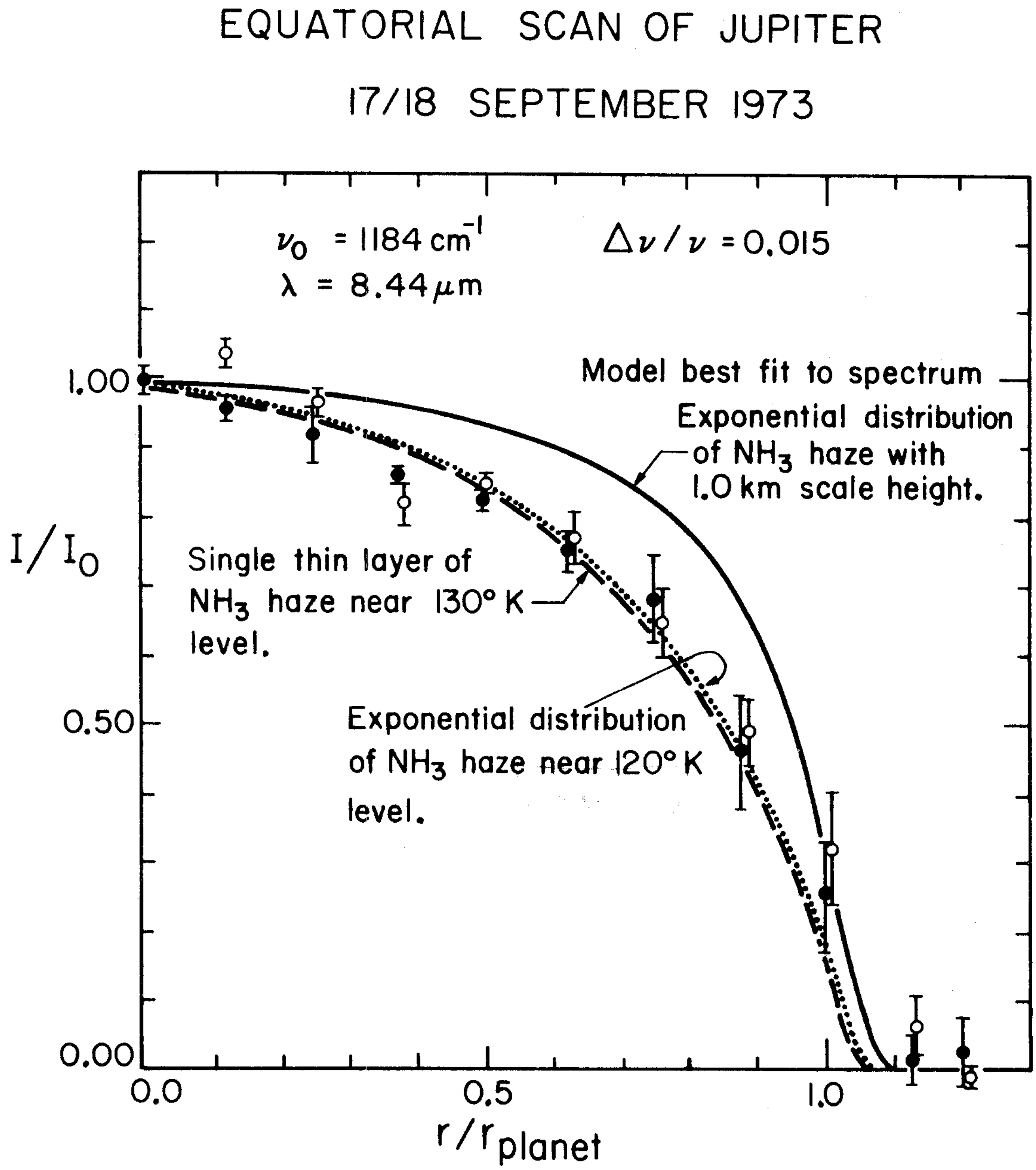

Fig. 12. -Comparison of models with limb structure data at 8.44 microns. Data is also shown in fig. 1.

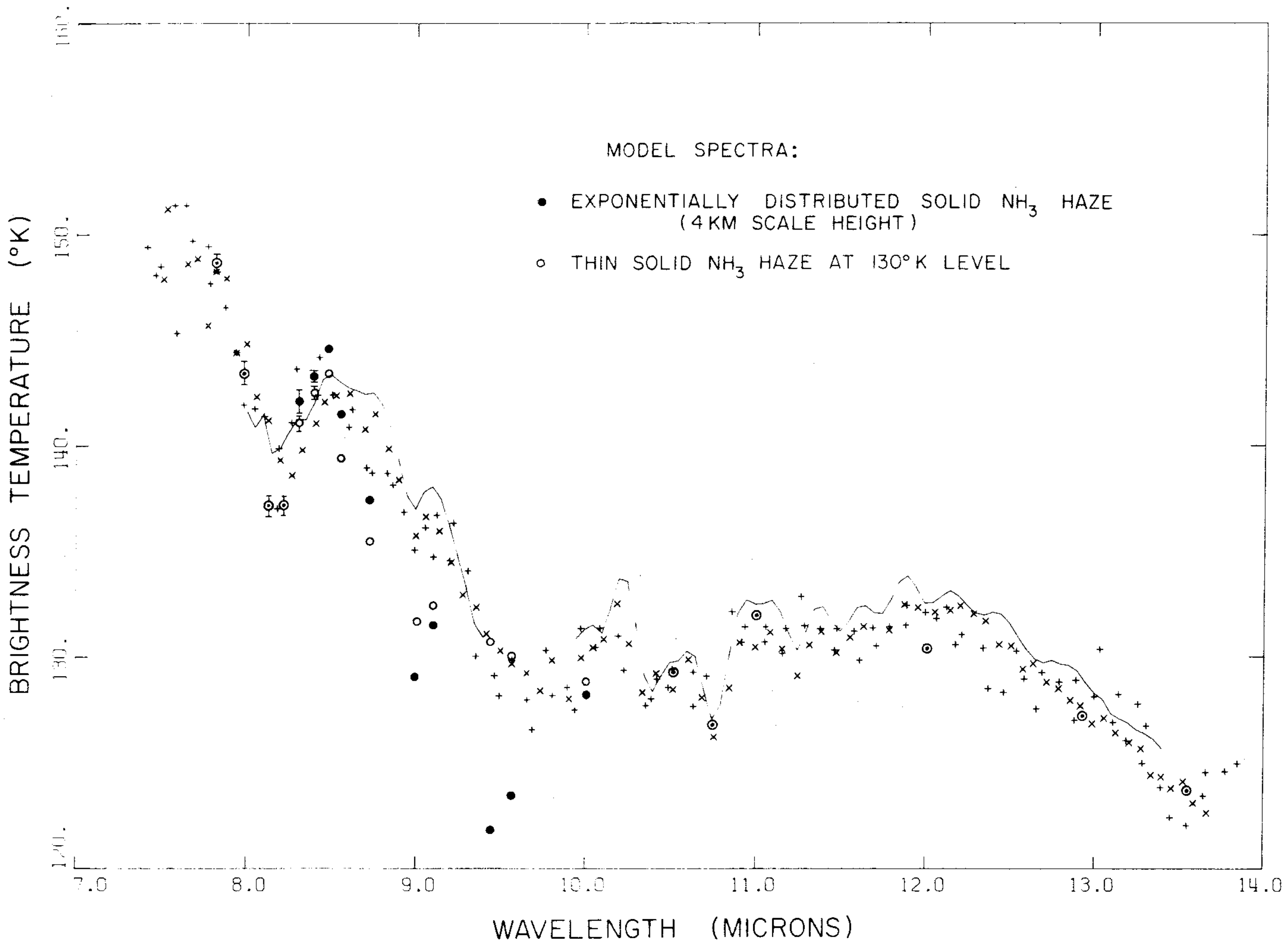

Fig. 13. -Spectra of models best fitting 8.44 micron limb structure data (fig. 12). Spectral data as in fig. 3B. Models have varying distributions of NH_3 haze.

that of black body emission for 143°K and 140°K, respectively. The effect of increasing the scale height of the haze or of raising the thick cloud in the zones to positions in the atmosphere near 140°K, or of placing a thick cloud in the belts, is the same. In comparison, the NH_3 haze reproduces the spectral characteristics quite well in this region, notably the absorption feature near 9.0 microns, which does not correlate with any feature in the gaseous absorption.

This crude haze model is considered to do little more than plausibly reproduce the observed shape of the spectrum in the 8.2-9.5 micron region. Two particular difficulties are encountered by this haze model if it is considered further. First, the path length of frozen NH_3 necessary to produce the requisite opacity in the 8.2-9.5 micron region is about equal to the full amount which could precipitate out of the atmosphere above the level where NH_3 begins to saturate out (for a partial pressure of 1.5×10^{-4} times the total pressure.) Second, the model simulation of the 8.44 micron center-to-limb scan (fig. 12) is visibly less limb darkened than the data.

The discrepancy with the physical chemistry of solid NH_3 might be explained by a systematic underestimate of the solid NH_3 absorption coefficients or the CH_4 gaseous opacity at 8.44 microns, by the assumption of an unrealistic distribution of the haze, or by the crude nature of the haze extinction which ignores the effect of particle size on scattering efficiency. There must in fact be a reduction of the opacity of the haze near 20 and 40 microns with respect to this model, in order for the intensity difference observed between both channels of the Pioneer 10 infrared radiometer to exist. At 8.44 microns, the relative limb brightening of the model with respect to the data indicates that either another opacity source besides the haze limits the observed brightness or that the haze is distributed somewhat higher in the atmosphere, if the thermal structure shown in fig. 5 is assumed to be correct. An additional opacity at 8.44 microns might be provided by a less approximate estimate of the CH_4 opacity at that wavelength. A larger value for the scale height of the haze or the presence of a single layer of haze above the thick cloud top both provide better fits to the scan, but are inconsistent with the spectral data (fig. 13).

It is apparent that the haze models used here are not consistent with all available data. For the purpose of this study, it is considered that a sufficiently plausible case has been made for the presence and activity of a haze layer of solid NH_3 particles somewhere near or above the 0.90 atm pressure level where these models have assumed an optically thick NH_3 cloud to exist in the zones. More realistic investigation of the haze with respect to composition, distribution and particle size must await a realistic treatment of multiple scattering and a somewhat larger base of 8.2-9.5 micron data for both belts and zones. Further considerations must be made of the effect of the haze extinction on radiation at wavelengths other than those in the 8-14 micron range. Such considerations are important, not only for radiation at wavelengths greater than 14 microns, where data has been obtained by Pioneer 10 and 11 and aircraft observations (Houck et al., 1974), but also with respect to 5 micron radiation (Westphal et al., 1974).

F. Lateral Variations

The ratio of the optical thickness of the haze in zones to that in belts is about 7.0 in the model. For the assumption of similar thermal profiles in both belts and zones, this successfully reproduces the belt to zone contrast observed by Westphal (1971) of about 25-30% for an 8.2-9.2 micron bandpass and 5-7% for a wide 8.2-13.5 micron bandpass. This would appear to imply that most of the contrast in the wide bandpass is coming from the 9.2-9.5 micron region. As noted earlier, a model with the same difference in haze distribution, but also with differences in thermal structure as implied by Pioneer 10 infrared data, results in 42% and 12% contrasts between belts and zones for the narrow and wide bandpasses, respectively (fig. 6). A model may be devised with an equal distribution of haze over both belts and zones which reproduces the spectrum quite well (fig. 11). However, this model results in nearly no contrast for either bandpass used by Westphal.

As stated previously, Westphal's (1971) observations are not consistent with the 20-30% contrast recently observed between belts and zones in the wide bandpass (Westphal and Terrile, 1974). Were this constrast due entirely to the 8.2-9.5 micron region, the intensity contrast would have to be much larger than the 25% previously observed. It is more plausible that the observed contrast is the result of differences in either the thermal structures or in the abundances of gaseous NH_3 in belts and zones. However the difficulties with these explanations have been noted earlier in this section: (1) the models inferred from the Pioneer 10 infrared data imply a contrast of only about 12% for the wide bandpass and (2) differences in the NH_3 gas abundance would imply undersaturated amounts of NH_3 gas in the belts, which is at odds with the spectral observations.

It is again emphasized that separate observations of belts and zones in this spectral region are necessary before spatial and temporal variation in thermal structure, NH_3 gas abundance and obscuring clouds and haze can be determined unambiguously.

V. DISCUSSION

In this section, the model derived is compared with others in the literature. Critical tests which might verify the model and also provide further useful information are summarized.

A. Comparison with Other Models

Figure 14 indicates the thermal structure of this model in comparison with other published models. These include: (a) the radio emission model of Gulkis, et al., (1973), (b) the spectral inversion of Ohring (1973), (c) the model thermal structure, based on Divine (1971), used in the 8-14 micron spectral analysis by Taylor and Hunt (1972), and (d) the radiative-convective equilibrium models by Wallace et al. (1974).

There are also large deficiencies between the model and the results of the Pioneer 10 neutral atmosphere inversion of the Pioneer 10 radio occultation data (Kliore et al., 1974). These are not shown in fig. 14 , but discussion of the differences with the model presented in this paper would be quite similar to that presented in Part 2 of this thesis with respect to models derived from Pioneer 10 infrared data. Therefore, such a discussion will not be repeated here.

As in the case with models derived from Pioneer 10 data, the model results derived in this study compare favorably with the model adiabat fit to microwave emission spectral data by Gulkis et al., (1973). In fact, all the models are consistent with this result to within the one standard deviation range, except for Ohring (1973).

Ohring's model for He/H_2 = 0.50 and α_{CH_4} (the CH_4 molar mixing ratio) = 1.8×10^{-3} has a thermal structure similar to the results of

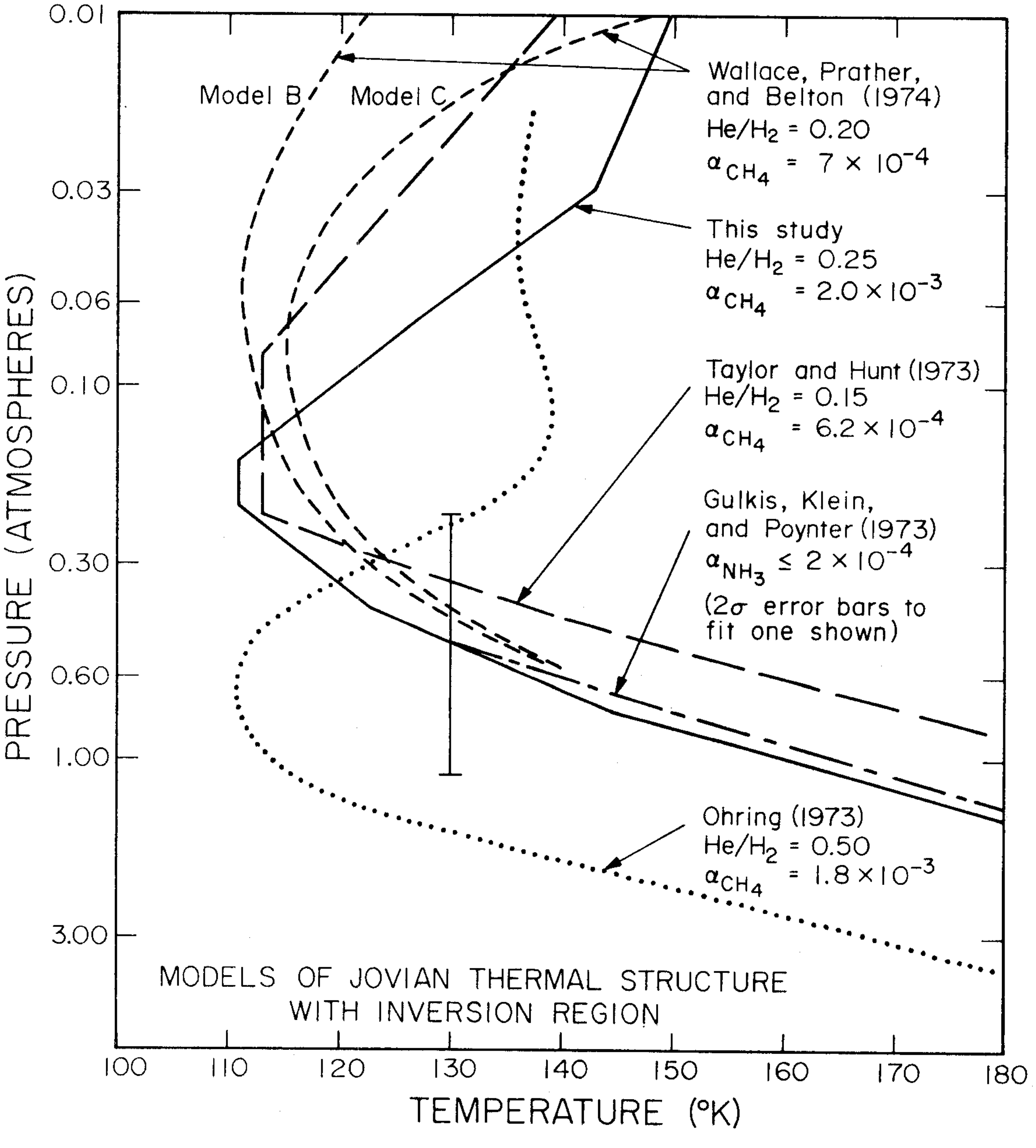

Fig. 14. -Comparison of thermal structure with other models. Derived thermal structure in solid line, representing results of this study, is that shown in fig. 5 .

this study, but there appear to be two major differences. First, the maximum temperature in the inversion region is below the results of this study. This could easily be attributed to the upward recalibration of intensities in the Gillett, Low, and Stein spectrum used here with respect to the data published originally. It will also depend upon the behavior of the thermal structure assumed above the levels which are displayed in his model. Second, the temperature minimum and the inversion structure appear to be displaced downward into the atmosphere by a factor of about 2.5 in pressure, relative to this study. The reason for this is difficult to assess. Ohring's inversion includes consideration of the brightness at 8.62 microns (1162 cm^{-1}) where he assumes that CH_4 is the only opacity source, but which has been found to be unreasonably bright under such an assumption (fig. 6). In the model presented here, the solid NH_3 haze is required to be the dominant opacity source at this wavelength. This study has also shown to a sufficient degree that the thermal structure must, indeed, change with a variation in the mixing ratio of CH_4 in order to maintain consistency with the spectral data. Ohring shows only minor changes in the thermal profile for a similar change in the assumed CH_4 abundance.

This study has attempted to be as rigorous as warranted by the data quality and resolution and by the available computational time. It may be best to consider Ohring's results as a reasonable first approximation to the inversion of the data, but subject to changes with somewhat more rigorous opacity models and the somewhat wider data base which is now available. It may be pointed out that Wallace et al., (1974) find inconsistencies with Ohring's results which are similar to the ones presented here, and that the spectrum of the Taylor and Hunt model uses a thermal profile similar to the one derived in this report, using techniques for estimating the opacity of CH_4 and NH_3 which are nearly identical to those used here.

The Taylor and Hunt (1972) thermal profile is identical to the model of Divine (1971) except that the inversion is allowed to continue upward to 155°K before an isotherm is assumed. While apparently providing a reasonable fit to the intensities of the original Gillett, Low and Stein spectrum, the model is not constrained by the more recent center-to-limb observations, in both 8 - 14 and 20 micron regions. A comparison of Taylor's (1972b) weighting functions in the CH_4 band near 8 microns compared extremely well with those calculated in this study for a similar CH_4 mixing ratio. Here, however, use of the random band approximation has been avoided close to the 7.7 micron center of the band because of its tendency to overestimate the opacity. This may also contribute to some of the model differences, as well. One of the major differences between the model presented in this paper and both the Taylor and Hunt (1972) and the Wallace et al., (1974) models (discussed below) is in the use of a higher mixing ratio for CH_4 ($\alpha_{CH_4} = 2.0 \times 10^{-3}$). This is about a factor of three higher than the value assumed by the other models.

The inversion region in the model presented here is located somewhat lower in the atmosphere than those derived in the Wallace et al., (1974) models, which assume radiative-convective equilibrium and are characterized by an effective temperature of 134°K. Model B assumes absorption of solar radiation by fundamental and overtone CH_4 bands; Model C additionally includes absorption of solar radiation by a hypothetical distribution of particulate materials. Model B results in spectral intensities in the CH_4 band which are cooler than the observations used as a data base in this study. Away from the band center, model C results in a more reasonable fit, but it assumes somewhat higher temperatures above the 0.01 atmosphere pressure level and would produce substantially more limb-brightening than indicated by observations at 7.94 microns.

Barring differences in the opacity estimates and the radiance calculations, the results described in fig. 8 would tend to indicate energy deposition somewhat deeper into the atmosphere than either models B or C of Wallace et al., (1974). If this energy is solar in origin, then it possibly indicates that the distribution of particulate materials which absorbs insolation is more heavily weighted toward the deeper part of the atmosphere than assumed in the hypothetical distribution of model C. Other more complex energy transport mechanisms cannot be completely ruled out, especially in view of the powerful Jovian magnetic field and the unusual activity associated with non-thermal radiation from the planet.

B. Recommendations for Further Work

Further observations, along with certain laboratory and theoretical studies, would be useful in clarifying the Jovian thermal structure and cloud properties. Among the most uncertain and inconsistent aspects of the model presented here are the following: (1) the uncertainties of the opacity estimates for gaseous constituents made in the model calculations, (2) the very crude estimate used for the opacity of the NH_3 haze, and (3) the lateral (belt to zone) variation of thermal structure, chemical composition, and cloud properties.

(1) The parameters of the opacity models are reasonably well understood at room temperature, with the exception of the CH_4 opacity at wavelengths equal to and greater than about 8.1 microns. Laboratory and theoretical work should be done to make reliable quantitative measurements of the distribution of line positions and their strengths and widths in this region of the P-branch of the ν_4 CH_4 fundamental band.

Of greater concern, however, is the lack of all but a few published measurements of absorption by the gaseous constituents at temperatures closer to those expected in the 1.0 - 0.01 atm pressure regime of the Jovian atmosphere. The lack of He-enchanced H_2 induced dipole absorption data is of particular concern. Corrections in the present H_2 opacity model may largely resolve the discrepancy between the thermal structures implied, respectively, by the 12 - 14 micron spectrum and the Pioneer 10 infrared data. Moreover, such corrections may place calculations of the atmospheric energy balance and the relative abundances of He and H_2 on a more reliable basis.

(2) The crude estimate of the solid NH_3 haze opacity must be improved. This may be done, first, by obtaining better measurements of the absorption coefficient than those used as the basis for this model (Taylor, 1973b). Self-consistency in such data can be determined by measurements of the wavelength-dependent real part of the index of refraction as well as the absorption coefficient (which determines the imaginary part of the index of refraction). Further studies of multiple scattering of radiation in a distribution of such particles may lead to models which are consistent with data at 5 microns and wavelengths greater than 14 microns, as well as in the 8 - 14 micron region.

(3) Separate spectral data in the 12 - 14 micron region for belts and zones may determine the lateral variation of the thermal structure near the level where pressure is about 0.5 atm. A greater correlation of earth-based measurements may then be made directly with spacecraft observations than possible at present. The ground work would then be established for the determination of the lateral variation of (a) NH_3 abundance via lateral variations in the 9.5 - 12.0 micron intensity and (b) haze and clouds via lateral variations in the 8.2 - 9.5 micron intensity. The distribution of particles in the haze may be further constrained by observations of center-to-limb structure in the 8.2 - 9.5 micron region.

In addition to resolution of the problems mentioned above, some means may be devised to determine more precisely the location and structure of the thermal inversion, and also the abundance of CH_4 which is highly correlated with it through the 7.4 - 8.2 micron spectrum. Narrow-band observations at the Jovian limb near 17 microns (somewhat more opaque than the broad 20 micron channel of Pioneers 10 and 11) may effectively "sound" the atmosphere near the base of the thermal inversion, although the required spatial resolution may only be attainable from nearby spacecraft. With a reliable estimate of the abundance of gaseous NH_3 from medium or high resolution spectrum, the region just below the temperature minimum may be effectively "sounded" by examining the intensity at the centers of individual strong lines of gaseous NH_3 near 10 microns in very high resolution spectra.

An interesting aspect of the thermal structure not addressed by present data is the possibility of lateral variations in the structure of the thermal inversion. Such variations may exist (a) between limbs,

(b) over different features on the planet, and (c) over regions with different amounts of available sunlight, e.g., observations near the planetary limb at equator and pole. Such variations might be detected by spatially resolved observations in the 8 micron region available from the ground. These might determine: (a) differences in the "morning" and "evening" inversion structure, (b) differences in the structure of the inversion over belts and over zones, and (c) dependence of temperatures in the thermal inversion on available solar radiation.

VI. SUMMARY AND CONCLUSIONS

This report has presented (1) observations of the limb structure near the equator of Jupiter at 8.15 and 8.44 microns, and (2) a model of the thermal structure and cloud properties of the atmosphere which is most consistent with spatially and spectrally resolved observations of the planet in the 8-14 micron region, including those in the first part of this report. The derived thermal structure is shown in fig. 5. A composition of $He/H_2 = 0.25$ is assumed on the basis of its consistency with most of the Pioneer 10 infrared data. Radiation emitted in the 12-14 micron region is not very sensitive to any atmospheric conditions other than the temperature near 0.4-0.6 atm.

Radiation in the 9.5-12.0 micron section of the spectrum is controlled by the thermal structure and the abundance of NH_3 gas, whose partial pressure can be no greater than the saturation vapor pressure at this level of the atmosphere. The spectrum in this wavelength region is matched well by the thermal structure fitting the 12.-14. micron data and by the assumption that NH_3 is fully saturated. However, this conclusion is probably inconsistent with recent 8-14 micron observations of Jupiter (Westphal and Terrile, 1974) showing some 20-30% contrast between belts and zones.

The structure of the thermal inversion is determined by data in the 7.4-8.2 micron region. The thermal inversion (fig. 5) is deeper than most other models in the literature. The molar mixing ratio of CH_4 is highly correlated with the thermal structure, as CH_4 is the major opacity source at these wavelengths. The mixing ratio of CH_4 most consistent with the spectrum and limb structure data is 2.0×10^{-3}, about a factor of 3 greater than assumed in most other models in the literature.

The 8.2-9.5 micron region of the spectrum is not easily matched by any gaseous opacity source. However, a haze of solid NH_3 particles above a thick cloud is quite consistent with the spectral intensities in this region and their variation with wavelength. The thick cloud, presumed to be composed of frozen NH_3, exists in zones and not in belts, corresponding to the models derived in Part 2 of this thesis.

The model used to calculate haze opacity consists of an exponential distribution of optical thickness in height (with a best fit scale height of about 1.0 km) with wavelength dependence directly proportional to the absorption coefficients of solid NH_3 compiled by Taylor (1973b). This is rather crude and it encounters difficulty with the expected amount of saturated NH_3 in the atmosphere and with limb structure data at 8.44 microns, where the haze is presumed to be the dominant opacity source. This model is probably also inconsistent with some observations outside the 8-14 micron range.

It is possible to match Westphal's (1971) observations of belt zone contrasts in the 8-14 micron spectral range with variations in the cloud and haze, or by including differences in the thermal structures of belts and zones, on the order of those implied by Pioneer 10 infrared data. However, the larger contrasts of more recent data cited above tend to indicate that differences may exist in gaseous NH_3 abundance also.

Some of the model inconsistencies are expected to be resolved with the help of low temperature laboratory measurements of the opacity of the relevant gaseous constituents. More accurate data for the solid NH_3 absorption coefficients is also needed, along with more realistic treatment of the scattering of radiation in the haze, before the size and distribution of particles in the haze can be understood and realistically modeled at a variety of wavelengths. Observations of the belt zone contrast at a variety of wavelengths in the 8-14 micron region will help to separate the effects of lateral variations in thermal structure, abundance of NH_3 gas, and cloud and haze properties.

Further observations may be devised which (1) provide independent verification of the derived thermal inversion structure and (2) explore the inversion structure dependence on time, on the corresponding visible appearance of the region, and on the amount of available sunlight.

APPENDIX A

Calculation of the Uncertainty in NH_3 and CH_4 Opacity

I. Assumptions regarding the probability distribution of line strengths:

For both CH_4 and NH_3, a random band model (Goody, 1963) has been used to estimate the opacity in a bandpass equal to the resolution of the 8-14 micron observations. All lines in the bandpass are assumed to be randomly distributed in frequency. The probability of finding a line with strength between s and s + ds in the bandpass may be given by:

$$d\pi = e^{-\sigma/s} ds \qquad \text{(exponential)} \tag{1a}$$

or

$$d\pi = (K/s) ds \qquad \text{(logarithmic)} \quad . \tag{1b}$$

The logarithmic assumption tends to include the presence of many more weak lines than the exponential assumption, and it leads to a greater opacity.

As a histogram of lines in either CH_4 or NH_3 bands do not clearly appear to be approximated better by one assumption than another, both are used to provide one measure of the uncertainty in the opacity of a given constituent.

II. Estimates of widths of individual lines:

For NH_3, the width of individual lines is given by:

$$\alpha(\mathrm{cm}^{-1}) = 0.075\left(\frac{p_{H_2}}{p_0}\right)\left(\frac{T_0}{T}\right)^{5/6} + \left(\frac{\alpha_i}{11.7}\right)\left(\frac{T_0}{T}\right)^{2/3}\left(\frac{p_{He}}{p_0}\right) \tag{2}$$

for $p_0 = 1.0$ atm, $T_0 = 300^\circ$K, and p_{H_2}, p_{He} the partial pressures of H_2 and He, respectively. α_i is the self-broadened width of each line given by Taylor (1973a). Varanasi (1971) has measured a nearly constant 0.074 cm^{-1}

for lines broadened by H_2. The broading coefficient of 11.7 is given by Gille and Lee (1969), as well as the temperature dependence of the widths, which originate from the theoretical work of Birnbaum (1967).

For CH_4, the width of individual lines is given by maximum and minimum estimates as follows:

$$\alpha_{MAX}(\mathrm{cm}^{-1}) = 0.080\left(\frac{p_{H_2}}{p_0}\right)\left(\frac{T_0}{T}\right)^{.55} + 0.048\left(\frac{p_{He}}{p_0}\right)\left(\frac{T_0}{T}\right)^{.50} \tag{3a}$$

$$\alpha_{MIN}(\mathrm{cm}^{-1}) = 0.068\left(\frac{p_{H_2}}{p_0}\right)\left(\frac{T_0}{T}\right)^{.45} + 0.042\left(\frac{p_{He}}{p_0}\right)\left(\frac{T_0}{T}\right)^{.20} \tag{3b}$$

for $T_0 = 273^\circ K$, and other parameters as in eq. (2). These estimates reflect the uncertainties in the measurements of Varanasi (1972), Varanasi and Tejwani (1972), Varanasi, et al. (1973), Rank, et al. (1966), and Darnton and Margolis (1973). These maximum and minimum estimates for line widths have been used in the determination of the minimum and maximum opacity estimates, respectively, resulting from assumptions (1a) and (1b) for the distribution of line strengths.

Note: A comparison of random band estimates of transmission with measurements of N_2-broadened CH_4 by Burch et al. (1962) and of H_2-broadened CH_4 at JPL (kindly supplied by Dr. F.W. Taylor) have shown consistent overestimates of the opacity of CH_4 close to the ν_4 band center at 7.66 microns (1306 cm^{-1}). Apparently, the dominance of the strong lines of the Q-branch of the band ($\Delta J = 0$ transitions) causes this systematic overestimate to be made. For this reason, no calculations have been made for $\lambda < 7.84$ micron (1276 cm^{-1}).

APPENDIX B

Non-plane Parallel Approximations Used in Model

For a ray emerging from one level of an atmosphere at radius R from the center of the planet at an angle from the normal given by $\cos^{-1}\mu$, the total path between levels R and R + ΔR may be computed simply by:

$$\Delta R' = R\left[\sqrt{\mu^2 + 2\beta + \beta^2} - \mu\right] \quad \text{for } \beta = \Delta R/R \quad . \tag{4}$$

For the model presented here, a planetary radius of 71,600 km from the Hubbard and Van Flandern (1972) observations of the Jovian occultation of β Scorpii is used for a reference radius near the 0.90 atm pressure level. R in eq. (4) is given by 71,600 km + z, for z equal to the distance above the reference level. At the planetary edge, then, μ is taken to be zero and $\Delta R' = R\sqrt{2\beta + \beta^2}$.

REFERENCES

Aitken, D.K. and Jones, B. 1972 " The 8 to 13 μm Spectrum of Jupiter." Nature, 240, 230-232.

Birnbaum, G. 1967, "Microwave Pressure-Broadening and Its Application to Intermolecular Forces." Adv. Chem. Phys., 12, 487-548.

Burch, D.E., Gryvnak, D., Singleton, E.B., France, W.L. and Williams D. "Infrared Absorption by Carbon Dioxide, Water Vapor and Minor Atmospheric Constituents." AFCRL-62-698, 316 pp.

Chase, S.C., Ruiz, R.D., Munch, G., Neugebauer, G., Schroeder, M., and Trafton, L.M. 1974, "Pioneer 10 Infrared Radiometer Experiment: Preliminary Results." Science, 183, 315-317.

Darnton, L. and Margolis, J.S. 1973, "The Temperature Dependence of the Half-Widths of Some Self- and Foreign-Gas-Broadened Lines of Methane." J.Q.S.R.T., 13, 969-976.

Divine, T.N. 1971, "The Planet Jupiter (1970)." NASA Space Vehicle Design Criteria (Environment) NASA SP-8069, Dec.

France, W.L. and Williams, D. 1966, "Total Absorption of Ammonia in the Infrared." J. Opt. Soc. Amer., 56, 70-74.

Gille, J.C. and Lee, T-H. 1969, "The Spectrum and Transmission of Ammonia Under Jovian Conditions." J. Atmos. Sci., 26, 932-940.

Gillett, F.C. 1973, Unpublished communication.

Gillett, F.C., Low, F.J., and Stein, W.A. 1969, "The 2.8-14 Micron Spectrum of Jupiter." Astrophys. J., 157, 925-934.

Gillett, F.C. and Orton, G.S. 1975, "Center-to-Limb Observations of Saturn in the Thermal Infrared." Astrophys J. (Lett.), in press.

Gillett, F.C. and Westphal, J.A. 1973, "Observations of 7.9 Micron Limb Brightening on Jupiter." Astrophys. J., 179, L153-L154.

Goody, R.M. 1952, "A Statistical Model for Water Vapor Absorption." Quant. J. R. Met. Soc., 78, 165-169.

Goody, R.M. 1963, Atmospheric Radiation, Part I; Theoretical Basis, (Oxford, Clavendon Press), 436 pp.

Gulkis, S., Klein, M.J., and Poynter, R.L. 1973, " Jupiter's Microwave Spectrum: Implications for the Upper Atmosphere." IAU Symposium on Exploration of the Planetary Systems, Torun, Poland.

Houck, J. Pollack, J.B., Schack, D. and Reed, R. 1974, "Aircraft Observations of Jupiter Between 16 and 40 Microns: A Determination of the Helium to Hydrogen Ratio and the Vertical Temperature Structure." 5th Annual Meeting, Div. of Planetary Sciences, Am. Astron. Soc., Palo Alto, Calif.

Hubbard, W.B., and Van Flandern, T.C. 1972, "The Occultation of Beta Scorpii by Jupiter and Io. III. Astrometry." Astron. J., 77, 65-74.

Kliore, A., Coin, D.L., Fjeldbo, G., Seidle, B.L., Rasool, S.I. 1974, "The Atmospheres of Io and Jupiter Measured by the Pioneer 10 Radio Occultation Experiment." 17th Plenary Meeting of COSPAR, Sao Paulo, Brazil.

Kyle, T.G. 1968, "Line Parameters of the Infrared Methane Bands." AFCRL-68-0521, 44 pp.

Newburn, R.L. and Gulkis, S. 1972, "A Survey of the Outer Planets Jupiter Saturn, Uranus, Neptune, Pluto, and Their Satellites." Space Sci. Rev., 14, 179-221.

Ohring, G. 1973, "The Temperature and Ammonia Profiles in the Jovian Atmosphere from Inversion of the Jovian Emission Spectrum." Astrophys. J., 184, 1027-1040.

Orton, G.S. and Gillett, F.C. 1974, "Thermal Structure of the Outer Atmosphere of Jupiter and Saturn from Center-to-Limb Observations in the Thermal Infrared." 5th Annual Meeting, Div. of Planetary Sciences, Palo Alto, Calif.

Rank, D.H., Fink, U., and Wiggins, T.A. 1966, "Measurements on Gases of Planetary Interest II. H_2, CO_2, NH_3 and CH_4." Astrophys. J., 143, 980-988.

Ridgway, S. 1974a, "Jupiter: Identification of Ethane and Acetylene." Astrophys. J., 187, L41-L43.

Ridgway, S. 1974b, "The Infrared Spectrum of Jupiter: 750-1700 cm." 5th Annual Meeting, A.A.S. Div. of Planetary Sciences, Palo Alto, Calif.

Taylor, F.W. 1972a, "Methods and Approximation for the Computation of Transmission Profiles in the ν_4 Band of Methane in the Atmosphere of Jupiter." J.Q.S.R.T., 12, 1151-1156.

Taylor, F.W. 1972b, "Temperature Sounding Experiments for the Jovian Planets." J. Atmos. Sci., 29, 950-958.

Taylor, F.W. 1973a, "Spectral Data for the ν_2 Bands of Ammonia with Applications for Radiative Transfer in the Atmosphere of Jupiter." J.Q.S.R.T., 13, 1181-1217.

Taylor, F.W. 1973b, "Preliminary Data on the Optical Properties of Solid Ammonia and Scattering Parameters for Ammonia Cloud Particles." J. Atmos. Sci., 30, 677-683.

Taylor, F.W. and Hunt, G.E. 1972, "The Infrared Spectrum of Jupiter and Radiative Properties of Clouds." 3rd Annual Meeting AAS Div. of Planetary Sciences, Kona, Hawaii.

Trafton, L.M. 1965, "A Study of the Energy Balance in the Atmospheres of the Major Planets." Ph.D. Thesis, Calif. Institute of Technology.

Trafton, L.M. 1967, "Model Atmospheres of the Major Planets." Astrophys. J., 147, 765-781.

Trafton, L.M. 1973, "A Comment on Jovian Greenhouse Models." Icarus, 19, 244-246.

Varanasi, P. 1971, "Collision-Broadened Half-Widths and Shapes of Methane Lines." J.Q.S.R.T., 11, 1711-1724.

Varanasi, P. 1972, "Shapes and Widths of Ammonia Lines Collision-Broadened by Hydrogen." J.Q.S.R.T., 12, 1283-1289.

Varanasi, P., Sarangi, S., and Pugh, L. 1973, "Measurements in the Infrared Lines of Planetary Gases at Low Temperatures. I. ν_3-Fundamental of Methane." Astrophys. J., 179, 977-982.

Varanasi, P. and Tejwani, G.D.T. 1972, "Experimental and Theoretical Studies on Collission-Broadened Lines in the ν_4 Fundamental of Methane." J.Q.S.R.T., 12, 489-493.

Wallace, L., Prather, M., and Belton, M.J.S. 1974, "The Temperature Structure of the Atmosphere of Jupiter." Astrophys. J., 193, 481-493

Weidenschilling, S.J. and Lewis, J.S. 1973, "Atmospheric and Cloud Structures of the Jovian Planets." Icarus, 20, 465-476.

Westphal, J.A. 1971, "Observations of Jupiter's Cloud Structure Near 8.5μ." in Planetary Atmospheres, ed. C. Sagan et al., Springer-Verlag, New York, Pp. 359-362.

Westphal, J.A., Matthews, K. and Terrile, R.J. 1974, "5-Micron Pictures of Jupiter." Astrophys. J., 188, L111-L112.

Westphal, J.A., and Terrile, R.J. 1974, unpublished communication.